




12-2020

## **Approaches to Studying Bacterial Biofilms in the Bioeconomy with Nanofabrication Techniques and Engineered Platforms.**

Michelle Caroline Halsted  
mhalsted@vols.utk.edu

Follow this and additional works at: [https://trace.tennessee.edu/utk\\_graddiss](https://trace.tennessee.edu/utk_graddiss)

 Part of the [Bacteriology Commons](#), [Biochemical and Biomolecular Engineering Commons](#), [Bioimaging and Biomedical Optics Commons](#), [Biological and Chemical Physics Commons](#), [Bioresource and Agricultural Engineering Commons](#), [Environmental Microbiology and Microbial Ecology Commons](#), [Nanoscience and Nanotechnology Commons](#), and the [Nanotechnology Fabrication Commons](#)

---

### **Recommended Citation**

Halsted, Michelle Caroline, "Approaches to Studying Bacterial Biofilms in the Bioeconomy with Nanofabrication Techniques and Engineered Platforms.." PhD diss., University of Tennessee, 2020.  
[https://trace.tennessee.edu/utk\\_graddiss/6075](https://trace.tennessee.edu/utk_graddiss/6075)

This Dissertation is brought to you for free and open access by the Graduate School at TRACE: Tennessee Research and Creative Exchange. It has been accepted for inclusion in Doctoral Dissertations by an authorized administrator of TRACE: Tennessee Research and Creative Exchange. For more information, please contact [trace@utk.edu](mailto:trace@utk.edu).

To the Graduate Council:

I am submitting herewith a dissertation written by Michelle Caroline Halsted entitled "Approaches to Studying Bacterial Biofilms in the Bioeconomy with Nanofabrication Techniques and Engineered Platforms.." I have examined the final electronic copy of this dissertation for form and content and recommend that it be accepted in partial fulfillment of the requirements for the degree of Doctor of Philosophy, with a major in Energy Science and Engineering.

Scott R. Retterer, Major Professor

We have read this dissertation and recommend its acceptance:

Jennifer L. Morrell-Flavey, Steven M. Abel, Jaan Mannik

Accepted for the Council:

Dixie L. Thompson

Vice Provost and Dean of the Graduate School

(Original signatures are on file with official student records.)

**Approaches to Studying Bacterial Biofilms in the  
Bioeconomy with Nanofabrication Techniques  
and Engineered Platforms.**

A Dissertation Presented for the  
Doctor of Philosophy  
Degree  
The University of Tennessee, Knoxville

Michelle Caroline Halsted  
December 2020

## DEDICATION

*In memory of Charles P. Halsted, ardent engineer and loving grandfather.*

## **ACKNOWLEDGEMENTS**

I am incredibly grateful of the support I have received throughout my graduate education with The Bredesen Center for Interdisciplinary Research and Graduate Education. I would like to thank my graduate adviser, Dr. Scott Retterer for his guidance, patience, and support. I'm incredibly grateful of the freedom and flexibility he provided, which allowed me to explore different fields and pursue educational opportunities outside my doctoral research. I would like to thank Dr. Jennifer Morrell-Falvey, Dr. Steven Abel, and Dr. Jaan Mannik for serving on my doctoral committee.

I would like to thank the members of Biological and Nanoscale Systems, Oak Ridge National Laboratory for their support, especially Dr. Amber Webb for sharing her enthusiastic love of microbiology. I would like to thank the staff at the Nanofabrication Research Laboratory, Center for Nanophase Materials Sciences for their assistance and patience. I'd also like to thank the members of Microbial Electrochemistry, Naval Research Laboratory for the internship opportunity and collaboration. I'm very appreciative of all my lab mates for sharing their expertise.

Lastly, I would like to thank my friends and family for their continued love and support, particularly Megan Lilly and OJ Caldwell who provided tremendous support as roommates with feedback on presentations and dissertation edits.

## ABSTRACT

Studies that estimate more than 90% of bacteria subsist in a biofilm state to survive environmental stressors. These biofilms persist on man-made and natural surfaces, and examples of the rich biofilm diversity extends from the roots of bioenergy crops to electroactive biofilms in bioelectrochemical reactors. Efforts to optimize microbial systems in the bioeconomy will benefit from an improved fundamental understanding of bacterial biofilms. An understanding of these microbial systems shows promise to increase crop yields with precision agriculture (e.g. biosynthetic fertilizer, microbial pesticides, and soil remediation) and increase commodity production yields in bioreactors.

Yet conventional laboratory methods investigate these micron-scale biofilms with macro-scale vessels and are limited in experimental throughput. This dissertation leverages nanofabrication techniques to engineer novel platforms for the study of bacterial biofilms from the bioeconomy. Nanofabrication can create micron-scale environments for bacterial biofilm studies and gain measurements inaccessible to conventional laboratory methods. Nanofabrication techniques can control physical and chemical influences (e.g. fluid flow, topography, confinement, surface roughness, chemistry, etc.) to mimic features of the natural environment. Platform design can also be aligned with microscopy and custom image processing algorithms to amass large datasets. Silane functionalization, together with image processing, investigated *Pantoea* YR343 biofilm propagation and enumerated the honeycomb biofilm morphology.

# TABLE OF CONTENTS

ABSTRACT.....	IV
CHAPTER ONE INTRODUCTION.....	1
1.1    Background .....	4
1.2    Research Aims .....	21
CHAPTER TWO FABRICATE NOVEL PLATFORMS TO FACILITATE STUDY OF MICROBIAL SYSTEMS .....	22
2.1    Silicon Microwell with Parylene Lift-off Layer.....	22
2.2    Transparent Microwell Platforms .....	25
2.3    Electrochemical Surface Plasmon Resonance Platform.....	36
2.4    Surface Functionalization and Patterning .....	46
CHAPTER THREE QUANTIFY CELL ATTACHMENT IN NOVEL PLATFORMS: IMAGE PROCESSING ALGORITHMS .....	54
3.1    Quantify Cell Attachment in a Transparent Microwell Platform.....	55
3.2    Quantify and Characterize Spatial Organization in Biofilms.....	58
CHAPTER FOUR ADAPTABILITY AND VERSATILITY OF MICROWELL PLATFORMS IN THE STUDY OF MICROBIAL SYSTEMS .....	62
4.1    High-Throughput Approach to Monitoring Cell Attachment .....	63
CHAPTER FIVE CELL ATTACHMENT STUDIES USING SUBSTRATE FUNCTIONALIZATION AND IMAGE PROCESSING .....	80
5.1    The Effect of Hydrophobicity on <i>Pantoea</i> sp. YR343 Cell Attachment and Biofilm Formation .....	81
5.2    Enumeration of <i>Pantoea</i> sp. YR343 Biofilm Propagation and Morphology .....	84
5.3    The Influence of FliR on <i>Pantoea</i> sp. YR343 Biofilm Propagation.....	93
5.4    Materials and Methods .....	99
CHAPTER SIX FUTURE DIRECTIONS .....	102
6.1    The Effect of Temperature on <i>Pantoea</i> sp. YR343 Biofilm Propagation	

6.2	The Influence of Cell Recruitment and Attachment on Honeycomb Biofilm Morphology .....	106
6.3	Next Steps: Investigate <i>Pantoea</i> sp. YR343 biofilm propagation with Confocal Laser Scanning Microscopy.....	112
6.4	Concluding Remarks .....	114
LIST OF REFERENCES.....		116
VITA.....		143



## LIST OF FIGURES

Figure 1.1.1: Stages of biofilm formation. Adapted from Beitelshées, et al., 2018.....	7
Figure 1.1.2: Surface Conditions Influence Cell Attachment and Biofilm Propagation. Source: Tuscon and Weibel, 2013.....	7
Figure 1.1.3: Flagellar proteins found in gram-negative bacteria. Core genes designated in bold. Genes colored in blue are widely present in different bacterial species. Genes in purple are sporadically distributed across bacterial species. Adapted from Liu and Ochman, 2007.....	10
Figure 1.1.4: Extracellular electron transfer in Bioelectrochemical Systems, example of an anodic processes. Adapted from Quejigo et al., 2019.....	12
Figure 2.1.1: Silicon microwell platform. (A) Fabrication of silicon microwell array begins with (i) Parylene deposition, (ii) photopatterning of a positive resist photomask, (iii) an oxygen plasma etches the exposed parylene, followed by a (iv) Bosch process to etch the microwell into silicon. Diagram is not drawn to scale. (B) Fluorescent imaging capability of silicon microwell array with bacteria confined to wells via Parylene lift- off.....	26
Figure 2.2.2: Transparent microwell. (A) fabrication, (B) assembly, and (C) imaging capability. (B) Schematic comparing imaging of silicon and transparent microwell platforms. On the left (B), the silicon microwell array is oriented with the well opening facing down on an inverted scope. On the right (B), the wells are imaged through a glass coverslip and a hydrated layer of agar, which allows for direct	

imaging through the coverslip-substrate using higher resolution, shorter working distance objectives. (C) Image of cells with high-resolution brightfield microscopy subset image emphasizes the advantage of the transparent microwell array's single-cell resolution (Olympus microscope, 40x). (D) Imaging capability with (i) fluorescence (Di), and (ii) phase contrast imaging.....28

Figure 2.2.3: Transparent microwell with parylene lift-off layer. (A) Fabrication is carried out with (i) dehydration bake on a coverslip substrate, (ii) SU-8 photolithography and deposition of a low-temperature ALD silicon dioxide film, (iii) parylene deposition, (iv) photopatterning of an aligned negative resist photomask, (v) an oxygen plasma etch to remove the exposed parylene. (B-E) Parylene lift-off layer: (B, D) scanning electron microscopy images of before lift-off and (C, E) after lift-off.....32

Figure 2.2.4: Tearing of parylene lift-off layer with SU-8 wells is promoted by poor alignment. (A, B) Remnants of parylene after lift-off and (C) tearing of large parylene section.....32

Figure 2.2.5: Thermanox™ microwell array fabrication (A) begins with a (i) low-temperature ALD silicon dioxide film, (ii) Parylene deposition, (iii) photopatterning of a negative resist photomask, (iv) an oxygen plasma removed the exposed parylene and etch the microwell into the Thermanox™. Diagram is not drawn to scale. (B) Image of Thermanox™ device. (C) Brightfield microscopy image of the Thermanox™ microwell, inset demonstrates the single-cell resolution at 20x. (D) Fluorescent image of Thermanox microwell; (E, F) scanning electron microscopy image of a Thermanox microwell and insert highlighting surface roughness.....35

Figure 2.3.1: Surface plasmon resonance imaging (SPRi) diagram, where the pink waves represent changes to the surface plasmons brought on by attachment of the sample. Source: Li and Zhong, 2012.....38

Figure 2.3.2: ESPR microwell platform. (A) Fabrication of microwell structure on gold SPR substrate with SU-8 Photolithography. (B) Example ESPR microwell configuration with 7 X 7 200  $\mu\text{m}^2$  square wells.....40

Figure 2.3.3: ESPR well platforms in the SPR chamber. (A) 400  $\mu\text{m}$  square, SU-8 2015 microwells, high quality fabrication; (B) 2 mm diameter, SU-8 2050 microwells, decent fabrication quality with small delamination edge effects on the first row; (C) 2 mm diameter, SU-8 2050 microwells on multielectrode device, poor fabrication quality and delamination; (D) 2 mm diameter, Poly-dimethylsiloxane (PDMS) wells; the white wells indicate presence of a biofilm.....42

Figure 2.3.4: ESPR PDMS well platform. (A) Fabrication: (i) 5 prepolymer: 1 cross-linker mixed and cured PDMS at 75°C; (ii) Biopsy punch generated 2 mm well; (iii) PDMS inking technique adhered PDMS wells to SPR slide. (B) Image of ESPR PDMS well platform (pre-wire attachment).....43

Figure 2.3.5: ESPR multielectrode well platform (A) Fabrication: (i) negative tone photoresist (NFR) photolithography; (ii) thin-film gold (37 nm) deposited on SPR glass slide; (iii) 5 prepolymer: 1 cross-linker mixed and cured PDMS at 75°C; (iv) Biopsy punch generated 2 mm well; (v) PDMS inking technique adhered PDMS wells to SPR slide. (B) Image of ESPR multielectrode well platform (pre-wire attachment).....45

Figure 2.3.6: Cyclic voltammetry feasibility experiment with ferrocene on ESPR multielectrode well platform. Cyclic voltammetry was performed on wells 3,5,8 at a scan rate of 1 mV/s.....47

Figure 2.4.1: Parylene stencil with SU-8 epoxy photoresist. (A) Fabrication: (i) Parylene deposition, (ii) photopatterning of SU-8 negative resist photomask, (iii)

an oxygen plasma to remove the exposed parylene. (B) Patterned collagen; (C) Pantoea YR343 attachment to patterned PFOTS on silicon substrate.....50

Figure 2.4.2: Formation of self-assembled monolayers on hydroxylated surfaces in the presence of an organosilane and trace amounts of water. The tail, represented by the “R”, functionalizes the surface while the opposing end bonds to the surface. Source: Glass et al., 2011 .....51

Figure 2.4.3: *G. sulfurreducens* attachment to CNS after six hours, brightfield microscopy, 40x objective. Cells were grown at grown at 30°C, vertical positioned substrate in a 30 mL volume, inoculated at 0.05 OD.....53

Figure 2.4.4: Patterned Carbon Nanospikes, imaged with Zeiss Scanning Electron Microscopy, coated with 5 nm chromium.....53

Figure 3.1.1: Outline of the ImageJ image processing algorithm labeled with built-in functions.....57

Figure 3.1.2: Percent area coverage standards and particle count masks. Left to right: particle count 10, and 1.1% area coverage; particle count 16, and 2.0% area coverage; particle count 34, 4.8 % area coverage; particle count 112, 10.9% area coverage.....59

Figure 3.2.1: Image processing and quantification of honeycomb biofilm pattern. Cells are grey in the original image and black after the threshold generates a binary image. The image is inverted, and the particle analysis function is applied to gaps in the image.....61

Figure 3.2.2: Propagation of *Pantoea* sp. YR343 honeycomb pattern with fluorescent images (left) and threshold images (right) at various stages in the

biofilm. Blue represents the cells (“branches”) and black represents the empty space (“gaps”).....61

Figure 4.1.1: Biofilm assay methods: substrate inoculated with 1 mL DCB-1 media, 0.05 OD *G. sulfurreducens* (A). Cells attached to substrate (B). Substrate removed at designated time point and rinsed with 10 mL DI water, 2 mL IPA, and dried with pressurized air (0.2 µm filter) (C). Imaged with brightfield microscope, 20x objective.....65

Figure 4.1.2: *G. sulfurreducens* seeding within SU-8 microwell platform with gold, glass, and quartz substrate materials. (A) Average cell area coverage ± standard deviation from each microwell (black line). The measurement of “Microwell Area Coverage” is the area of cells that have attached to the base of the microwell against the total microwell area. Representative images of *G. sulfurreducens* attachment at four hours for quartz (B) gold (C) and glass (D).....66

Figure 4.1.3: Percent area coverage standards and particle count masks. Left to right: Particle count 10, and 1.1% area coverage; Particle count 16, and 2.0% area coverage; Particle count 34, 4.8 % area coverage; Particle count 112, 10.9% area coverage.....67

Figure 4.1.4: Characterization of cell seeding within a microwell, gold substrate, 4 hours. (A) Diagram of annulus regions in microwell. (B) Spatial distribution of *G. sulfurreducens* area coverage in microwell. (C) Distribution of *G. sulfurreducens* seeding as a function of cell anchor size and location in the microwell.....69

Figure 4.2.1: Change in SPR pixel intensity of *G. sulfurreducens* cultures in PDMS wells 1, 7, 3, 9 (insert).....75

Figure 4.2.2: Cyclic voltammetry *G. sulfurreducens* activity at the surface of the SPR slide in turnover, stationary conditions: 2 scans with scan rate of 1 mV/s, applied potential of 0.20 V to -0.75 V vs. Ag/AgCl. (A) ESPR microwell platform, 49 simultaneous measurement; (B) ESPR PDMS well platform with deterministic seeding in 4 PDMS wells.....77

Figure 5.1.1: Biofilm assay methods for functionalized silane platform. (A) Substrates were submerged in 3 mL of R2A growth medium inoculated with *Pantoea* sp. YR343-GFP at an optical density (OD600) reading of 0.1. (B) Biofilm formation occurs for a set incubation period for each time point. (C) Substrates were removed at the designated time and rinsed with 10 mL of DI water, and dried with pressurized air (0.2 µm filter). (D) Imaging was carried out with a with 20x objective.....83

Figure 5.1.2: *Pantoea* sp. YR343 area coverage on hydrophobic and hydrophilic surfaces after 20 hours: Trichloro(1H,1H,2H,2H-perfluorooctyl) silane (PFOTS), n-octadecyl (trimethoxy) silane (OTS), 3-aminopropyl trimethoxy silane (APTMS), Methoxytriethylenoxypropyl- trimethoxy silane (MTMS); scale bar 50 µm.....85

Figure 5.2.1: Time course of *Pantoea* YR343 attachment to Trichloro(1H,1H,2H,2H-perfluorooctyl) silane (PFOTS). Error Bar: 1 Std Dev.....89

Figure 5.2.2: Characterization of *Pantoea* sp. YR343 morphology. (A) Relationship between Average gap size across dataset and time. (B) Relationship between average gap size and number per image, represented by a data point. Representative images from each time point correspond to the pink triangle data point on the plot, scale bar is 50µm.....88

Figure 5.2.3: Distribution of gap size across *Pantoea* sp. YR343 time points: (A) Distribution of gap size (percentage of gaps exceeding 1,000 pixels size is not

shown in plot); inset shows a comparative measure of gap size in pixels; (B) Distribution of gap size greater than 200 pixels; (C) Distribution of gap size less than 200 pixels.....89

Figure 5.2.4: An evaluation of *Pantoea* sp. YR343 biofilm propagation on PFOTS-silicon substrate using different microscopy methods. (A) Fluorescence microscopy after 10 hours attachment. Sample was rinsed with 10 mL DI water and dried with pressurized air. (B) Scanning Electron Microscopy after 10 hours of attachment. Sample was rinsed with 10 mL DI water, dried with pressurized air, and coated with 5 nm gold. (C) Wet biofilm at 13 hours, Confocal Laser Scanning Microscopy. (D) Vertical profile of *Pantoea* sp. YR343 biofilm at 2 hours (0-16  $\mu$ m). (E) Vertical profile of *Pantoea* sp. YR343 biofilm at 7 hours (0-12  $\mu$ m). (F) Vertical profile of *Pantoea* sp. YR343 biofilm at 24 hours (0-12  $\mu$ m). (G) *Pantoea* sp. YR343 biofilm propagation on PFOTS-Si substrate, 24 hours (Zeiss Scanning Electron Microscope, 5 nm gold coating).....91

Figure 5.3.1: Effect of *Pantoea* sp. YR343 FliR mutants on attachment to PFOTS, Area coverage after 24 hours. Scale bar 50  $\mu$ m.....95

Figure 5.3.2: Early attachment of *Pantoea* sp. YR343 WT and flagella mutants to PFOTS-Si substrate (Zeiss Scanning Electron Microscope, 5 nm gold coating). (A) *Pantoea* sp. YR343  $\Delta$ fliR, 3 hours. (B) *Pantoea* sp. YR343 *Tn5::fliR*, 3 hours. (C) *Pantoea* sp. YR343 WT 4 hours. (D, E) *Pantoea* sp. YR343  $\Delta$ fliR mutant on PFOTS-Si substrate, 24 hours (Zeiss Scanning Electron Microscope, 5 nm gold coating).....96

Figure 5.3.3: *Pantoea* YR343  $\Delta$ fliR mutant on PFOTS-Si substrate, 24 hours (Zeiss Scanning Electron Microscope, 5 nm gold coating).....97

Figure 5.3.4: Differences between *Pantoea* sp. YR343 WT and *Pantoea* sp. YR343  $\Delta fliR$  biofilm morphology. (A) Relationship between  $\Delta fliR$  average gap size and number per image, represented by each data point and overlaid on WT dataset. (B) Images of *Pantoea* sp. YR343 WT (53% area coverage) which corresponds to the blue dataset, and *Pantoea* sp. YR343  $\Delta fliR$  (52% area coverage) which corresponds to the orange dataset. These images illustrate the morphology differences in the two strains and the plot (right) demonstrates how image processing can enumerate morphology differences. Bubble size illustrates gap size standard deviation in each image, and the center point is the average gap size for each image, respectively.....98

Figure 6.1.1: *Pantoea* sp. YR343 biofilm propagation and morphology in normal room temperature conditions. (A) Time course of *Pantoea* sp. YR343 attachment to Trichloro(1H,1H,2H,2H-perfluorooctyl) silane (PFOTS) for 2018 and 2019 datasets; Error Bar: 1 Std Dev. (B) Relationship between gap size and number. Each data point corresponds to the average gap size in an image and the total number of gaps in the image.....103

Figure 6.1.2: The effect of temperature on *Pantoea* sp. YR343. (A) Comparing the effect of temperature on WT and  $\Delta fliR$  attachment to Trichloro(1H,1H,2H,2H-perfluorooctyl) silane (PFOTS); Error Bar: 1 Std Dev. (B) The effect of temperature on the cell number in the bulk solution.....105

Figure 6.2.1: Biofilm assay methods for functionalized silane platform. (A) Substrate were submerged in 3 mL of R2A growth medium inoculated with *Pantoea* sp. YR343-GFP at an optical density (OD600) reading of 0.1, and (B) nucleation sites form. (C) Substrate is removed after a seed period, rinsed with 10 mL of DI water. (D) Substrates are placed in new media and incubated. (E) Substrate is removed at designated time, rinsed with 10 mL of DI water, and dried



with pressurized air (0.2  $\mu\text{m}$  filter). (F) Imaging was carried out with a with 20x objective.....107

Figure 6.2.2: *Pantoea* sp. YR343 WT attachment to PFOTS-Silicon substrate. (A) The role of cell attachment on *Pantoea* sp. YR343 WT biofilm propagation where “seed” signifies the cell attachment period (B) Area coverage of a 3-hour seed culture compared to standard culture.....108

Figure 6.2.3: *Pantoea* sp. YR343 WT and  $\Delta\text{fliR}$  attachment to PFOTS-Silicon substrate. (A) The role of cell attachment on *Pantoea* sp. YR343  $\Delta\text{fliR}$  biofilm propagation where “seed” signifies the cell attachment period; two images represent the variation in the  $\Delta\text{fliR}$  biofilm for the time point. (B) Area coverage of a 3-hour seed *Pantoea* sp. YR343 WT and  $\Delta\text{fliR}$  cultures compared to the respective standard cultures.....110

Figure 6.2.4: *Pantoea* sp. YR343 WT and  $\Delta\text{fliR}$  attachment to PFOTS-Silicon substrate with 1-hour and 3-hour “seed” attachment. Cells attached during the seed period, then the substrate was removed from the culture, rinsed with DI water, and placed in new medium.....111

# **CHAPTER ONE**

## **INTRODUCTION**

Microbial communities are essential to both natural and engineered processes, an in-depth understanding is needed to fully optimize microbial systems for societal gain. Nanofabrication techniques can augment the study of microbial systems with high-throughput experimentation, control of microenvironments, and mimicry of natural features. Image processing algorithms can in turn extract numerical data from engineered platforms. This dissertation presents a multitude of tools to aid the study of microbial systems throughout the bioeconomy. Comprehension of these complex microbial systems will yield advances in soil health, precision agriculture, biochemical processing, and production of renewable energy & materials.

As we move to the future, society will be called to balance an increasing demand for energy and materials with environmental responsibility. There is an ongoing effort to leverage bio-based feedstocks (e.g. corn, switchgrass, crop residues, timber) as renewable alternatives to fossil fuel commodities (Rogers et al., 2016). The bioeconomy aims to transition from fossil fuels to bio-based feedstock commodities, and calls upon agriculture, forestry, waste management, and bioprocessing to generate renewable alternatives to energy, plastics, and specialty chemicals (Dietrich et al., 2016; De Besi and McCormick, 2015; Babu et al., 2013).

The first automotive engines were designed to run on plant oils, otherwise known as biodiesel (Ginley and Cahen, 2012). Similarly, bioplastics preceded petroleum-based plastic, but petroleum proved to be a cheaper feedstock material for both technologies (Raschka, Carus, and Piotrowski, 2013). Production of these bio-based commodity chemicals can be executed by microbial organisms in bioreactors, exploiting these “cellular factories” (Ginley and Cahen, 2012; Brown

and Brown, 2014). There is a growing trend to leverage mixed communities of microbial species to reduce the threat of contamination, optimize processing conditions, and commodity yield (Engel et al., 2019; Fradinho, Oehmen, and Reis, 2019). Transition to a bioeconomy calls upon the need to understand the complexities of microbial systems.

Bioelectrochemical systems (BES) are an extraordinary approach to microbe-commodity production (Borole, 2012). This field of study includes microbial fuel cells (MFC) and microbial electrolysis cells (MEC), which yield commodities from the exchange of electrons between electrodes and biofilms (Lovley and Nevin, 2013; Borole, 2012; Borole, 2015; Shi et al., 2016). These electroactive biofilms are formed by anaerobic, metal-reducing bacteria isolated from soils and marine sediment ecosystems (Lovley and Phillips, 1988; Logan and Regan, 2006; Lovley, 2012). These electroactive biofilms show great promise for carbon cycling, provided that economic and scaling limitations are addressed. For example, MECs can be incorporated into waste-water treatment facilities to simultaneously treat water and generate commodities (Logan, 2005; Rosenbaum et al., 2011; Logan and Rabaey, 2012). Fundamental research on extracellular electron transfer extends beyond bioenergy and includes efforts to understand soil health, such as biogeochemical cycling and bioremediation (Lovley, 2006; Lovley 2011; Lovley 2012; Cologgi et al., 2014; Shi et al., 2016; Steidl, Lampa-Pastirk, and Reguera, 2016). A collection of platforms were designed to aid the study of *Geobacter sulfurreducens*, a model organism of electroactive biofilms, and feasibility tests with these platforms are detailed in Chapter Four.

While there are many avenues to generate a biofuel or bioplastic, plant biomass is the primary feedstock for a vast number of biochemical processing systems and the root of the bioeconomy (Rogers et al., 2016; Aragon et al., 2017). There is a growing need to increase agricultural productivity to meet demand for food and renewables, emphasized by climate change and population growth (Quinn et al.,

2015; Aragon et al., 2017). Agricultural crops are cultivated in soils, which greatly influence plant growth and development in providing nutrients, water, and structural stability. As such, efforts to increase crop yields and cultivate stress-tolerant feedstocks will benefit from an increased understanding of soil systems, particularly in the rhizosphere, the soil region influenced by root activity (Raaijmakers et al., 2009; Quinn et al., 2015; Gouda et al., 2018; Ali et al., 2017). The rhizosphere is the most biological diverse ecosystem on earth, home to countless numbers of microbial communities (Raaijmakers et al., 2009; Gottel et al., 2011; Shakya et al., 2013; Ali et al., 2017; Rabbi et al., 2018). These microbial systems profoundly affect the rhizosphere by directly interacting with the plant roots and indirectly with biogeochemical cycling (Lugtenberg and Kamilova, 2009; Pii et al., 2016; Ali et al., 2017). Yet due to the opaque nature of soils, it is difficult to study microbial systems in the rhizosphere directly. Chapter five presents silane functionalization as an alternative approach to study *Pantoea* sp. YR343, an isolate of the poplar rhizosphere. Chapter Five also characterizes *Pantoea* sp. YR343 honeycomb biofilm morphology and propagation, accomplished by use of custom image processing scripts.

From the plant roots of bioenergy crops, to production of bioreactor commodities, microbial communities influence every stage of the bioeconomy. Rather than exist in a planktonic state, many species of bacteria form biofilms to protect against environmental stresses (e.g. antibiotics, toxins, flow, temperature, pressure, and pH) (Branda et al. 2005). Biofilms are not merely a film of cells, but a coordinated effort, and certain species of bacteria may form complex architectural structures, like a mushroom (Donlan, 2002; Ben-Jacob, 2008; Flemming and Wingender, 2010; Brider et al., 2010; Schultz, Onuchic, and Ben-Jacob, 2012). Biofilm formation is heavily influenced by a vast parameter space (e.g. spatial confinement, fluid flow, physiochemical influences, community members & abundance, etc.) and disentangling these variable influences requires novel experimental approaches (Little et al., 2008; Wang et al., 2011; Zhou et al., 2014;

Song and Ren, 2015; Cheng, Feng, and Moraru et al., 2019). This dissertation leverages nanofabrication techniques to engineer novel platforms for the study of bacterial biofilms. Fabrication of these platforms are detailed in Chapter Two. Data from the platforms are quantified with image processing algorithms, and these algorithms are described in Chapter Three. Platforms and image processing scripts from Chapters Two and Three are used to study *Geobacter sulfurreducens* and *Pantoea* sp. YR343, described in Chapters Four and Five, respectively. Lastly, Chapter Six describes recommended experiments, preliminary results, and concluding remarks.

## **1.1 Background**

This section of the dissertation describes relevant background information on biofilms. This includes general information on biofilm formation and cell-surface interactions. Background information on biofilms in bioelectrochemical systems and the rhizosphere are further described in this section, along with descriptions of *Geobacter sulfurreducens* and *Pantoea* sp. YR343. The background then shifts with how biofilms are studied with a summary of conventional methods, microscopy & image processing, and how other researches have used nanofabrication to aid microbial studies.

### **Biofilm Formation**

Biofilm formation begins with planktonic cells which migrate to the surface through swimming motility (flagella), Brownian motion (i.e. random collision of particles suspended in fluid), sedimentation (gravity), and convection (i.e. particles are pushed to a surface by fluid flow) (Palmer, Flint, and Brooks, 2007). As cells draw closer to the surface, Brownian motion increases, as does the drag in flow systems (Palmer, Flint, and Brooks, 2007). The initial cell-surface contact is considered reversible, and cells may wander via surface motility, or they may be pulled by the

surface shear stresses (e.g. flow, rinsing) or Brownian motion (Palmer, Flint, and Brooks, 2007; Kearns, 2010). At the surface, bacteria experience physiochemical forces described by the extended-DVLO (Berne et al., 2015; Berne et al., 2018).

After an initial period of cell adsorption, the cells secure surface attachment with adhesions. Chief among these is extrapolymeric substance (EPS), material secreted by bacteria cells that includes carbohydrates, lipids, proteins, and even DNA (Palmer, Flint, and Brooks, 2007; Flemming, Neu, and Wozniak, 2007; Colvin et al., 2012; Okshevsky et al., 2013; Das et al., 2013; Sutherland, 2001; Jakubovics et al., 2013). EPS can be hydrophobic or hydrophilic, and certain biofilms even use EPS to increase water retention (Donlan, 2002; Flemming and Wingender, 2010; van Schie and Fletcher, 1999). Cell appendages, such as flagella and pili, also play a role in adhesion (Lemon, Higgins, and Kolter, 2007; Berne et al., 2015; Berne et al., 2018).

Cells attached to the surface begin to form nucleation sites, recruit other cells with release of chemical signals (e.g. quorum sensing), and expand to form the monolayer biofilm on the surface (Davies et al., 1998; Stoodley et al., 2002; Visick and Fuqua, 2005; O'Toole and Kolter, 1998). Mature biofilms are often porous and include channels to allow fluid flow and the exchange of nutrients, waste, oxygen, etc. (Donlan, 2002; Flemming, Neu, and Wozniak, 2007; Schaudinn et al., 2007; Stoodley et al., 2002; Flemming and Wingender, 2010). EPS play a vital role in this architecture, protecting cells from environmental stresses and comprise 50-90% of the biomass in a biofilm (Evans, 2000; Flemming, Neu, and Wozniak, 2007; Bendaoud, 2011).

Some bacteria species use flagella to stabilize the multi-dimensional structure of mature biofilms (Flemming and Wingender, 2010; Wood, 2013). Serra et al. observed flagella on the substrate to be a dense mesh, analogous to ropes

tethering cells together (2013). The group speculated that flagella rotation entangled the “ropes”, securing the cells together (Serra et al., 2013).

While much is known about cell attachment and biofilm formation, there is much that remains unknown. This is especially true for biofilms in BES systems and the rhizosphere. The ability to understand, optimize, and direct the microbial systems holds significant potential for the bioeconomy, and a collection of complementary experimental methods, instruments, and analysis are needed for this effort.

### **Cell-Surface Interactions**

Biofilms begin with cell attachment to a surface (Figure 1.1.1). As such, the factors which govern bacteria attachment are of great interest to a multitude of fields. Surface topography, roughness, and other physiochemical forces influence bacteria attachment to surfaces (An and Friedman, 1998; Palmer and Brooks, 2007; Harimawan et al., 2011; Bendaoud et al., 2011; Crawford et al., 2012; Song and Ren, 2015). These surface characteristics can have a profound effect on cell attachment and biofilm propagation, and naturally occurring biofilms are likely to be affected by numerous factors simultaneously (Cheng, Feng, and Morau, 2019). Figure 1.1.2 summarizes how these factors can influence cell attachment.

In the past, surface topography referred to features with sizes greater than that of a bacterium, while surface roughness referred to submicron or nano-scale features (Palmer and Brooks, 2007). However, recent work by Cheng, Feng, and Moraru provides a more precise definition of these parameters (2019). Surface roughness merely describes the variation in surface height, whereas topography describes the entire surface configuration with spatial arrangement and vertical features (Cheng, Feng, and Moraru et al., 2019). Lack of precision in past use of surface roughness and characterization parameters may explain why there are contradictory results in the literature (Cheng, Feng, and Moraru et al., 2019). It's also likely that surface height variation (roughness) simply affects different bacterial species differently, not to mention the combined effects of surface height

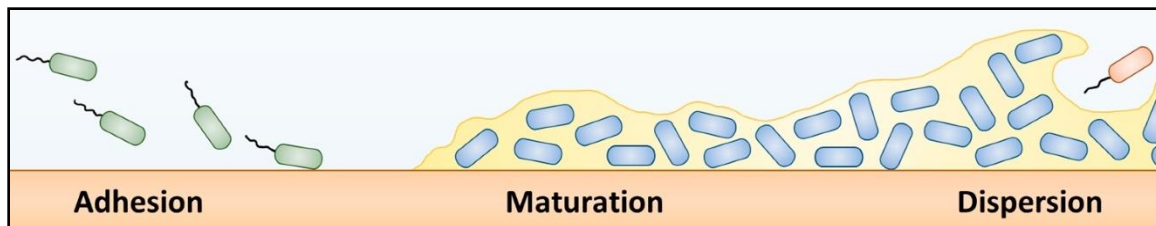


**Figure 1.1.1: Stages of biofilm formation. Adapted from Beitelshes, et al., 2018.**

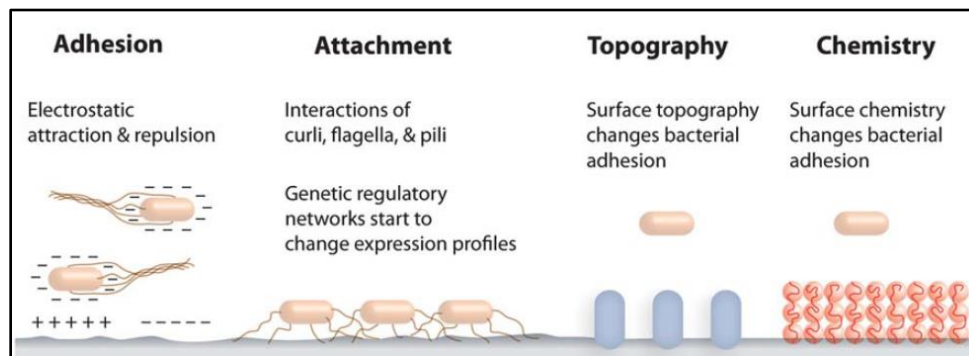


**Figure 1.1.2: Surface Conditions Influence Cell Attachment and Biofilm Propagation. Source: Tuscon and Weibel, 2013.**



variation with other physiochemical properties for a given experimental setup (Cheng, Feng, and Moraru et al., 2019). Topographic features can increase attachment by providing increased surface area and select sizes of topographic features can shelter cells from sheer stresses in environments with fluid flow (Hochbaum and Aizenberg, 2010; Epstein et al., 2011; Crawford et al., 2012; Berne et al., 2018).

Charge and hydrophobicity have immense influence on cell-surface interactions (Song and Ren, 2015; Berne et al., 2018). Bacteria have been shown to be negatively charged and attach more readily to neutral surfaces (Donlan, 2002; Berne et al., 2018). Specifically, many bacteria prefer attachment to hydrophobic, nonpolar surfaces (e.g. plastic) over hydrophilic, polar surfaces (e.g. glass), however bacteria are incredibly diverse and there are certainly exceptions (An and Friedman, 1998; Donlan, 2002; Palmer, Flint and Brooks, 2007; Song and Ren, 2015). Interestingly, hydrophobicity and charge of the cell envelope has been known to change under different growth conditions (Donlan, 2002). In certain cases, bacteria can even control for desirable surface conditions, and deposit various biomolecules before attachment, known as a conditioning layer (Palmer, Flint, and Brooks, 2007; Berne et al., 2015). Another example is the bacteria production of surfactants which decreases surface energy and supports swarming motility (Flemming and Wingender, 2010; Mukherjee and Das, 2010; Kearns, 2010; Wood, 2013).

These physiochemical forces interact with the bacterial cell envelope, which consists of the cell membrane, cell wall, and various polymer extensions (Malanovic and Lohner, 2016). Many bacteria have lipid-based functional groups on the outer exterior of the cell envelope with lipopolysaccharides (LPS) for gram-negative bacteria and lipoteichoic acid (LTA) for gram-positive bacteria (Li and Logan, 2004; Malanovic and Lohner, 2016; Silhavy, Kahne and Walker, 2010; Kurinčić et al., 2016). Bacteria also present proteins and polysaccharides on their

envelope, along with fimbrial structures (Silhavy, Kahne and Walker, 2010, Berne et al., 2015). Embedded further in the cell envelope is the peptidoglycan layer, comprising the cell wall in gram-positive bacteria and located in between the cell membrane layers in gram-negative bacteria (Silhavy, Kahne and Walker, 2010). While the LPS and LTA influence electrostatic interactions (both gram-negative and gram-positive bacteria), the peptidoglycan layer wields hydrophobic influence (Malanovi and Lohner, 2016).

The flagella play a key role in the cell-surface interactions, and not just by “getting there” via liquid and surface motility (Lemon, Higgins, and Kolter, 2007; Petrova and Sauer, 2012; Friedlander et al., 2013; Kearns, 2010; Guttenplan and Kearns, 2013; Berne et al., 2018). Swimming motility refers to single cell movement in fluids, and swarming motility refers to multicellular movement on a surface (Visick and Fuqua, 2005; Kearns, 2010; Herrera et al., 2008). The flagella is a complex biomolecular structure and of great interest to many researchers (Figure 1.1.3). The motor propels the cell forward by rotating the hook, and the filament follows (Nakamura and Minamino, 2019). In addition to motility, flagella can help bacteria overcome repulsive forces on the surface, anchor cells to niches in topographic features, and increase the surface area during initial cell attachment (Petrova and Sauer, 2012; Song et al., 2017; Berne et al., 2018). *Pantoea* sp. YR343 appear to use flagella as an adhesin and Chapter 5 investigates the effect of the flagella FliR protein on *Pantoea* sp. YR343 biofilms propagation.

### **Biofilms in Bioelectrochemical Systems**

Bioelectrochemical systems (BES) exploit electroactive biofilms on BES electrodes for production of electricity, fuels, and specialty chemicals. Microbial fuel cells (MFC) produce electricity and microbial electrolysis cells (MEC) use a power supply to drive production of hydrogen, hydrocarbons, and other commodity chemicals (Logan, 2005; Logan and Regan, 2006; Logan and Rabaey, 2012).

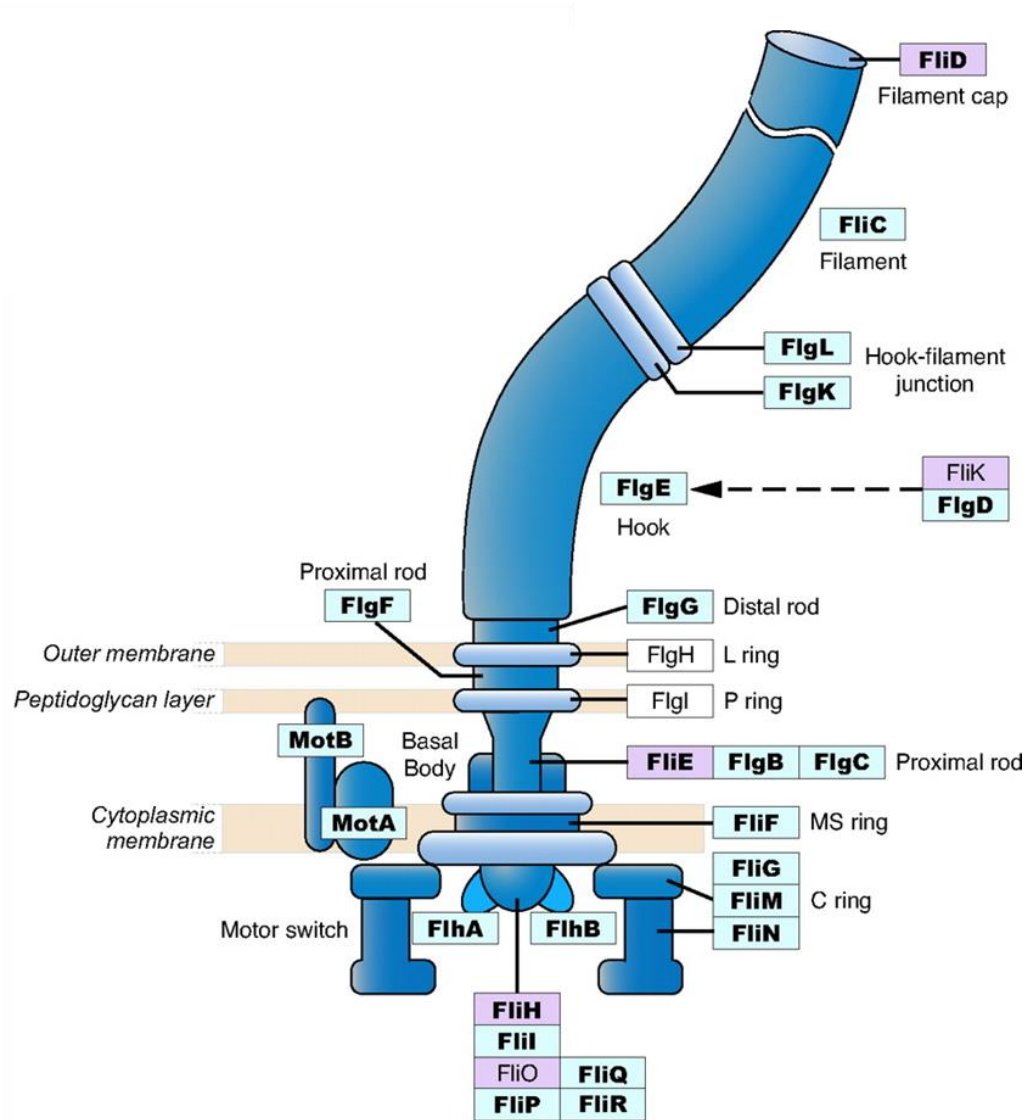
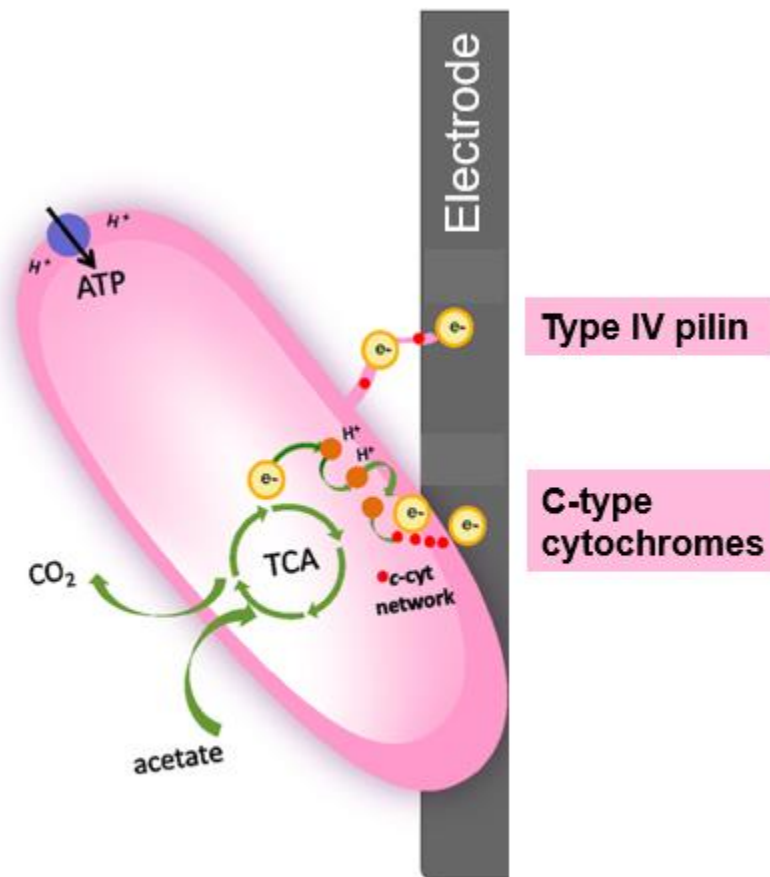


Figure 1.1.3: Flagellar proteins found in gram-negative bacteria. Core genes designated in bold. Genes colored in blue are widely present in different bacterial species. Genes in purple are sporadically distributed across bacterial species. Adapted from Liu and Ochman, 2007.

MFCs resemble classic galvanic fuel cells as electrons move from the bacteria-anode interface to recombine with protons in the cathode. The separation of the voltage potentials of the respective redox reactions drives electrons from the anode to the cathode, which generates current (Logan, 2005; Logan and Regan, 2006). Conversely, respiration occurs in the cathode of MECs and the voltage potential drives electroactive biofilms to catalyze commodity production or remediation of pollutants (Lovley, 2011; Lovley, 2012). BES technologies stand to gain from an increased understanding of electroactive biofilms.

*Geobacter* is a genus of gram-negative, bacteria isolated from soils and aquatic sediment, capable of “breathing” metals (Lovley and Phillips, 1988; Lovley, 2011). *Geobacter* are anaerobic bacteria which rely on metals and minerals, present in the soil, to accept electrons for completion of metabolic processes, just as animals rely on oxygen in the bloodstream. These electroactive bacteria transfer terminal electrons outside the cell envelope (extracellular electron transfer) to complete metabolic processes (Lovley, 2012). In BES systems, electroactive biofilms transfer electrons to inert electrodes when a voltage potential is applied; common electrode materials include platinum, gold, and various forms of carbon (Xie, Criddle, and Cui, 2015; Beyenal and Babauta, 2015).

*Geobacter sulfurreducens* is a model organism for electroactive biofilms, reported to transfer electrons distances upwards of 50 microns to an electrode (Rosenbaum et al., 2010; Lovley, 2011; Lovley, 2012). The underlying mechanism of this “long-range” extracellular electron transfer is at the heart of microbial electrochemical research. *G. sulfurreducens* use c-type cytochromes and pilin (type IV secretion system) to transfer electrons to biotic and abiotic surfaces (Lovley, 2006; Liu and Bond, 2012; Lovley and Nevin, 2013; Beyenal and Babauta, 2015; Xie, Criddle, and Cui, 2015; Lovley, 2012). Figure 1.1.4 illustrates extracellular electron transfer in a BES anode. C-type cytochromes are proteins with a heme functional group which facilitates the passing of electrons through the cell membrane(s) (Li and



**Figure 1.1.4: Extracellular electron transfer in Bioelectrochemical Systems, example of an anodic processes. Adapted from Quejigo et al., 2019.**

Bond, 2012; Li et al., 2011; Strycharz et al., 2011; Bond et al., 2012; Strycharz-Galven et al., 2012). The *G. sulfurreducens* pilin have been nicknamed “nanowires”, as these appendages transfer electrons through the biofilm (Reguera et al., 2005; Malvankar et al., 2012; Malvankar et al., 2015).

The mechanism for long-range electron transfer is part of an ongoing debate in the literature, and theories being considered include metal-like (delocalized) electron transfer along nanowires, electron “hopping” along the aromatic amino acids in the pilin, and electrons “hopping” along the c-type cytochromes in the cell membrane (Strycharz et al., 2011; Strycharz-Galven et al., 2012; Snider et al., 2012; Malvankar et al., 2012; Malvankar et al., 2015). Understanding the fundamentals of extracellular electron transfer will augment design and efficacy of bioelectrochemical systems.

### **Microbial Systems in the Rhizosphere**

Reports have found the concentration of bacteria in the rhizosphere to be 10-1000 times greater than regular soils, with thousands of different bacterial and fungal species (Brown et al., 2012; Pandit, et al., 2019). These plant-microbe relationships can be pathogenic or beneficial (Lugtenberg and Kamilova, 2009; Raaijmakers et al., 2009). Plant-growth-promoting-rhizobacteria (PGPR) contribute to the cycling of critical plant nutrients like nitrogen, phosphorus, and potassium. Some PGPR even secrete phytohormones (e.g. indole-3 acetic acid) to promote plant growth (Ramey et al., 2004; Singh et al., 2004; Berg, 2009; Gouda et al., 2018; Estenson et al., 2018). These rhizobacteria act as bio-fertilizers and can also serve as bio-remediators by deactivating or decomposing pollutants (Prasad, Bhattacharyya, and Nguyen, 2017; Gouda et al., 2018). Plant root exudation releases minerals and other biochemicals into the soil, providing a potential food source for rhizobacteria (Berg, 2009; Pandit, et al., 2019). Rhizosphere biofilms may take on many forms, from small clusters to an extensive network, and this may be due to the large variety in chemical and physical influences (Ramey et al.,

2004). Chemical composition of root exudate has been shown to directly influence cell attachment and biofilm formation (Pii et al., 2016; Sánchez-Cañizares et al., 2017; Pandit et al., 2020).

Characteristics of the root surface vary from mature roots to root hairs, and biofilms have shown a preference for actively growing root sites (Pandit et al., 2020). These actively growing root sites secrete mucilage to assist in soil penetration (Carminati and Vetterlein, 2013; Zickenrott et al., 2016; Zeppenfeld et al., 2017). Mucilage is a gel-like material released from root tips and is predominantly comprised of polysaccharides, the exact chemical composition varies with plant species (Zickenrott et al., 2016; Zeppenfeld et al., 2017). Interestingly, mucilage can store water to maintain a hydraulically conductive environment, yet becomes hydrophobic when dried, and repels water from the roots (Zeppenfeld et al., 2017). All these features substantiate an extremely diverse rhizosphere environment.

*Populus deltoides*, better known as poplar, is a fast-growing, hardwood tree and a promising bioenergy crop (Sannigrahi, Ragauskas, and Tuskan, 2010). *Populus* trees have emerged as a model for studying plant-microbe interactions in the rhizosphere as the diverse rhizosphere microbiome has been shown to influence growth and productivity (Walterson and Stavrinos, 2015). The microbial community in the poplar rhizosphere is incredibly diverse with members from phyla of Proteobacteria, Acidobacteria, and Verrucomicrobia (Gottel et al., 2011; Shakyia et al., 2013). Of these microbes, one genus of interest in Proteobacteria phyla is *Pantoea*, which contains both beneficial and pathogenic species. *Pantoea* has the advantage of being genetically tractable and is being explored for its bioremediation potential, antimicrobial production, phytohormone production and overall role in plant growth and development (Hebushima et al., 2011; Nakata et al., 2011; Walterson and Stavrinos, 2015). Studies on the *Populus* microbiome will help to understand the complexities between the rhizosphere microbiome and roots of other plants.

*Pantoea* sp. YR343 is a robust colonizer of *Populus* and has emerged as a model-bacteria for the poplar rhizosphere and has been engineered to express green fluorescent protein (GFP), facilitating the use of fluorescence microscopy (Bible et al., 2016; Vijaya Kumar et al., 2019). *Pantoea* sp. YR343 is gram-negative, aerobic, flagellate, rod-shaped bacteria with cells 1- 2  $\mu\text{m}$  in length and approximately 0.5  $\mu\text{m}$  in width (Bible et al., 2016). *Pantoea* sp. YR343 has been shown to exhibit swimming motility, surface motility, and biofilm formation (Bible et al., 2016; Vijaya Kumar et al., 2019). Studies also found *Pantoea* sp. YR343 produced the plant-growth hormone, indole-3-acetic acid, and solubilized phosphate, an important nutrient (Bible et al., 2016; Estenson et al., 2018). These attributes have promising opportunities for precision agriculture, but research efforts are challenged by the inability to directly visualize the soil microbiome. Investigation of *Pantoea* sp. YR343 and the rhizosphere microbiome calls for novel platforms.

### **Biofilm Assays**

O'Toole and Kolter began biofilm assays with a plate reader back in 1998, and this technique has since become the most widely used approach to studying biofilms (O'Toole and Kolter, 1998; Azeredo et al., 2016). A plate reader is capable of simultaneously measuring a multitude of biological samples on a microtiter plate (e.g. 96-well plate), and can measure fluorescence, optical density, stain quantities, etc. The optical density (OD) of a culture is a correlation of light refraction to the number of cells present in the culture, measured by a spectrophotometer at 600 nm wavelength (Azeredo et al., 2016). Culture readings can range from 0.05 OD<sub>600</sub> (early exponential growth) to 5.0 OD<sub>600</sub> (stationary phase); 1.0 OD<sub>600</sub> corresponds to roughly  $10^8$ - $10^9$  cells/mL (variation by size/species) (Moran et al., 2010).

Crystal violet (CV) stain is often used in conjunction with plate reader to perform biofilm assays (Bendaoud et al., 2011; Rollefson et al., 2011; Cologgi et al., 2014;



Stedil et al., 2016; O'Toole and Kolter, 1998). The crystal violet stain binds to extra polymeric substance (EPS) secreted by the cells during biofilm formation, and an increase in CV signal corresponds to an increase in biofilm growth (Tomaras et al., 2003; O'Toole and Kolter, 1998; van Schie and Fletcher, 1999; Stoodley et al., 2002). Note that the measure of CV is an indirect measure of biomass (Zaeredo et al., 2016). In a typical protocol, cells are grown-up in the microtiter plate, and rinsed with DI water. Mere bacteria-surface contact does not constitute a biofilm and the rinse step serves to remove loosely attached cells, such as those which may have settled to the bottom of the well. After the rinse step, cells are stained with crystal violet, incubated, and rinsed again to remove excess crystal violet stain. The CV stain is measured in the plate reader at 580-620 nm wavelength (Steidl et al., 2016; Bendaoud et al., 2011; Rollefson et al., 2011; Cologgi et al., 2014; O'Toole and Kolter, 1998).

Automated cell imagers and elaborate plate readers provide a rapid approach to high-resolution imaging (60-100x maximum magnification) and can even be outfitted with built-in image processing features. These systems include Lionheart Automated Microscope, BioTek Instruments, Inc., BioSpa Live Cell Analysis System. These systems can facilitate visualization of biofilm features, such as porosity and channels. Built-in processing features include label-free cell counts and automated image analysis software, which reduce workflow and facilitates data analysis. One drawback is that user-friendly software will often exchange convenience for exacting control, thus custom image analysis scripts are still recommended for complex features. Although these systems can visualize biofilm features, three-dimensional features are best captured by confocal scanning microscopy.

Cell attachment, the first step in biofilm formation, calls for different experimental protocols (Azeredo et al., 2016). Many studies on bacteria adhesion focus on metal and plastic surfaces to understand biofilm formation on man-made devices, such

as biofouling of pipes & ship hulls, contamination of medical devices & food processing equipment (Puckett et al., 2009; Das et al., 2008; Schultza et al., 2012). For this reason, bacterial attachment studies often use material coupons, or glass coverslips with material alterations. These substrates are removed after a set period of time, rinsed, and then analyzed (e.g. quartz microbalance with dissipation, water contact angle, zeta potential, atomic force microscopy, x-ray diffraction), and/or imaged with microscopy (van Schie and Fletcher, 1999; Reguera et al., 2005; Reguera et al., 2007; Logan and Li, 2004; Friedlander et al., 2013; Donlan, 2002; Berne et al., 2018; Malvankar et al., 2011).

### **Microscopy & Image Processing**

Imaging has been a hallmark of biological studies for centuries, providing qualitative descriptions of physical changes in biological systems. Simple, optical microscopes now feature charge-couple device (CCD) cameras to capture digital images. Brightfield microscopy images can be paired with image processing to quantify biomass and perform cell counts via particle analysis functions, image processing software (Choudhry, 2016). There are numerous open source algorithms designed to count cells and colony forming units in brightfield images (e.g. cell-counter, OpenCFU, ColonyArea, NIST's Integrated Colony Enumerator (NICE), CellProfiler, and Biofilm Growth Intensity (BGI) algorithm), and experimenters can write their own scripts with programs like ImageJ, MATLAB, and Python (Heydorn et al., 2000; Sieuwerts et al., 2008; Carpenter et al., 2006; Clarke et al., 2010; Cai et al., 2011; Geissman, 2013; Guzmán et al., 2014; Larimer et al., 2016). A typical approach creates a binary mask of the image and then applies a particle analysis function to quantify the number of objects (e.g. cells, colonies, nucleation sites) in the region of interest (Choudhry, 2016). While no stains are needed to perform cell counts with brightfield microscopy, image quality and improper illumination can hinder image processing (Choudhry, 2016).

Microscope image quality can be enhanced with stains and fluorophore-labeled cells. Crystal Violet is a stain that bind to EPS and is commonly used to visualize biofilms with brightfield microscopy (Merritt, Kadouri, and O'Toole, 2005; Larimer et al., 2016). A less popular biofilm stain is congo red dye, which binds to polysaccharides (Rollefson et al., 2011). One avenue to real-time cell monitoring is genetically engineering bacteria to express fluorescent protein (Azeredo et al., 2016). Image processing can quantify biomass from the intensity of a fluorescence signal. This is a common approach and numerous algorithms are available for processing these images in ImageJ, MATLAB, and Python (Ljosa and Carpenter, 2009). This technique attributes an increase in the fluorescent signal to an increase in cell number and is typically reported as “Relative Fluorescence Units (RFU)” (Hecht et al., 2016). Synthetic fluorophores can also be applied at the end of an experiment, such as the Live/Dead viability stains which are very popular with confocal laser scanning microscopy (Bridier et al., 2010; Mosquera-Fernández et al., 2014; Mosquera-Fernández et al., 2016; Hu and Bohn, 2017).

Confocal laser scanning microscopy (CLSM) revolutionized biofilm studies when it was introduced in early 1990s, by providing real-time, three-dimensional imaging of hydrated biofilms (Donlan, 2005; Azeredo et al., 2016). CLSM constructs three-dimensional images from a series of images captured during a vertical scan Azeredo et al., 2016. This is a valuable approach to examining mature biofilms because it enables visualization of biofilm porosity and complex architecture (Bridier et al., 2010; Mosquera-Fernández et al., 2014; Mosquera-Fernández et al., 2016). CLSM is paired with image analysis tools, and the software BIOFILMDIVER can perform measurements on areal porosity and the biofilm void ratio (Mosquera-Fernández et al., 2016).

Scanning Electron Microscopy (SEM), and other electron microscopy methods, have long been used to visualize bacterial biofilms (Azeredo et al., 2016). Substituting photons for electrons yields submicron imaging resolution up to ~200

nm (Joens et al., 2013). This allows for visualization of cell appendages, such as flagella and pili. However, these methods call for conductive coatings to mitigate charge accumulation which could compromise visualization of material secreted by bacteria, such as EPS (Hlawacek et al., 2014; Azeredo et al., 2016). Helium ion microscopy has been used to visualize biological samples. The ion beam can image the smallest of biological features with 50 nm resolution limit, yet rigorous fixation methods are needed to ensure the ion beam does not damage the sample (Hlawacek et al. 2014).

These methods offer complementary information and insight into the study of bacterial biofilms. New approaches will offer yet another perspective to this effort, increasing the collective understanding of microbial systems. Nanofabrication techniques can be combined with microscopy to enhance the study of microbial systems, through the creation of novel platforms.

### **Nanofabrication in Microbial Studies**

Nanofabrication techniques can be incorporated into biofilm studies to bolster comprehension of these complex dynamics as part of a greater effort to understand and exploit microbial systems in the bioeconomy. Nanofabricated platforms can gain measurements that may be inaccessible to conventional methods and can be paired with various microscopic and spectroscopic techniques (Holman et al., 2009; Kim, Park, and Chung, 2012; Hol and Dekker, 2014; Golden et al., 2018; Retterer, Morrell-Falvey, and Doktycz, 2019). Nanofabricated (and microfluidic) platforms have unveiled unique insights to microbial systems, such as aging cells and death, antibiotic resistance, and single-cell dynamics (Zhang et al., 2011; Stewart et al., 2005; Lindner et al., 2008; Norman et al., 2013; Gefen et al., 2008; Long et al., 2013).

Nanofabrication encompasses lithography, thin films, and etching (Hasu, 2016). Collectively, these fabrication techniques have developed an assortment of

platforms to aid microbial studies (Hol and Dekker, 2014). Etching enables topographic control and can create microscopic features (e.g. microwells or pillars) when combined with lithography methods (Ingham et al., 2007; Epstein et al., 2011; Yang et al., 2015; Halsted et al., 2016; Hansen et al., 2016; Timm et al., 2017; Aufrecht et al., 2018). Thin-films enable surface control via deposition of metals, oxides, polymers, self-assembled monolayers, etc. (Glass et al., 2011; Karakoy et al., 2014; Sugimura et al., 2002). Thin-film metal deposition (and lithography) can fabricate microelectrodes, capable of performing electrochemical experiments in microenvironments (Jiang et al., 2010; Jiang et al., 2013).

Nanofabrication techniques can control the microenvironment of bacterial studies with modification of surface chemistry, stiffness, topography, roughness, and confinement (Li and Logan, 2004; Epstein et al., 2011; Kim, Park, and Chung, 2012; Song et al., 2012; Friedman et al., 2013). Friedlander et al. found that flagella “reach” and “grasp” into trenches of topographic features to improve adhesion (2013). Nanofabrication of microwell platforms offers an approach to spatial confinement and can be combined with other nanofabrication techniques (Ingham et al., 2007; Park et al., 2011; Hol and Dekker, 2014; Halsted et al., 2016; Timm et al., 2017). Microfluidics, via soft lithography methods, have been extensively used to control fluid flow (i.e. sheer stresses), and there has been a rise in mimicry platforms, such as recreation of soil particle topography with Poly-dimethylsiloxane (PDMS) (Aufrecht et al., 2017; Aufrecht et al., 2018; Uehling et al., 2019; Millet et al., 2019).

This dissertation employs nanofabrication techniques to construct innovative platforms for biofilm experimentation, compatible with imaging, from which custom image processing algorithms extract numerical data. These approaches were applied to the study of biofilms in bioelectrochemical systems and the rhizosphere, with *Geobacter sulfurreducens* and *Pantoea* sp. YR343, respectively serving as case study bacteria for this work.

## 1.2 Research Aims

This dissertation is part of a greater effort to comprehend the role of microbial systems in the bioeconomy. Nanofabrication techniques and image processing algorithms will complement existing experimental methods, and the work presented here illuminates the potential for these approaches in the study of 1) *G. sulfurreducens* biofilms and 2) *Pantoea* sp. YR343 biofilms. The first research objective is to fabricate novel platforms to facilitate study of bacterial biofilms. This is accomplished by use of nanofabrication techniques, designing platforms that are compatible with microscopy and spectroscopic methods. The second research objective is to quantify cell attachment and biofilm propagation in novel platforms. This called for development of image processing algorithms to enable data collection from microscopy images and quantify biomass in nanofabricated platforms. The final research objective of this dissertation is to demonstrate the utility of these platforms in the study of bacterial biofilms.

Each platform has its own capabilities, advantages and disadvantages. This dissertation presents the transparent microwell array platform as a high-throughput approach to cell attachment studies by seeding of *G. sulfurreducens* on various based substrates. A collection of electrochemical surface plasmon resonance imaging (ESPR) platforms offer parallel experimentation of *G. sulfurreducens* biofilms. Functionalize silanes are used to modify surface chemistry and elucidate the effect of hydrophobicity on *Pantoea* sp. YR343 biofilm formation. Custom image processing scripts enumerated *Pantoea* sp. YR343 biofilm propagation and honeycomb morphology observed on hydrophobic surfaces. The functionalized silanes, combined with custom image processing scripts, were used to investigate the influence of FliR on *Pantoea* sp. YR343 biofilm propagation.

## **CHAPTER TWO**

### **FABRICATE NOVEL PLATFORMS TO FACILITATE STUDY OF MICROBIAL SYSTEMS**

Microbial systems are heavily influenced by bacterial member abundance, spatial confinement, fluid flow, surface characteristics, etc., and the complexities of this vast parameter space call for high-throughput screening platforms (Little et al., 2008; Zhou et al., 2014; Song and Ren, 2015; Hansen et al., 2016; Halsted et al., 2016; Timm et al., 2017; Wilmoth et al., 2018; Cheng, Feng, and Moraru et al., 2019). Conventional, batch-model methods limit the ability to adequately assess the numerous variables influencing these systems; thus, there is a need to develop alternative approaches to bacterial studies. Just as computers enabled complex mathematical computations by use of parallel processing, high-throughput screening platforms can perform bacterial studies in parallel and elucidate complex relationships. This chapter details the design and fabrication of novel platforms for the study of bacterial biofilms.

#### **2.1 Silicon Microwell with Parylene Lift-off Layer**

*A version of this work was originally produced by A. C. Timm, M. C., Halsted, J. L. Wilmoth, and S. T. Retterer.*

Timm, A. C., Halsted, M. C., Wilmoth, J. L., Retterer, S. T. (2017). Assembly and Tracking of Microbial Community Development within a Microwell Array Platform. J. Vis. Exp. (124), e55701. Doi:10.3791/55701.

With countless variables influencing microbial systems, there is a need to develop novel tools to screen bacterial communities in an efficient manner. Microwell platforms enable the *en masse* study of microbial communities while offering spatial and environmental control (Hansen et al., 2016; Hol & Dekker, 2014;

Ingham et al., 2007; Van der Viles et al., 2019). These platforms can be used with conventional microscopes and do not require flow systems, as needed with microfluidics platforms. Stochastic seeding facilitates screening of microbial systems with rapid assemblages of bacterial communities.

Hansen et al. developed a silicon microwell array with a parylene lift-off layer to enable stochastic seeding of microbial communities. Specifically, this work used 2,2-paracyclophane (Sigma) as a parylene precursor to form p-xylylene in a parylene coater (SCS Labcoter 2, Speciality Coating Systems). Timm et al. modified the methods in Hansen et al. to yield a second-generation silicon microwell array platform. These modifications are described here.

Parylene C precursor (3.5 g load) was deposited with a Labcoter 2, Specialty Coating Systems on a silicon wafer (Silicon Quest), coated with 10 nm silicon dioxide (thermal oxide process: Temperature: 1000°C, O<sub>2</sub>: 3000sccm, H<sub>2</sub>O: 3ml/min, Pressure: 1atm, Time: 80 min) to yield a thin parylene layer ( $2 \pm 0.5 \mu\text{m}$  thickness). Shin-Etsu Microprime P20 adhesion promoter was spun-cast onto the substrate at 3000 rpm, 45 s, followed by S1818 photoresist (MicroChem Corp.), (3000 rpm, 45 s). The substrate was placed on a hot plate at 115°C for 90 s, exposed for 6s using the SUS + Micro Tec, MA6/BA6 contact mask aligner, developed in CD-26 developer (Microposit MF, Malborough, MA) for 1 min and 20 s, then rinsed with distilled water and dried with pressurized nitrogen.

An Oxford Plasmalab 100 reactive ion etching system removed the exposed parylene with an oxygen plasma. The estimated parylene etch rate is 0.5  $\mu\text{m}/\text{min}$ . Next, a five cycle Bosch process etched the silicon (1.1  $\mu\text{m}/\text{cycle}$ ) to achieve a well depth of 5  $\mu\text{m}$ . A summary of these fabrication methods can be found in Figure 2.1.1, A.



To form stochastic communities, a bacterial culture was applied to the platform. Time passed to allow cells to attach to the microwell, this period is referred to as seeding. After the seeding period, the liquid culture was pipetted up from the platform and the parylene layer was removed. The only cells that remained on the platform were the cells that attached within the microwell during the seeding period. This created independent cultures of bacteria within the wells as cells that attached between the wells were removed with the parylene.

The parylene removal process is as follows. Two opposing platform edges are taped to the counter (previously sterilized) and a third piece of tape removes the parylene with part of the tape pressed along the parylene and the other held by tweezers. The tweezers slowly pull the tape-parylene to the opposing edge and the parylene lifts off. The remaining tape is removed from the edges and the platform is ready for imaging or incubation.

Timm et al. modified the fabrication methods outlined in Hansen et al. to improve cell seeding (2016). The original device called for a 20  $\mu\text{m}$  microwell depth and this was changed to 5  $\mu\text{m}$  to increase cell-microwell seeding, accessibility of the food source (agar layer), and facilitate data collection with the automated z-scanning on the microscope camera.

Initially, the work described in Timm et al. experienced a high rate of failure with the parylene lift-off layer. This greatly hindered experimentation and a concerted effort to improve the parylene lift-off success rate was put forth. Parylene N was used in the original Timm et al. platform and an investigation into parylene mechanical properties revealed this to be the likely source of lift-off failure. Parylene N has a tensile ultimate strength of 45 MPa and an elongation of only 30% (Specialty Coating Systems, 2011). Tensile ultimate strength is the maximum stress the material can withstand, while the elongation measures how far the material can be stretched, as a percentage of its original length. Parylene C (70

MPa) has a tensile strength nearly 1.5X that of Parylene N and an elongation of 200% (Specialty Coating Systems, 2011). A switch was made to Parylene C and the lift-off failure rate decreased dramatically.

Wilmoth et al., leveraged data ascertained by this platform to build an agent-based model to examine the role of spatial confinement and organization on H1-Type VI secretion system (T6SS) in *Pseudomonas aeruginosa* mutants (2018). This work found spatial confinement of a microwell to effect T6SS cell contact & lysis, relative species abundance, cell density, metabolites and spatial organization, all of which were parameters in the model.

## **2.2 Transparent Microwell Platforms**

The motivation for this work is aligned with the silicon microwell platform described in Timm et al. (2017). Microwell platforms with a transparent base are compatible with both brightfield and fluorescence microscopy, eliminating the need for fluorescent cell labels. Transparent microwell platforms aid microbial community studies by offering an additional channel for data collection, as compared with the silicon microwell platform. This section describes the fabrication processes for several different transparent microwell platforms.

### **Transparent Microwell**

*A version of this work was originally published by M. Halsted, J. L. Wilmoth, P. A. Briggs, R. R. Hansen, D. P. Briggs, A. C. Timm, and S. T. Retterer:*

Halsted, M., Wilmoth, J. L., Briggs, P. A., Hansen, R. R., Briggs, D. P., Timm, A. C., and S. T. Retterer. (2016). Development of transparent microwell arrays for optical monitoring and dissection of microbial communities. *Journal of Vacuum Science & Technology B*. 34, 06K103. <https://doi.org/10.1116/1.4962739>

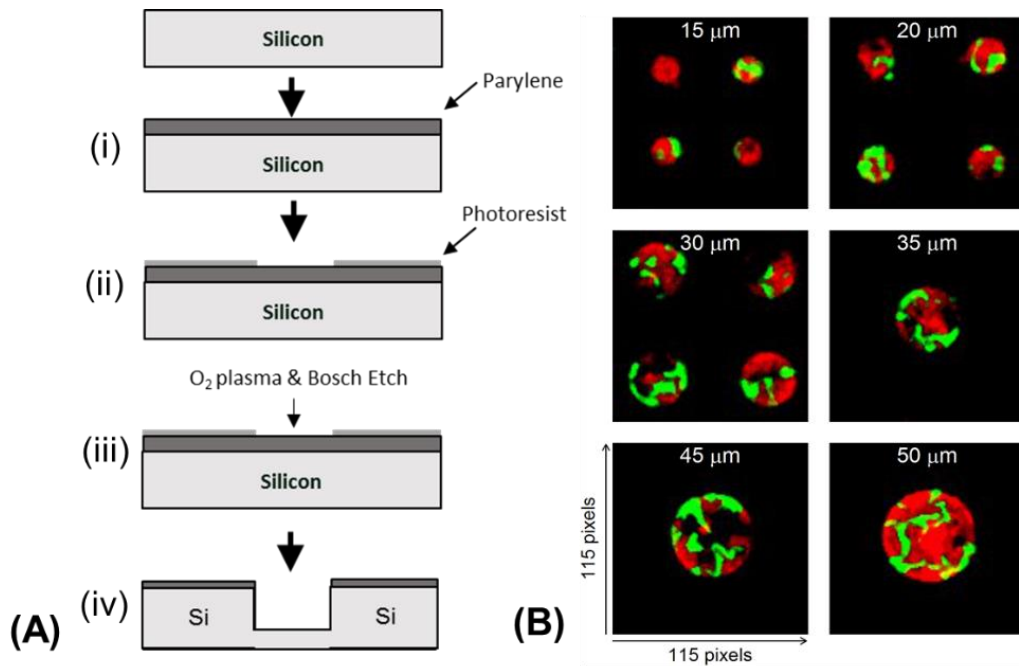


**Figure 2.1.1: Silicon microwell platform. (A) Fabrication of silicon microwell array begins with (i) Parylene deposition, (ii) photopatterning of a positive resist photomask, (iii) an oxygen plasma etches the exposed parylene, followed by a (iv) Bosch process to etch the microwell into silicon. Diagram is not drawn to scale. (B) Fluorescent imaging capability of silicon microwell array with bacteria confined to wells via Parylene lift-off.**

Fabrication of the transparent microwells was carried out using a combination of SU-8 lithography, atomic layer deposition, photolithography and reactive ion etching. Specifically, the microwells were created from (biocompatible) SU-8 photoresist-epoxy spun-cast on to a glass cover slip (120  $\mu\text{m}$  thickness). To improve adhesion of the SU-8 to the glass, the coverslips were heated for at least an hour at 180°C prior to photolithography. This dehydrates the glass and reduces moisture at the SU-8 and glass interface.

SU-8 2005 (MicroChem Corp., Westborough, MA) was spun-cast onto the coverslip; the spin-speed and duration were chosen in accordance with the manufacturer's recommendation for the desired thickness. To achieve a 5  $\mu\text{m}$  microwell depth, SU-8 2005 spun-cast at 2000 RPM, 45 s. A soft bake at 95°C was performed for 1.5 min prior to exposure. The substrate was exposed for 5.4 s in a Quintel UV Contact Aligner (Rochester, NY) at a power of  $\sim 10 \text{ mW/cm}^2$  (365 nm) and exposed at  $150 \text{ mW/cm}^2$  for SUSS + Micro Tec, MA6/BA6. After exposure, the sample was placed on a 65°C hot plate for one minute, and then a 95°C hot plate for 3 min. The spray-puddle technique was applied with SU-8 Developer (MicroChem, Westborough, MA) for 40 s, rinsed with SU-8 Developer and isopropyl alcohol (IPA), and then dried with pressurized nitrogen. Figure 2.2.2 highlights aspects of the transparent microwell platform.

Figure 2.2.2, B compares the transparent microwell platform to the silicon microwell platform for experiments with time-lapse imaging where agar caps the microwell. This contains the cells and provides a food source. Figure 2.2.2 B illustrates the decreased working distance for glass coverslip substrates (120-200  $\mu\text{m}$ ) compatible with high resolution objectives. Figure 2.2.2, C-D illustrates the high-resolution imaging capabilities of the transparent microwell platform.

Time-lapse imaging does not meet the needs of all experiments and is not amenable to anaerobic conditions. Time point experiments, with terminal

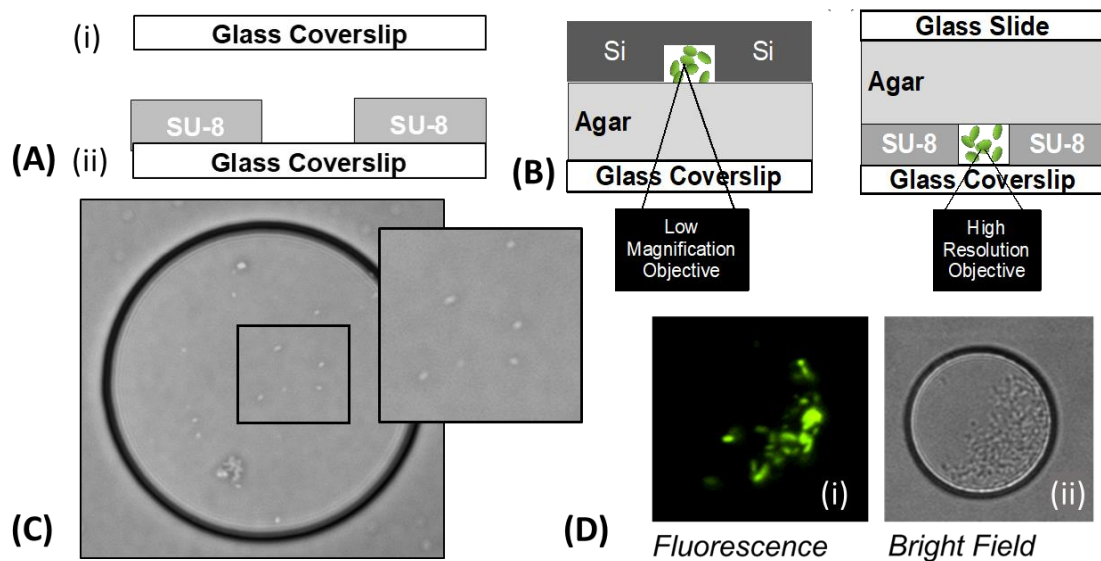


**Figure 2.2.2: Transparent microwell. (A) fabrication, (B) experimental assembly, and (C) imaging capability. (B) Schematic comparing imaging of silicon and transparent microwell platforms. On the left (B), the silicon microwell platform is oriented with the well opening facing down on an inverted scope. On the right (B), the wells are imaged through a glass coverslip and a hydrated layer of agar, which allows for direct imaging through the coverslip-substrate using higher resolution, shorter working distance objectives. (C) Image of cells with high-resolution brightfield microscopy subset image emphasizes the advantage of the transparent microwell platform's single-cell resolution (Olympus microscope, 40x). (D) Imaging capability with (i) fluorescence (Di), and (ii) phase contrast imaging.**

substrates may be more appropriate. Terminal test platforms call for many platforms, thus fabrication becomes very time intensive, especially when production yields of the glass coverslip platform are only 60%. Minimal efficiencies are captured with batch assembly and the fabrication rate is fifteen minutes per device, i.e. four devices per hour.

Quartz wafers offer an appealing alternative base substrate for the transparent microwell platform with only slight modifications to SU-8 photolithography methods. Multiple microwell platforms can be housed on a single quartz wafer, and then sectioned with a dicing saw (the structural integrity of the SU-8 microwells remains intact). A standard wafer thickness is 700  $\mu\text{m}$ , compatible with high resolution imaging, and durable. Fabrication of nine platforms per quartz wafer is roughly fifteen minutes, compared to the 135 minutes needed to generate nine glass coverslip platforms; a 90% increase in efficiency and 100% production yield.

Both quartz and glass substrates can be modified by nanofabrication techniques to accommodate different base materials for the microwell platform. For instance, metals can be deposited on the substrate, prior to SU-8 photolithography, by use of sputter or evaporation. SU-8 Photolithography methods are optimized to the specific platform. Substrates can be placed on a 180°C hot plate, before SU-8 photolithography, to facilitate SU-8 adhesion to nonideal substrates. This is recommended for SU-8 photolithography on glass. A post-lithography anneal (180°C hot plate) can smooth bubbling and reseal delamination. SU-8 photolithography can also form microwells at varying well depth.

### **Transparent Microwell with Parylene Lift-off Layer**

*A version of this work was originally published by M. Halsted, J. L. Wilmoth, P. A. Briggs, R. R. Hansen, D. P. Briggs, A. C. Timm, and S. T. Retterer:*

Halsted, M., Wilmoth, J. L., Briggs, P. A., Hansen, R. R., Briggs, D. P., Timm, A. C., and S. T. Retterer. (2016). Development of transparent microwell arrays for optical monitoring and dissection of microbial communities. *Journal of Vacuum Science & Technology B*. 34, 06K103. <https://doi.org/10.1116/1.4962739>

In addition to modifying the microwell base, features can be added on top of the SU-8 microwells. Examples of this include poly-dimethylsiloxane (PDMS) features (e.g. microfluidics) and parylene stencils. A transparent microwell platform, equipped with parylene lift-off layer, offers the same capabilities as the silicon microwell platform (section 2.1), plus the advantage of high-resolution brightfield microscopy. However, parylene adheres to the SU-8 epoxy and this presents fabrication challenges not encountered with the silicon microwell platform (parylene does not bind with silicon dioxide).

A low temperature plasma assisted atomic layer deposition (ALD) of silicon dioxide was deposited on the SU-8 microwells to create a separation layer between the SU-8 and parylene. A low temperature is required because the SU-8 epoxy may reflow and deform the microwells if temperatures exceed 150°C. The low-temperature plasma assisted atomic layer deposition (Plasma-ALD) was carried out in an Oxford FlexAL Atomic Layer Deposition System (Oxford Instruments, Abingdon UK). The ALD deposition process utilizes a Bisdiethylaminosilane (BDEA) precursor. Each ALD cycle consisted of a dose, purge, and plasma treatment step. Dosing of precursor was carried out under flow of Argon and Oxygen, 100 sccm and 1 sccm respectively, at 80 mTorr for 800 ms, followed by a purge (same conditions) with no precursor for 5 sec. Next, a treatment with an oxygen plasma (O<sub>2</sub>: 60 sccm, 15mTorr) applied for 2 s. and followed by 3 s of O<sub>2</sub> plasma treatment at 250 W for 3 s. Post plasma stabilization (Ar: 100sccm, 80mTorr) applied for 1.5 s before repeating the cycle. Silicon deposition was approximately 1.2 Å/cycle for each 12.3 s cycle. A minimum of 15 cycles are needed to prevent parylene adhesion.

Parylene was deposited on the samples using a Labcoter 2 parylene Deposition Unit Model PDS 2010 (Specialty Coating Systems, INC, Indianapolis, IN). Parylene C, with a thickness of  $1.5 \pm 0.5 \mu\text{m}$  (load of 3 g), mitigated the risk of parylene tears during lift-off. To define the photoresist mask for parylene etching and removal, a  $3 \pm 0.5 \mu\text{m}$  layer of a negative tone photoresist (NFR) (JSR Microphotoresist, Sunnyval, CA) was spun-cast onto the samples (2000 RPM, 45 s). The stencil mask (a slightly oversized version of the microwell mask) is aligned with the substrate with a SUSS + Micro Tec, MA6/BA6 and exposed for 6 s. The substrate was developed in CD-26 (Microposit MF, Malborough, MA) for 1 min, 20 s.

The parylene stencil is completed with an oxygen plasma etch (Oxford Instruments, Abingdon UK) (60 mTorr, 20oC, 100 sccm O<sub>2</sub>, 10W RF, 2000 W ICP), etch rate  $0.5 \mu\text{m}/\text{min}$ . The reactive ion etch oxygen plasma is vertically applied (i.e. z-axis) and etches carbon-based materials on the x-y-plane (i.e. the microwell base and corners). A summary of this process is outlined in Figure 2.2.3, A. The oversized mask exposes parylene along the top edge of the microwell, which is removed during the oxygen plasma etch, along with the parylene on the microwell base. A parylene sidewall likely remains on the microwell edge due to a vertically directed etch, but this has been proven to not affect lift-off.

The parylene layer is only  $1.5 \pm 0.5 \mu\text{m}$  thick, thus the lift-off layer is a delicate process (section 2.1). This is especially true for the stenciled parylene layer. During deposition, the parylene layer conforms to the material topography, and can be thought of as a continuous sheet hugging the well edge, sidewall, and base (Haus, 2016). Proper alignment of the second mask to the SU-8 wells is critical to successful lift-off. Misalignment can result in parylene remnants (Figure 2.2.4, A, B), or incomplete lift-off (Figure 2.2.4, C).



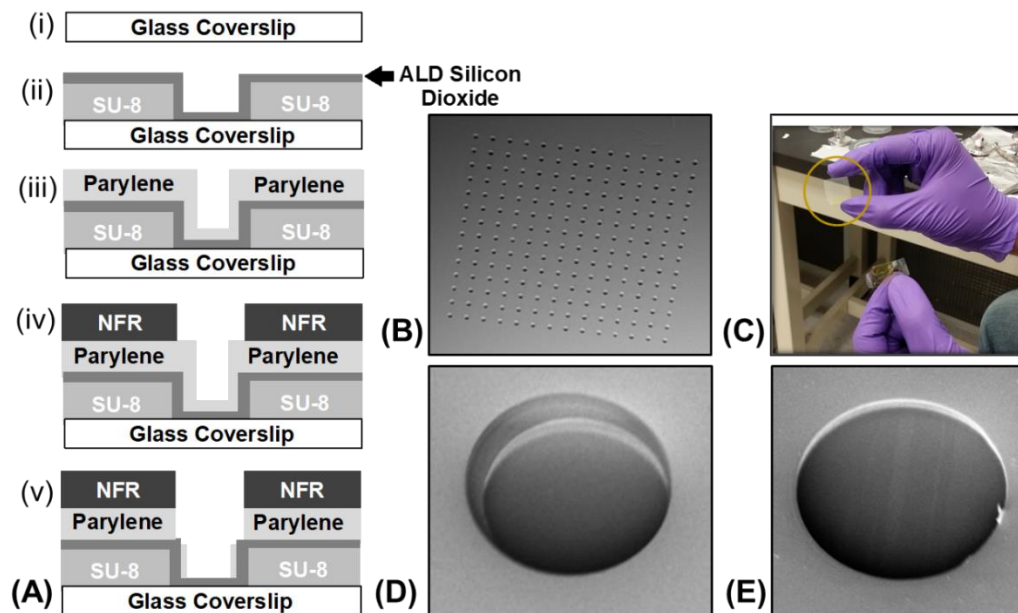


**Figure 2.2.3: Transparent microwell fabrication with parylene lift-off layer.**  
 (A) Fabrication is carried out with (i) dehydration bake on a coverslip substrate, (ii) SU-8 photolithography and deposition of a low-temperature ALD silicon dioxide film, (iii) parylene deposition, (iv) photopatterning of an aligned negative resist photomask, (v) an oxygen plasma etch to remove the exposed parylene. (B-E) Parylene lift-off layer: (B, D) scanning electron microscopy images of before lift-off and (C, E) after lift-off.

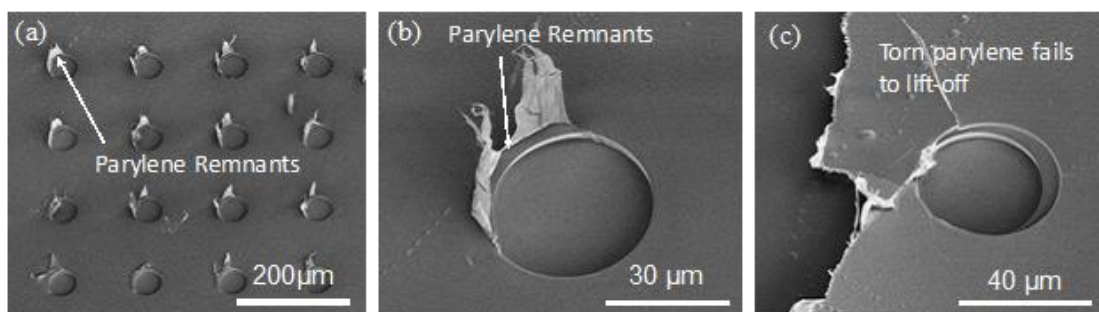


**Figure 2.2.4: Tearing of parylene lift-off layer with SU-8 wells is promoted by poor alignment.** (A, B) Remnants of parylene after lift-off and (C) tearing of large parylene section.

## **Transparent Microwell with Thermoplastic Substrate**

One key limitation to the silicon and transparent microwell platforms is accessibility to the biofilm for extraction of genetic material, proteins, metabolomes, etc. to use in “-omic” analysis. Simply breaking glass substrates does not allow for isolation of experimentally significant wells and removing biomass via microneedle is a delicate, cumbersome, and time-intensive extraction method.

To address this challenge, a transparent microwell platform was designed with Thermanox™, a polyolefin, as the base substrate. Thermanox™ can be sectioned with a microtome to isolate wells of interest. The device can even be sectioned with a razor blade if visible guides are included in the fabrication design. The section of Thermanox™ can be placed in a test tube for -omic analysis (Nkayasu et al., 2016; White et al., 2016).

Thermanox™ is uniquely suited for nanofabrication as many plastics are not compatible with the photolithography temperatures (i.e. softbake, post bake), nor can most plastics resist the solvents used to develop the photoresist. Thermanox™ can withstand temperatures up to 150°C (“Thermanox™ Coverslips”) and is compatible with alcohols, aldehydes, dilute acids hydrocarbons, and even has some resistance to chlorinated hydrocarbons. Plus, Thermanox™ was designed for compatibility with cell biology work, has a cell-friendly coating, and can withstand sterilization in the autoclave.

There are two approaches to Thermanox™ microwell matrices: build up or etch down. Unlike quartz and glass, which have limited etch rates, Thermanox™ is a carbon-based material and can be etched with an oxygen plasma etch. To avoid parylene binding with the Thermanox™, a separation layer of silicon dioxide is applied. An oxford FlexAI Atomic Layer Deposition (ALD) System (Oxford Instruments, Abingdon, UK) deposited roughly 25 nm of silicon dioxide at a rate of 1.2 Å/cycle per the methods specified in Halsted et al. (2016). Thermanox™ is

rated to 145°C, but because the material is under vacuum pressure in the ALD system, Thermanox™ can withstand the 150°C temperature.

Next, parylene C precursor (3 g load) was deposited on Thermanox™ with a Labcoter 2, Specialty Coating Systems on to yield a thin Parylene layer ( $1.5 \pm 0.5$   $\mu\text{m}$  thickness). A negative tone resist (JSR Micro Microphotresist, Sunnyvale, CA) was spun-cast onto the sample at 700 RPM. A two min soft bake followed and a three s exposure Quintel UV Contact Aligner (Rochester, NY) at a power of  $\sim 10$   $\text{mW}/\text{cm}^2$  (365nm). The substrate was placed on the hot plate (115°C) for two minutes and developed in CD-26 (Microposit MF, Malborough, MA) for 1 min 20 s. The parylene layer was etched with an oxygen plasma etch (Oxford Instruments, Abingdon UK) (60 mTorr, 20°C, 100 sccm O<sub>2</sub>, 10W RF, 2000 W ICP), followed by 6 second C<sub>4</sub>F<sub>8</sub> & O<sub>2</sub> plasma to remove the 25 nm silicon dioxide layer. Lastly, two iterations of a five-minute oxygen plasma were applied to the substrate (0.5  $\mu\text{m}/\text{min}$  etch rate). The two separate oxygen plasma applications minimized stress and deformation of the substrate. This achieved a total well (Thermanox™ & parylene layer) with an approximate depth of 5  $\mu\text{m}$ . Figure 2.2.5, A illustrates the fabrication methods.

Thermanox™ is compatible with brightfield and fluorescence imaging (Figure 2.2.5, C and D). However, parylene and NFR are auto fluorescent. The parylene stencil yield an auto fluorescent ring (i.e. white ring) around the microwell in Figure 2.2.5, D. This could interfere with data extraction from cells with low fluorescent signals. One unforeseen advantage of the Thermanox™ platform is the surface roughness created by the oxygen plasma etch (Figure 2.2.5, E, F). Surface roughness is a desirable surface condition for certain bacterial species (Friedlander et al., 2013; Hochbaum et al., 2012; Crawford et al., 2012; Jeong et al., 2013; Song and Ren, 2015; Cheng, Feng, and Moraru et al., 2019). Independent of the microwell platform, Thermanox™ has potential applications for studying surface roughness and cell attachment of different bacterial species.

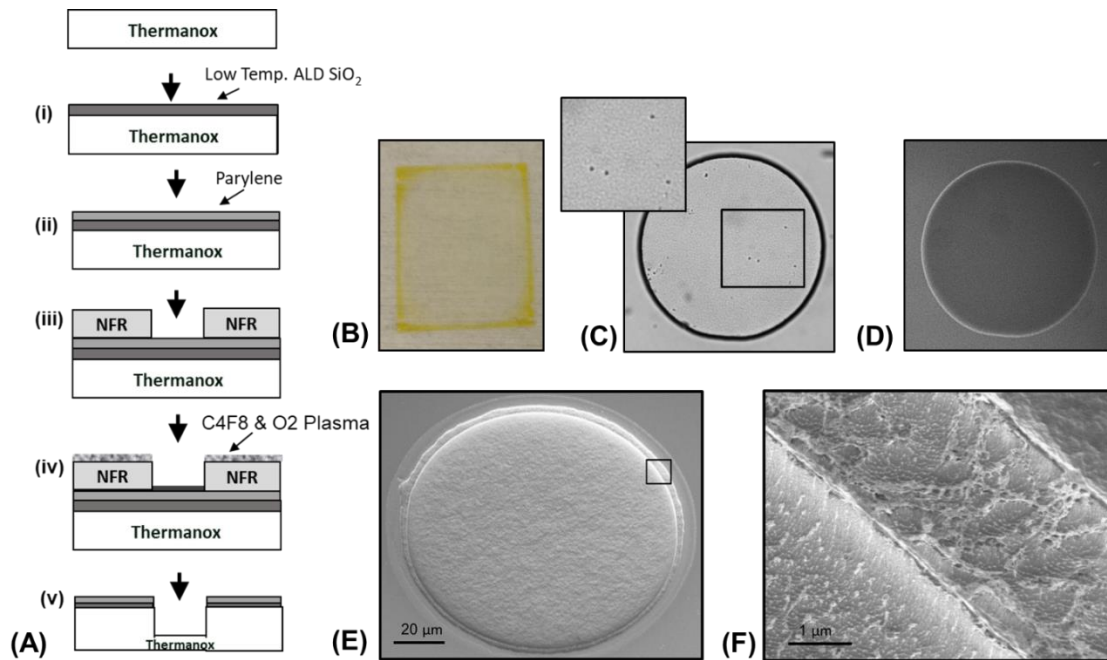


**Figure 2.2.5: Thermanox™ microwell platform. (A) Fabrication begins with a (i) low-temperature ALD silicon dioxide film, (ii) parylene deposition, (iii) photopatterning of a negative resist photomask, (iv) an oxygen plasma removed the exposed parylene and etch the microwell into the Thermanox™; diagram is not drawn to scale. (B) Image of Thermanox™ device; (C) brightfield microscopy image of the Thermanox™ microwell, inset demonstrates the single-cell resolution; (D) fluorescence image of Thermanox™ microwell; (E, F) scanning electron microscopy image of a Thermanox™ microwell and insert highlighting surface roughness.**

## 2.3 Electrochemical Surface Plasmon Resonance Platform

*This work was part a collaboration with The Naval Research Lab (NRL) and The Center for Nanophase Material Sciences (CNMS) at Oak Ridge National Laboratory (ORNL). Fabrication of the platform took place at the Nanofabrication Research Laboratory, ORNL as part of the CNMS User Program. The Microbial Electrochemistry group, NRL performed electrochemical surface plasmon resonance testing. This collaboration included participation in the Navel Research Enterprise Internship Program (summer, 2017), and the opportunity to intern with the Microbial Electrochemistry group, NRL. Funding for the internship was provided by the American Society for Engineering Education.*

Nanofabricated platforms have been used to conduct electrochemical experiments. The microenvironment can increase resolution and elucidate the mechanisms of extracellular electron transfer. In 2010, Jiang et al. used nanoelectrodes in a polydimethylsiloxane (PDMS) chamber to determine the extracellular electron transfer mechanism of *Shewanella oneidensis*. A few years later, Jiang et al. calculated the current of a single *Geobacter sulfurreducens* bacterium in a SU-8 microwell-nanoelectrode matrix (2013). The microwell-nanoelectrode platform consisted of 16 microwells each with a pair of finger electrodes and a total of 32 wires connected along the platform edge (Jiang et al., 2013). While an impressive setup, this number of wire connections is cumbersome and impractical for mass experimentation. This work presents an alternative approach to parallel, electrochemical measurements by use of electrochemical surface plasmon resonance (ESPR). Nanofabrication can segment the ESPR slide to enable high-throughput data collection.

Surface plasmon resonance (SPR) analyzes samples in real-time, without labels, and is recognized as a highly sensitive biosensor platform (Tang, Zeng & Liang, 2010; Piliarik, Vaisocherova & Homola, 2009; Zeng et al., 2014). Surface plasmons

are electromagnetic waves at a metal-dielectric interface, and resonance is an oscillating signal (Wang et al., 2010; Tang, Zeng, and Liang, 2011). Surface plasmon resonance measures changes to the surface of a dielectric-metal interface from reflection of a light source; the light source is beamed through a prism and received by a detector (Tang, Zeng, and Liang, 2011; Li and Zhong, 2012) (Figure 2.3.1). Surface plasmon resonance imaging (SPRi) correlates changes in the surface plasmons to changes in pixel intensity (Li and Zhong, 2012). Specifically, a charge-coupled detector (CCD) camera detects changes in the intensity of the reflected light beam with the angle of incidence, as shown in Figure 2.3.1 (Li and Zhong, 2012).

Electrochemical surface plasmon resonance (ESPR) imaging combines this spectroscopic method with a potentiostat to generate a highly sensitive platform for interrogating electrochemical systems (Wang et al., 2010; Shan et al., 2017). The gold thin-film on the SPR specialty glass slide doubles as the working electrode and the metal-dielectric surface required for SPR measurements (Shan et al., 2017; Tang, Zeng & Liang, 2010). The potentiostat applies a voltage potential to the SPR platform and this prompts electron flow in an electrochemical setup (working electrode, reference electrode, counter electrode, electrolytic solution). Electron transfer to the gold surface is detected by the SPRi system and monitored by change in pixel intensity. Golden et al. leveraged this system to study electron transfer between *G. sulfurreducens* biofilms and the gold electrode (2018). Golden et al. confirmed the change in pixel intensity corresponds to the electron transfer at the biofilm-electrode interface (2018).

This work leverages nanofabrication techniques to construct (micro)wells on an SPR specialty glass slide to create an ESPR platform. The microwells confine the biofilm and enables parallel measurements. Fabrication of three different ESPR well platforms is described in this section. Feasibility testing of the ESPR microwell platform can be found in section 4.2.

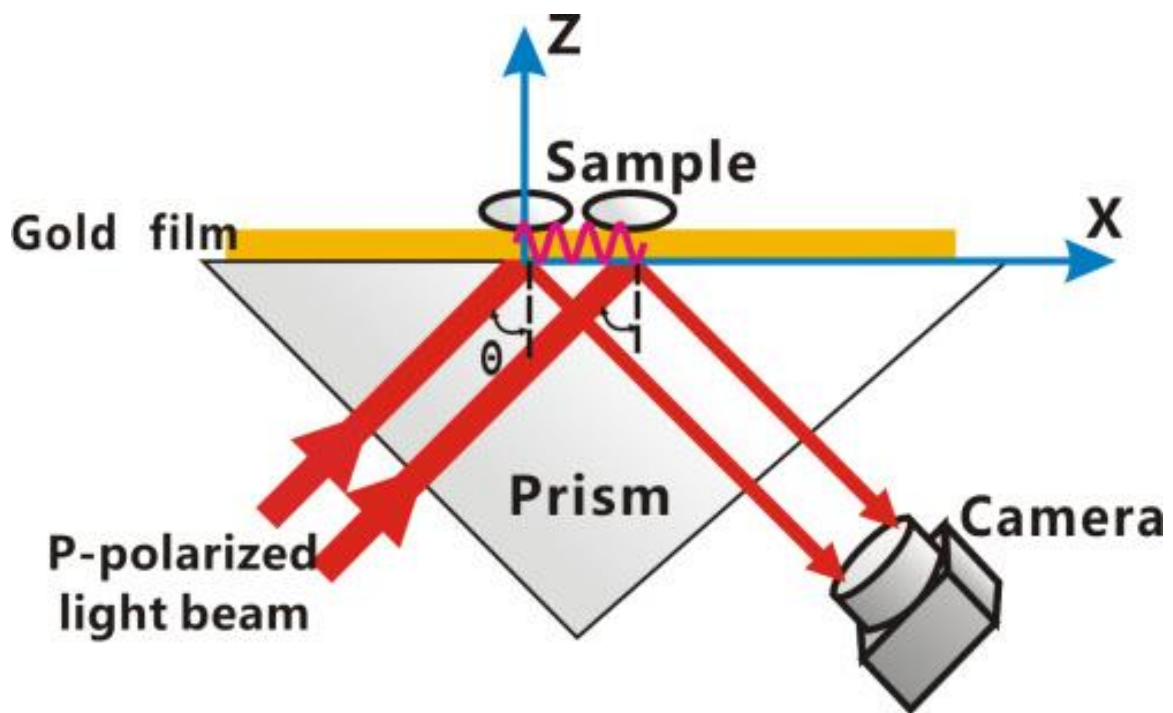


Figure 2.3.1: Surface plasmon resonance imaging (SPRi) diagram, where the pink waves represent changes to the surface plasmons brought on by attachment of the sample. Source: Li and Zhong, 2012.

### **ESPR Microwell Platform**

SU-8 2015 (MicroChem, Westborough, MA) was spun-cast on standard SPR gold substrates (GWC Technologies) at 3000 RPM, 60 s. To improve adhesion, the SPR slide was placed on 180°C for at least an hour prior to SU-8 photolithography. Following the SU-8 spun-cast, the substrate was placed on a 95°C hotplate for two min, exposed at 190 mJ/cm<sup>2</sup> with a SUSS + Micro Tec, placed on a 65°C hot plate for 60 s, and returned to the 95°C hotplate for 3 min. The platform was developed for 60 s using SU-8 Developer (MicroChem, Westborough, MA) via spray-puddle method, rinsed with SU-8 Developer and isopropanol (IPA), followed by a second anneal at 180°C, 15 min. Fabrication is summarized in Figure 2.3.2, A.

The microwell platform segments the SPR platform to enable high-throughput data collection. The 7 X 7 ESPR microwell platform in Figure 2.3.2, B produced 49 individual voltammograms of the *G. sulfurreducens* biofilms, each corresponding to the 49 microwells (results are presented in section 4.2). This high-throughput platform magnifies the output of experimental data, capturing natural variation in the biological phenomena and enabling statistical rigor.

### **ESPR PDMS Well Platform**

Parallel experimentation of different bacterial biofilms (e.g. mutant biofilms, bacterial species) requires deterministic seeding. Microwell platforms require special experimental equipment to execute deterministic seeding on the microscopic scale, such as a bacterial bioprinting system ink jet printer for biological samples (Srimongkon et al., 2015; Mohammadi and Rabbani, 2018). Alternatively, the well size can be increased to accommodate deterministic seeding with a pipette.

Wells with as little as 2 mm diameter, 2 mm height, are compatible with deterministic pipette seeding. Bacteria cultures are filled in each well, and cells



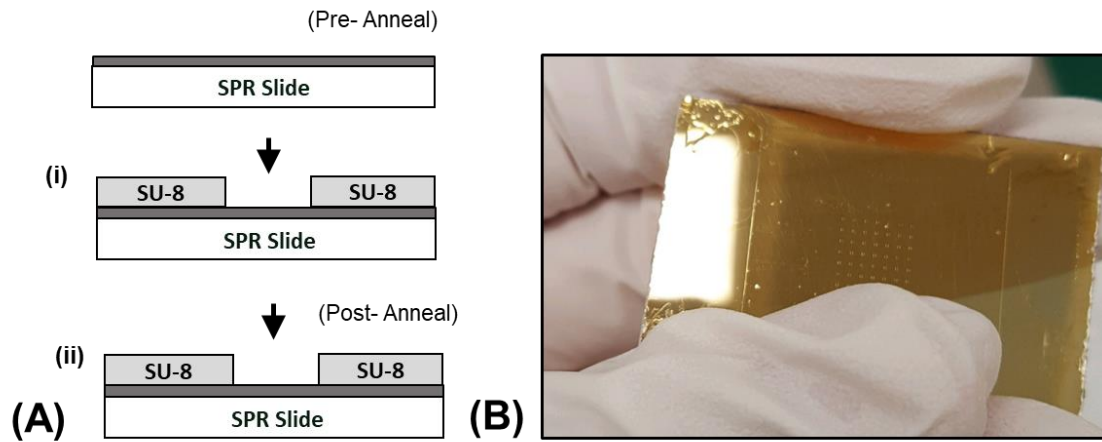


**Figure 2.3.2: ESPR microwell platform. (A) Fabrication of microwell structure on gold SPR substrate with SU-8 Photolithography. (B) Example ESPR microwell configuration with 7 X 7 200  $\mu\text{m}^2$  square wells.**

attach to the microwell. After a designated period of time, the excess liquid culture is removed, and the platform is placed in the ESPR system. The ESPR system can accommodate a three by three matrix of 2 mm diameter wells. Initially, the wells were fabricated with SU-8 photolithography, but there were low fabrication yields (~20%) for these design constraints. Soft lithography offered a reliable fabrication method for this design. Figure 2.3.3 compares fabrication methods for the various SU-8 photolithography and soft lithography platforms.

Poly-dimethylsiloxane (PDMS) (Sylgard 184, Dow Corning, Midland, MI) was mixed at a 5:1 ratio, prepolymer to crosslinker, and poured in a petri dish (2 mm depth). The petri dish of PDMS was placed under vacuum for twenty minutes to degas the material, then cured in an oven (75°C, 1 hour). A razor blade extricated 15 mm squares from the PDMS slab. The PDMS squares were placed on a well matrix guide and punched with a 2 mm biopsy punch tool. PDMS inking technique adhered the PDMS wells to the SPR slide. The inking technique mixed PDMS at a 10:1 prepolymer to crosslinker to adhere the PDMS well matrix to the substrate.

Approximately 5 mL PDMS was spun-cast on a 4-in diameter silicon wafer (3000 rpm, 6 min) and the PDMS well matrix was stamped (with the PDMS adhesive) on the SPR slide. The device was cured overnight in a 75°C oven and the samples were shipped to the Naval Research Lab for ESPR experimentation with *G. sulfurreducens*. Figure 2.3.4 outlines the fabrication steps. A thin-film of gold (7nm titanium adhesive layer, 38 nm gold) was deposited on the patterned substrate with a Thermionic VE-240 electron beam evaporator. SU-8 photolithography or soft lithography can create the wells. Soft lithography is recommended for applications that require well height exceeding 50  $\mu\text{m}$ , such as seeding unique cultures of bacteria for parallel testing. The fabrication process follows the ESPR PDMS well platform. The punctured PDMS are “stamped” with liquid PDMS and carefully aligned with the gold electrode. Once placed, the punctured PDMS cannot be adjusted, less the liquid PDMS may leave a residue that could with the signal.

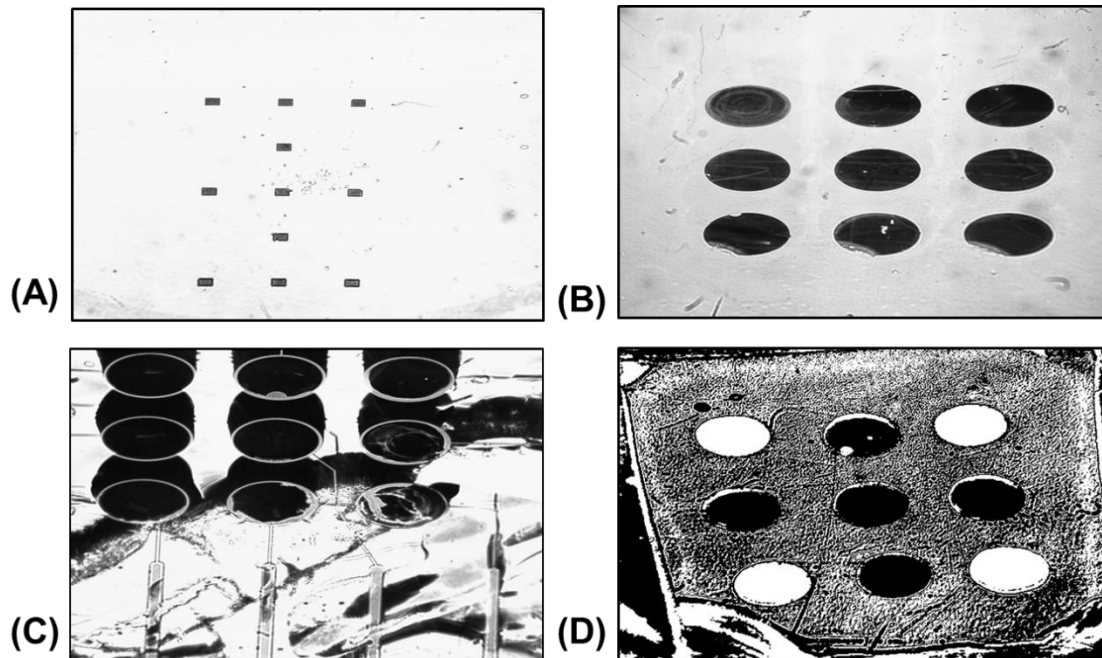


**Figure 2.3.3: ESPR well platforms in the SPR chamber: (A) 400  $\mu\text{m}$  square, SU-8 2015 microwells, high quality fabrication; (B) 2 mm diameter, SU-8 2050 microwells, decent fabrication quality with small delamination edge effects on the first row; (C) 2 mm diameter, SU-8 2050 microwells on multielectrode device, poor fabrication quality and delamination; (D) 2 mm diameter, Poly-dimethylsiloxane (PDMS) wells; the white wells indicate presence of a biofilm.**

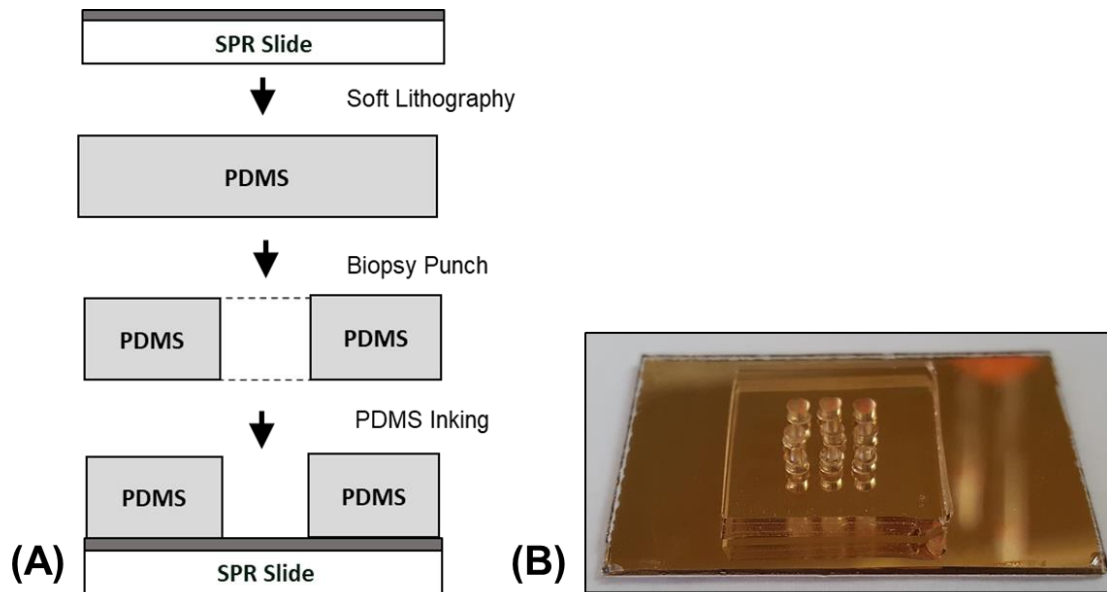


**Figure 2.3.4: ESPR PDMS well platform. (A) Fabrication: (i) 5 prepolymer: 1 cross-linker mixed and cured PDMS at 75°C; (ii) Biopsy punch generated 2 mm well; (iii) PDMS inking technique adhered PDMS wells to SPR slide. (B) Image of ESPR PDMS well platform (pre-wire attachment).**

## ESPR Multielectrode Well Platform

The gold film on the SPR slide served as the working electrode for entire ESPR platform, hence only one voltage potential can be applied to the system. This platform patterns gold into 9 individual electrodes for each well and paired with a multi-channel potentiostat to simultaneously apply different voltage potentials (Figure 2.3.5). The ESPR multielectrode well platform can be seeded with unique bacterial cultures to conduct individual electrochemical experiments. The platform has promising applications for electrochemical experiments with *G. sulfurreducens* cytochrome mutant biofilms. A negative tone photoresist (NFR) (JSR Microphotoresist, Sunnyval, CA) was spun-cast onto the SPR slide (2000 RPM, 45 s) to generate a multielectrode pattern.

The substrate was placed on a 95°C hot plate (90 s), exposed 6 s with SUSS + Micro Tec, MA6/BA6 and then placed on a 115°C hot plate. The substrate was developed in CD-26 (Microposit MF, Malborough, MA) for 1 min, 20 s. SU-8 photolithography with the SUSS + Micro Tec MA6/BA6 contact aligner offers micron-scale alignment resolution. However, dense layers of SU-8 can delaminate from glass, thus there is a low fabrication yield. An example of SU-8 delamination in the SPR chamber is shown in Figure 2.3.3, C. SU-8 photolithography is recommended for multielectrode platform applications compatible with stochastic seeding, and SU-8 well depth need not exceed 50  $\mu\text{m}$ .

A feasibility experiment was performed with ferrocene to demonstrate the platform's ability to track individual signals in the wells. A full description on the workings of the ESPR system and the experimental setup are included chapter 4 (section 4.2). The patterned gold creates individual electrodes, each connected to a wire-attachment pad. Wires were connected to the pads for select well-electrodes (3, 5, 8), and cyclic voltammetry (CV) was performed (Figure 2.3.6). The entire platform was submerged in an electrolytic solution (ferrocene), with a

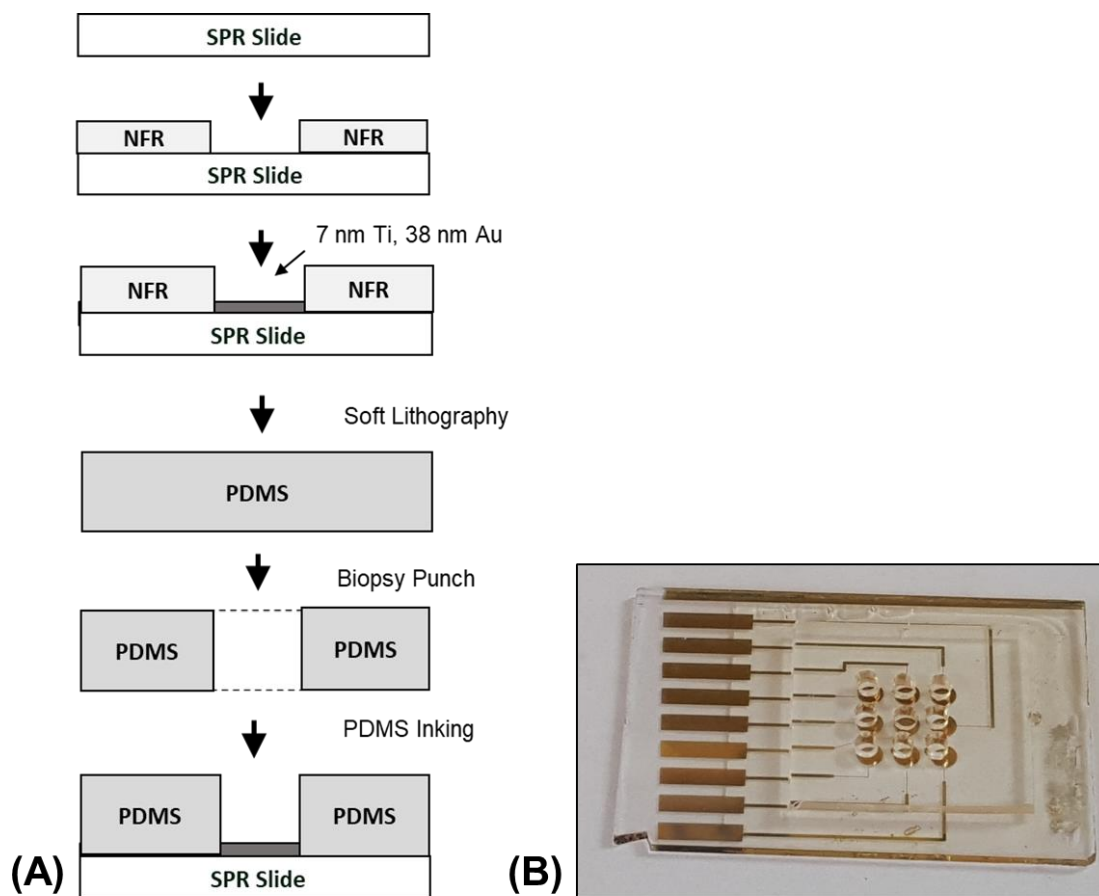


**Figure 2.3.5: ESPR multielectrode well platform (A) Fabrication: (i) negative tone photoresist (NFR) photolithography; (ii) thin-film gold (37 nm) deposited on SPR glass slide; (iii) 5 prepolymer: 1 cross-linker mixed and cured PDMS at 75°C; (iv) Biopsy punch generated 2 mm well; (v) PDMS inking technique adhered PDMS wells to SPR slide. (B) Image of ESPR multielectrode well platform (pre-wire attachment).**

counter electrode and connected to the SPRi system (experimental setup is detailed in section 4.2). CV scans were only detected in the intended wells, and this demonstrates the ability of the platform to apply unique voltages to each well (Figure 2.3.6).

## **2.4 Surface Functionalization and Patterning**

Material coupons are commonly used in detrimental biofilm studies, such as contamination in food processing and biomedical implants (Puckett et al., 2009; Das et al., 2008; Schultza et al., 2012; Kocot and Olszewska, 2017; Mosquera-Fernández et al., 2014; Mosquera-Fernández et al., 2016; Guo et al., 2019; Rieu et al., 2008; Marsh, Luo, and Wang, 2015). This approach is convenient for man-made surfaces, but natural surfaces are not so lucky. The study of biofilms on natural surfaces, like plant roots or soil particles, requires a bit of ingenuity. Nanofabrication offers the ability to mimic select features of natural surfaces.

Nanofabrication techniques present a mechanism for modifying and controlling surface features for biofilm studies. Approaches to modifying surface chemistry include atomic layer deposition (ALD), plasma enhanced chemical vapor deposition (PECVD), and thin-film deposition via electron-beam physical vapor deposition (EBPVD). Self-assembled monolayers (SAM) can modify surfaces with thiol and silane chemistries (Galbiati, 2016; Friedlander et al., 2015; Want et al., 2013; Glass et al., 2011; Tan and Craighead, 2010; Timm et al., 2015; Privett et al., 2011). Surface topography can be controlled with alteration of silicon substrates, using photolithography, or advanced lithographic techniques, and plasma etching (Friedlander et al., 2013; Truong et al., 2010; Ammar et al., 2015; Bhattacharjee et al., 2017; Hochbaum and Aizenberg, 2010; Epstein et al., 2011). Patterning the surface alterations allows for side-by-side comparison in biofilm studies (Tan and Craighead, 2010; Timm et al., 2015; Hansen et al., 2014; Murphy et al., 2015).

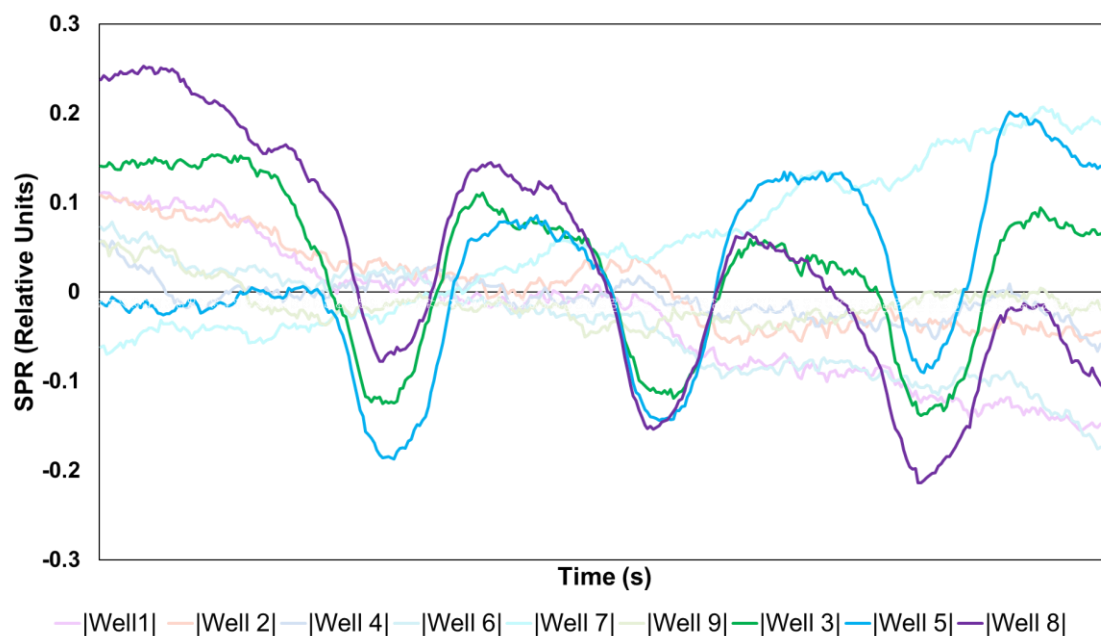


**Figure 2.3.6: Cyclic voltammetry feasibility experiment with ferrocene on ESPR multielectrode well platform. Cyclic voltammetry was performed on wells 3,5,8 at a scan rate of 1 mV/s.**



## **Patterned Surface Treatments via Parylene Stencil**

Parylene stencils exist in a variety of applications, such as patterning bacteria with a microfluidic device, patterning biomolecular arrays with an inkjet printer, even assembling stochastic communities of bacteria in microwell platforms (Tan and Craighead, 2010; Tim et al., 2009; Timm et al, 2015; Timm et al., 2017). The transparent microwell platform incorporated a parylene stencil, and this design laid the foundation for other experimental platforms. This modified design substitutes NFR with SU-8 negative photoresist epoxy to improve durability. The epoxy photoresist can also supply depth and further expand the breadth of application.

A  $1.5 \pm 0.5 \mu\text{m}$  layer of Parylene C was deposited on glass slides (Labcoater 2 parylene Deposition Unit Model PDS 2010, Specialty Coating Systems, INC, Indianapolis, IN). SU-8 2005 (MicroChem, Westborough, MA) was spun-cast on the parylene-glass substrate at 5000 RPM, 45 s. The substrate was baked at  $95^\circ\text{C}$ , 90 s, and exposed for  $150 \text{ mW/cm}^2$  with a SUSS + Micro Tec, MA6/BA6. The substrate was returned to the hot plate for an additional 90 s then developed with SU-8 Developer (MicroChem, Westborough, MA) for 60 s, rinsed with SU-8 Developer and isopropyl alcohol (IPA), then dried with pressurized nitrogen. A five-minute oxygen plasma (Oxford Instruments, Abingdon UK) (60 mTorr,  $20^\circ\text{C}$ , 100 sccm  $\text{O}_2$ , 10W RF, 2000 W ICP) stenciled the Parylene (etch rate of  $0.5 \mu\text{m/min}$ ). This parylene stencil design can be applied to the pattern of tissues, such as collagen, for biofilm and tissue engineering studies. A parylene stencil with an epoxy depth adds a mechanism for enclosing tissues. An example of this is found in Figure 2.4.1, B where an SU-8 parylene stencil patterned collagen onto glass and the SU-8 depth ( $5 \pm 0.5 \mu\text{m}$ ) contained collagen wetting and promoted a uniform thickness across the surface. The parylene stencil can also assess the influence of physiochemical forces on cell attachment with side-by-side comparisons as parylene lift-off is compatible with silane deposition. The silane bonds to the exposed substrate (e.g. silicon) and functionalizes the exposed surface. Figure 2.4.2 explains the self-assembled monolayer formation

mechanism. Preliminary experiments patterned PFOTS and consequently patterned *Pantoea* sp. YR343 cell attachment (Figure 2.4.1, C).

*Pantoea* sp. YR343 biofilm forms on the hydrophobic surface (PFOTS) and there is little attachment to the hydrophilic, silicon substrate. A continuation of this work might reveal whether cell appendages, like flagella, can overcome undesirable surface properties to connect nucleation sites and propagate a biofilm across an undesirable surface. Varying pitch and diameter in a matrix of patterned PFOTS circles could pin-point the distance for which the *Pantoea* sp. YR343 flagella might be able to connect to adjacent nucleation sites.

### **Patterned Carbon Nanospikes**

Sheridan et al. developed carbon nanospikes (CNS), an ideal fuel cell material with a high degree of surface area (2014). In sum, a plasma enhanced chemical vapor deposition (PECVD), in the presence of acetylene ( $2\text{H}_2$ ) and ammonia ( $\text{NH}_3$ ), grows the CNS at  $650^\circ\text{C}$ , and a full methods description and characterization can be found in Sheridan et al. (2014). Time is correlated to CNS thickness, and 3-5 min yields transparent films of CNS when grown on quartz (*unpublished work from the Center for Nanophase Material Science Nanofabrication Research Lab*).

CNS was explored as a microelectrode material for study of *G. sulfurreducens* biofilm. This interest arose because carbon cloth is a popular, inexpensive electrode material in bioelectrochemical system, and more importantly, both materials have ample opportunity for electron exchange because of the high degree of surface area in each material (Xie, Criddle, and Cui, 2015; Sheridan et al., 2014; Beyenal and Babauta, 2015). The CNS material is biologically appealing as many bacteria prefer attachment to surfaces with average roughness ( $R_a$ ) 10-100 nm (Donlan, 2002). The CNS may even provide a source of nitrogen from the ammonia in the PEVCD process, and *G. sulfurreducens* is capable of fixing nitrogen in soil environments (Nagarajan et al., 2013).

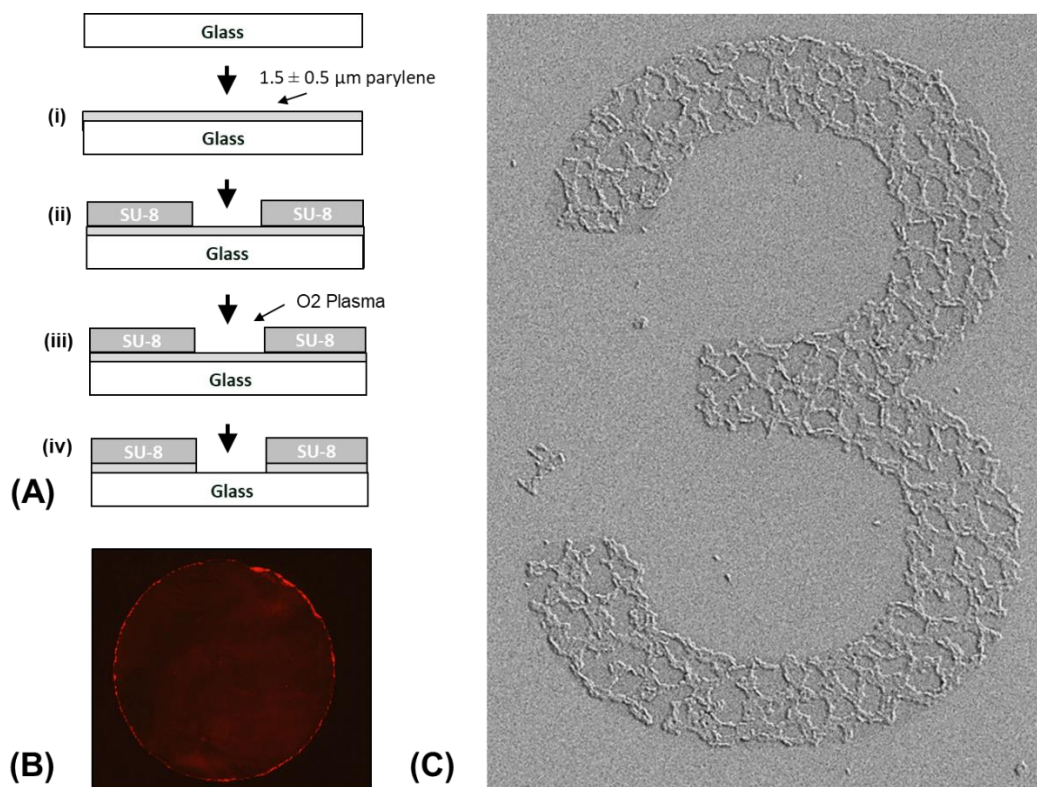


**Figure 2.4.1: Parylene stencil with SU-8 epoxy photoresist. (A) Fabrication:**  
 (i) Parylene deposition, (ii) photopatterning of SU-8 negative resist photomask, (iii) an oxygen plasma to remove the exposed parylene. (B) Patterned collagen; (C) *Pantoea* sp. YR343 attachment to patterned PFOTS on silicon substrate.

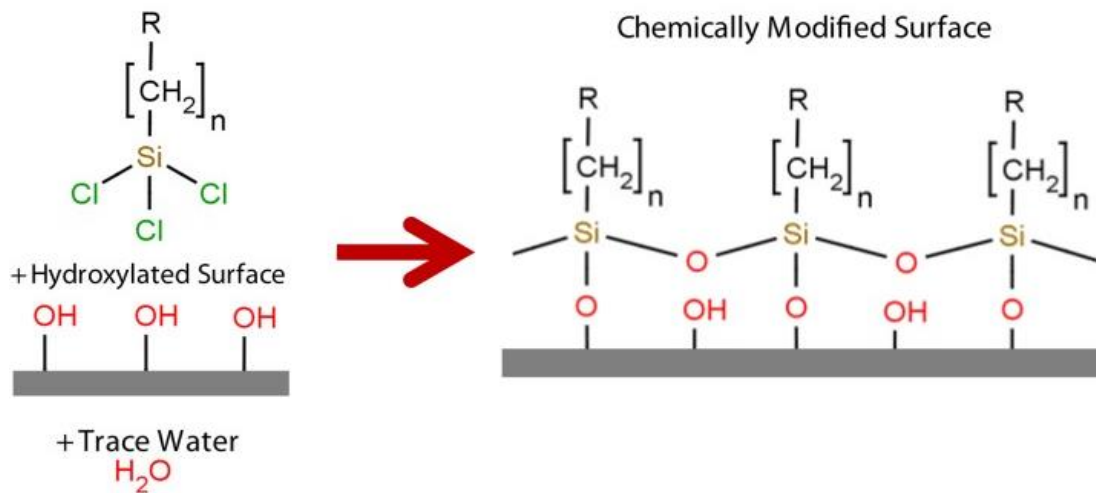


**Figure 2.4.2: Formation of self-assembled monolayers on hydroxylated surfaces in the presence of an organosilane and trace amounts of water. The tail, represented by the “R”, functionalizes the surface while the opposing end bonds to the surface. Source: Glass et al., 2011.**

Preliminary experiments found *G. sulfurreducens* readily attached to CNS (Figure 2.4.2).

To utilize CNS as a microelectrode material, CNS must be patterned on the substrate (Figure 2.4.3). Just as with the parylene stencil, a Reactive Ion Etch Oxygen plasma can etch CNS because it is a carbon-based material. Photolithography directed the oxygen plasma and successfully patterned the CNS while preserving CNS surface roughness (Figure 2.4.3 C). S1818 was spun-cast on 20 mm square CNS substrates at 3000 RPM, 45 s, followed by a one-minute bake on a 150°C hot plate. The substrate was exposed for 5 s in a SUSS + Micro Tec, MA6/BA6 contact aligner and developed in Microposit MF CD-26 developer (Malborough, MA) for 2 min. An Oxford Instruments Plasmalab System 100 Reactive Ion Etcher (Abington, Oxfordshire, UK) carried out the oxygen plasma etch at a recommended 3:5 ratio of CNS growth to oxygen plasma. It is important to note that small quartz substrates (i.e. 20 mm squares) can experience edge effects with disproportionate CNS thicknesses. In such instances, multiple oxygen plasmas of three-minute intervals are recommended. This allows for inspection of the substrate and appropriate levels of CNS removal. Acetone is used to remove residual NFR, with up to 2 min sonication. This method was tested with a 70 µm width stripped pattern and imaged with a Zeiss Scanning Electron Microscope (Figure 2.4.3, A).

This work demonstrates the ability of CNS to serve as a(n) (micro)electrode material. The CNS was not selected for the ESPR multielectrode well platform because the SPR system requires a metal-dielectric interface. The patterned CNS platform shows promise for applications beyond BES, such as culturing mammalian cells (unpublished work).

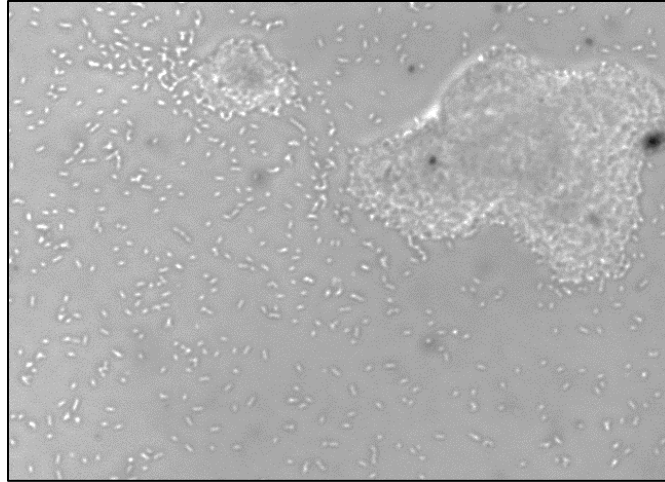


**Figure 2.4.3: *G. sulfurreducens* attachment to CNS after six hours, brightfield microscopy, 40x objective. Cells were grown at 30°C, vertical positioned substrate in a 30 mL volume, inoculated at 0.05 OD.**

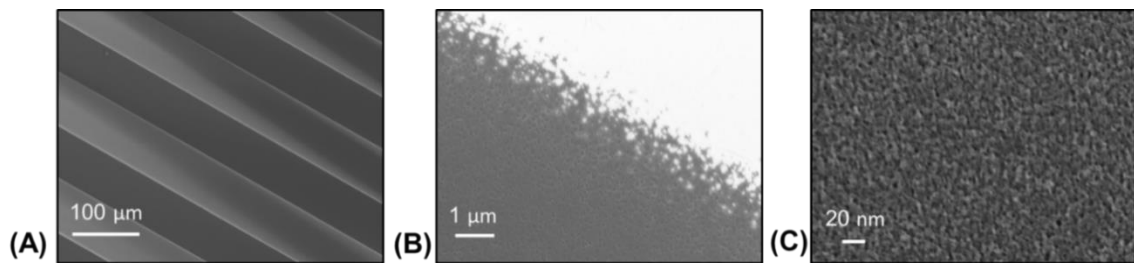


**Figure 2.4.4: Patterned Carbon Nanospikes, imaged with Zeiss Scanning Electron Microscopy, coated with 5 nm chromium.**

### **CHAPTER THREE**

## **QUANTIFY CELL ATTACHMENT IN NOVEL PLATFORMS: IMAGE PROCESSING ALGORITHMS**

Image processing tools have become readily available and quite sophisticated in recent years, aiding microbiology with extraction of quantitative information from microscopy images. Image processing is made possible by digital images, which are visual matrices that use pixels to store information on intensity and/or color. Even though a pixel looks like a square in a zoomed digital picture, the pixel is an assigned value, not a measure of area. Image processing uses a variety of functions to manipulate the values in the visual matrix; a detailed explanation can be found in Murphy and Davison (2012).

One key concept in image processing is threshold functions which identify foreground objects (based on differences in pixel intensity) and reassigns the pixels as white or black (binary image) in accordance with the image foreground and background (Ljosa and Carpenter, 2009; Cardullo, 2003). The binary image then allows particle analysis functions to quantify objects (black particles) in the region of interest (white background) and report metrics such as particle size, particle area, location, area coverage, etc. (Choudhry, 2016; Clarke et al., 2010; Cai et al., 2011). Particle analysis functions offer a high-throughput approach to performing cell counts (Guzmán et al., 2014; Larimer et al., 2016). An understanding of the image processing fundamentals can be used to tailor algorithms for specific experimental conditions and imaging conditions, such as gradients in the background of a brightfield image brought about by uneven illumination.

Many automated image processing algorithms exist for high-throughput image processing. These ready-to-use algorithms often demand little of the user in exchange for limited application (Guzmán et al., 2014; Larimer et al., 2016).

Microfluidic and nanofabrication platforms call for customized image processing algorithms to account for the unique features of the platform while measuring bacteria response (Mueller et al., 1992; Verma et al., 2012; Timm et al., 2016; Hansen et al., 2016). Image processing software like ImageJ facilitates creation of custom algorithms with a user-friendly interface. This section describes two image processing algorithms each designed for bacterial studies in novel platforms.

### **3.1 Quantify Cell Attachment in a Transparent Microwell Platform**

Particle analysis functions offer a high-throughput approach to enumerate cell attachment in the early stages of biofilm formation (Choudhry, 2016; Clarke et al., 2010; Cai et al., 2011). Particle analysis functions can be paired with fluorescence and high resolution brightfield microscopy, provided processing functions can create representative binary images. The algorithm presented here leverages edge detection, threshold, and particle analysis functions to quantify cell attachment to the base of a microwell (section 3.2). The algorithm then uses a series of filtering techniques to generate a robust mask of the microwell. This serves as the region of interest, where a particle analysis function is applied to quantify cell attachment within the well. Hundreds of unique microwell images can be processed within minutes.

High-resolution brightfield microscopy eliminates the need for synthetic fluorophores or engineering bacteria to express fluorescent proteins. This is beneficial for bacterial studies with autofluorescence materials, such as SU-8 photoresist epoxy, which can overpower the cell signal. On the downside, brightfield microscopy is susceptible to poor image quality, such as uneven illumination, low-contrast, and noisy backgrounds (Choudhry, 2016). These deficiencies can disable the threshold function from distinguishing foreground



objects correctly and prevent the use of a standard threshold in a batch of images (Choudhry, 2016). Edge detection functions can overcome these challenges with brightfield images (Choudhry, 2016). This function exaggerates differences in pixel intensity and draws attention to foreground images (Ljosa and Carpenter, 2009; Verma et al., 2012; Choudhry, 2016). Edge detection functions can produce results nearly identical to manual cell counts (Choudhry, 2016).

The specific image processing steps are outlined in Figure 3.1.1 with ImageJ function names. First, an edge detection function (“Find Edges”) exaggerates differences in pixel intensity to apply a threshold function (“Triangle Dark”) and generate a binary image (Figure 3.1.1, step 1-3). The foreground features are black, the background is white. The binary image is adjusted using binary specific functions (e.g. “Dilate”, “Erode”, “Fill Holes”) and image filters (“Median”, “Minimum”) to create a representative mask of the well (Figure 3.1.1, step 4-6). The image filter functions change the value of the pixel intensity using information from the surrounding pixels, denoted by the radius measure. The particle analysis function (“Particle Analysis”) creates a mask from the microwell, which serves as the region of interest (ROI) when counting the attached cells. The microwell mask is stored as an ROI in the particle manager and is applied to a duplicate of the original image (Figure 3.1.1, step 7-8).

The second image undergoes similar processing steps. Edge detection (“Find Edges”) and threshold functions (“Triangle Dark”) are applied to the image within the microwell mask to capture cells as the foreground object in a binary image (Figure 3.1.1, 9-10). Filters (“Median”) smooth the image. The particle analysis function (“Particle Analysis”) counts the cells, determines cell size, location, total area coverage, etc. (Figure 3.1.1, step 12). The particle analysis function allows the user to decide if particles (cells) on the border of the ROI are counted.

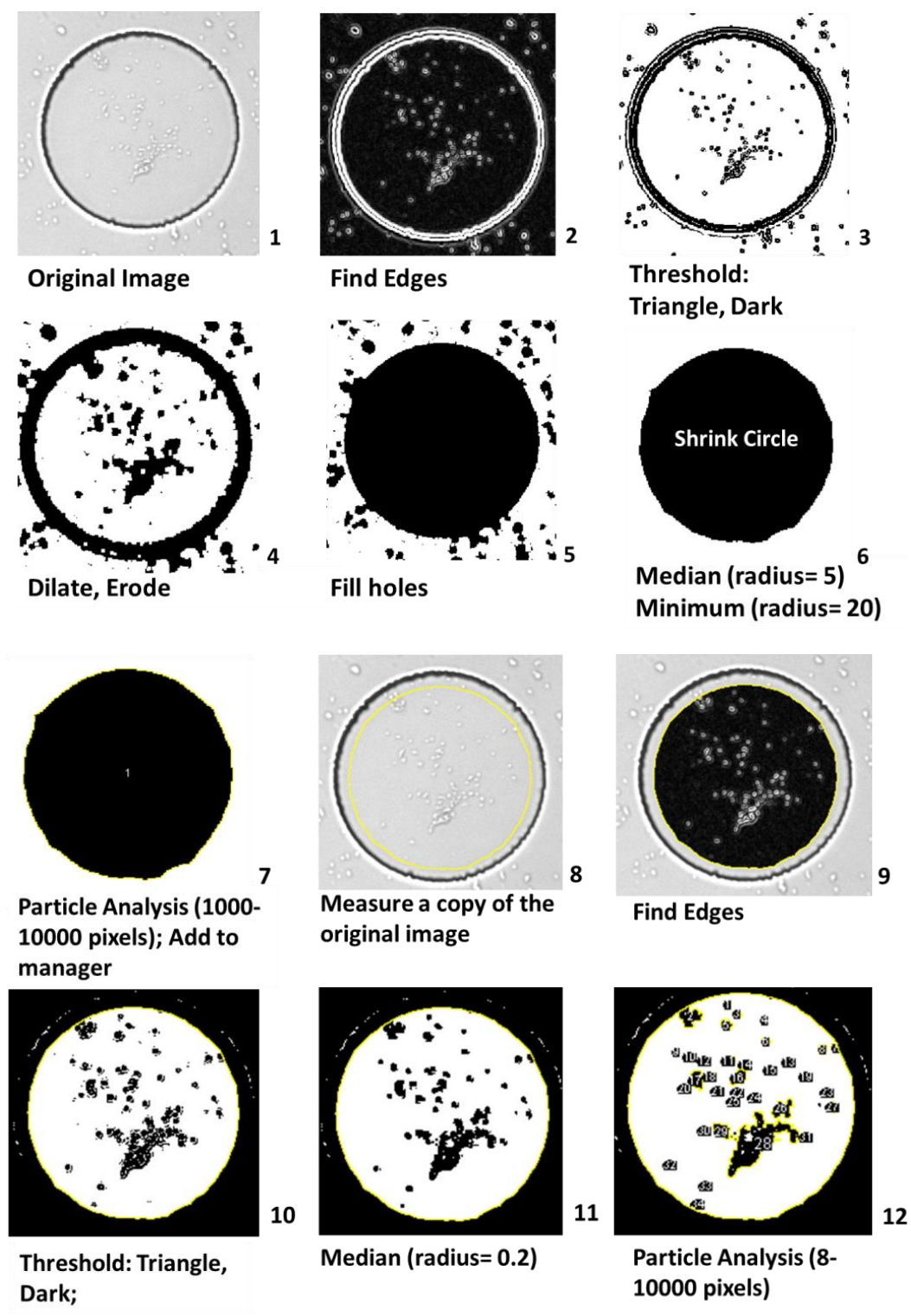


**Figure 3.1.1: Outline of the ImageJ image processing algorithm labeled with built-in functions.**

This algorithm did not include cells on the border of the microwell (“Exclude on edges”). Cells that attached to the SU-8 wall are not a fair assessment of the base material, and this algorithm pairs with a microwell platform designed to survey cell attachment to different materials.

Area coverage (%) is the recommended metric for reporting cell attachment. The cell count reported by the particle analysis function does not capture nucleation site as a collection of individual cells, but as one large particle. Area coverage captures all cells equally, and can be easily applied to measuring biofilm coverage, which might otherwise appear as one very large particle. Figure 3.1.2 presents a standard comparison of area coverage to the number of cells.

The microwell platform can be combined with image processing to yield a high-throughput method for quantifying early biofilm formation. A 20 mm by 20 mm substrate can easily house over a hundred microwells with 100  $\mu\text{m}$  diameter. This number is even greater with smaller well sizes. For instance, the Timm et al. silicon microwell platform housed thousands of microwells on a platform of roughly equal size (2017). This image processing algorithm quantifies biomass in the transparent microwell platform in a timely manner and is recommended for the survey of bacterial attachment to different substrate materials.

### **3.2 Quantify and Characterize Spatial Organization in Biofilms**

Many image processing algorithms are geared towards cell colony counts or quantifying fluorescence intensity, neither of which are designed to handle unique biofilm features (Clarke et al., 2010; Cai et al., 2011; Geissmann, 2013; Choudhry, 2016). Unique biofilm features and morphology are predominantly described by qualitative observations, and there is a need to extract quantitative information to explain intuitive trends viewed in microscopy images.

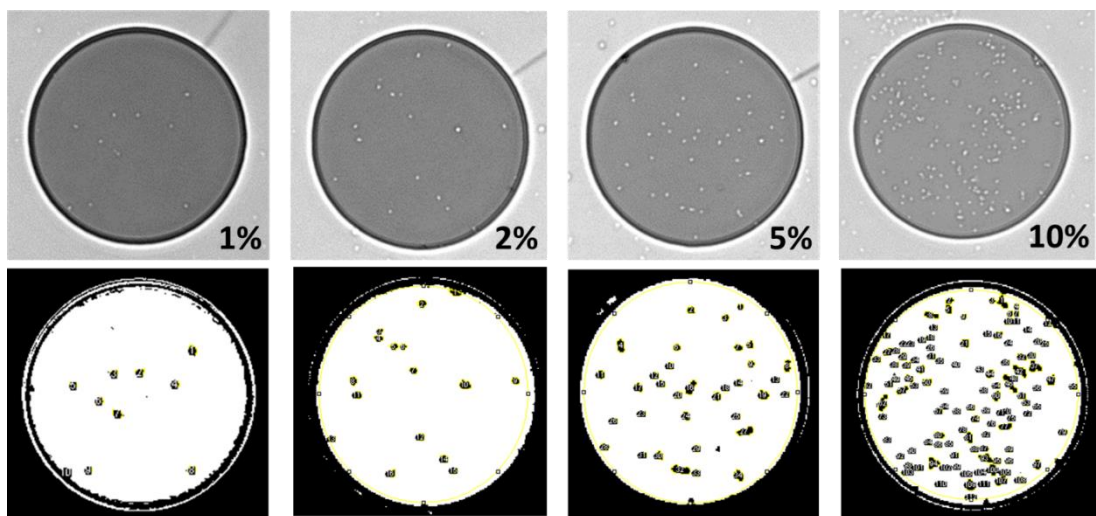


**Figure 3.1.2: Percent area coverage standards and particle count masks. Left to right: particle count 10, and 1.1% area coverage; particle count 16, and 2.0% area coverage; particle count 34, 4.8 % area coverage; particle count 112, 10.9% area coverage.**

A prime example is the honeycomb biofilm morphology of *Listeria monocytogenes*, observed under various experimental conditions and material substrates (e.g. polystyrene, steel) (Tresse et al., 2009; Kocot and Olszewska, 2017; Mosquera-Fernández et al., 2014; Mosquera-Fernández et al., 2016; Marsh, Luo, and Wang, 2015). *Pantoea* sp. YR343 also form honeycomb biofilm patterns on hydrophobic surfaces; this work enumerates the morphology of the *Pantoea* sp. YR343 biofilm with semi-automated ImageJ algorithms (Figure 3.2.1).

Binary images were created from fluorescence images of *Pantoea* sp. YR343 to leverage the particle analysis function for spatial characterization. To generate a binary image, the algorithm applied a background subtraction, followed by a threshold function (Huang or Default). The threshold function was selected to accommodate differences in the images. The binary image was saved in a separate folder and the images were manually adjusted, as needed, to generate a binary image representative of the original image. Adjustments included binary functions, various filters, and removal of background noise. The adjusted binary images were processed in a second algorithm to analyze the honeycomb morphology. The *Pantoea* sp. YR343 biofilm has continuous, interconnecting branches of cells, and the gaps of empty spaces give off a honeycomb appearance. To understand spatial distribution in the biofilm, the particle analysis function was applied to the empty space in between the cells. To accomplish this, the binary image was inverted so that the gaps became the objects of interest (black). This “gap analysis” gleaned information on gaps size, the number of gaps, and total gap area coverage.

This method processed hundreds of images as part of the effort to understand the unique *Pantoea* sp. YR343 biofilm propagation and morphology (Chapter 6). The pattern begins with a branch-like groupings of cells, arranged in a linear fashion. These cell “branches” intersect as time progresses and eventually form a honeycomb pattern (Figure 3.2.2).

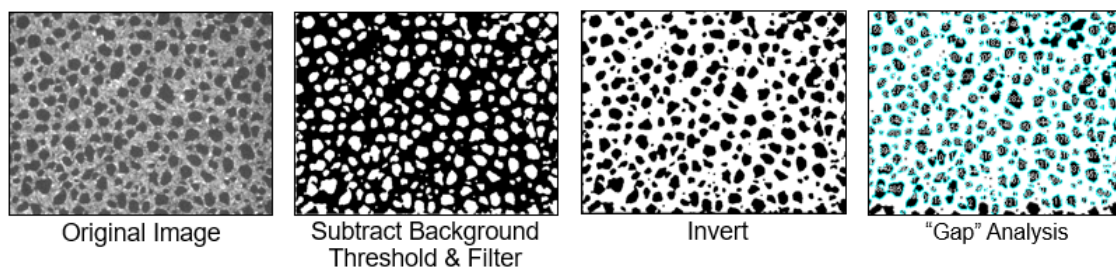


**Figure 3.2.1: Image processing and quantification of honeycomb biofilm pattern. Cells are grey in the original image and black after the threshold generates a binary image. The image is inverted, and the particle analysis function is applied to gaps in the image.**

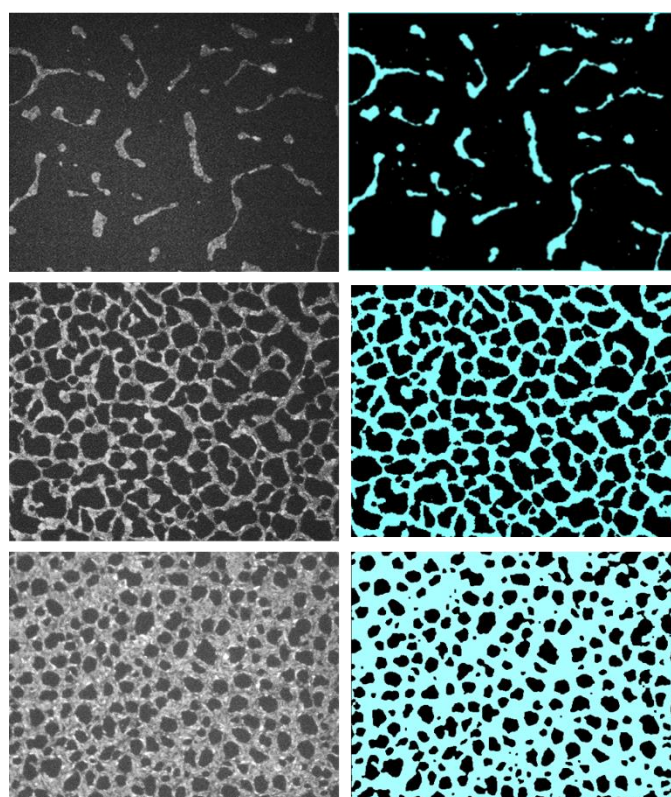


**Figure 3.2.2: Propagation of *Pantoea* sp. YR343 honeycomb pattern with fluorescence images (left) and threshold images (right) at various stages in the biofilm. Blue represents the cells ("branches") and black represents the empty space ("gaps").**

## **CHAPTER FOUR**

### **ADAPTABILITY AND VERSATILITY OF MICROWELL PLATFORMS IN THE STUDY OF MICROBIAL SYSTEMS**

Microwells can be thought of as microscopic test tubes, limiting bacterial experimentation to nanoliter volumes. These microwells can even trap cells with agar media and capture phenomenon that may be lost in macroscale experimentation (Marcy et al., 2007; Timm et al., 2016; Hansen et al., 2016). Matrices of microwells can facilitate hundreds of paralleled experimental parameters within a single platform, offering *en masse* experimental replicates, all the while retaining the resolution to image individual cells. This work demonstrates the adaptability and versatility of microwell platforms to provide spatial & physiochemical control, parallel experimentation, and microscopic & spectroscopic compatibility.

Nanofabrication techniques can craft (micro)wells with photolithography and soft lithography methods, and SU-8 negative photoresist epoxy and polydimethylsiloxane (PDMS) are ideal materials for these respective methods. Both materials are transparent and biocompatible (Jiang et al., 2010; Halsted et al., 2016; Friedlander et al., 2013; Kim et al., 2012). These well platforms can readily accommodate a variety of surfaces, enabling the study of physiochemical influences on biofilm propagation.

This work leverages the nanofabricated well platforms to study *G. sulfurreducens* biofilm. First, by examining cell attachment to different surfaces (i.e. glass coverslips, quartz, and gold thin films). Second, by elucidating the electrochemical behavior of *G. sulfurreducens* biofilm with cyclic voltammetry (CV) via electrochemical surface plasmon resonance (ESPR), demonstrating the ease at which the nanofabricated platforms can be combined with various spectroscopic techniques.

## 4.1 High-Throughput Approach to Monitoring Cell Attachment

There is a need to understand the factors which promote cell attachment. Existing methods for cell attachment studies include material coupons (e.g. steel, polystyrene, Teflon, etc.) and surface functionalization of transparent substrates (e.g. coverslips coated with metal oxides, thin-films metals, and self-assembled monolayers) (Mozes et al., 1987; van Schie and Fletcher, 1999; Busalmen & Sánchez, 2001; Gottenbos et al., 2002; Li and Logan, 2004; Jain et al., 2004; Reguera et al., 2005; Glass et al., 2011; Wang et al., 2011; Hochbaum and Aizenberg, 2010; Almaguer-Flores et al., 2015). Thin-film metals can be applied to transparent bases by sputter or electron beam evaporator deposition and adapted to bacterial biofilm studies. Metal films are optically transparent at 20 nm and subsequently compatible with brightfield microscopy. Thin-film metals can be easily adapted to the transparent microwell platform. When paired with image processing, these combined methods offer a high-throughput approach to early biofilm and cell attachment studies.

This work examines *G. sulfurreducens* attachment to substrate materials of glass, quartz, and thin-film gold, candidate materials for a microelectrode platform. *G. sulfurreducens* is anaerobic, and thus unsuitable for real-time imaging with fluorescence microscopy. Instead, brightfield microscopy imaged a (terminal) transparent microwell platforms at select time points. The data was processed with a custom image processing algorithm (section 3.1). This feasibility testing assessed the seeding time of *G. sulfurreducens* into microwell-microelectrode platforms for electrochemical experiments.

### Feasibility Testing and Application

Photolithography methods with SU-8 negative photoresist epoxy were applied to transparent substrates (e.g. glass coverslip, quartz, thin-film metals) to create a



microwell platform compatible with high-resolution brightfield microscopy imaging (section 2.2). A thin-film of gold was applied, prior to SU-8 photolithography, using electron-beam deposition.

The microwell platforms were seeded with 1 mL, optical density (OD<sub>600</sub>) 0.05 (at 600 nm) *G. sulfurreducens* in an anaerobic chamber. After a specified period of time (i.e. seeding period), the culture was pipetted up from the platform, removed from the anaerobic chamber, and rinsed with distilled (DI) water to remove loosely attached cells (Figure 4.1.1). The platform was dried with filtered compressed air to minimize drying artifacts. A brightfield microscope imaged the microwell platform to examine the remaining, attached cells within the microwell. A minimum of 50 wells were imaged on each platform to generate a data set with hundreds of well images (Figure 4.1.2, A). Each device was terminated after imaging.

Gold is a popular electrode material in microbial fuel cell (MFC) experiments (Reguera et al., 2007; Strycharz et al., 2011; Malvankar et al., 2011; Lovely, 2012; Snider et al., 2012). Unlike in MFC experiments, voltage potential was not applied to the gold substrate in this experimental setup. *G. sulfurreducens* attachment to glass surpassed gold at each time point. There was negligible attachment to quartz throughout the experiment (Figure 4.1.2, A). The variation in cell seeding is explicated in Figure 4.1.3 with distributions of surface coverage in the microwell platform for each time point. The distributions of these materials reinforce *G. sulfurreducens* preference attaching to glass. After just one hour, 50% of the wells exceeded 0.5% area coverage on glass, compared to gold where only 40% of wells exceeded 0.5% area coverage after 4 hours of seeding. Figure 4.1.3, C illustrates a distribution of the glass dataset with an area coverage between 0-10% as part of an effort to understand the variation in area coverage for the 2-hour and 4-hour dataset show in Figure 4.1.2, B.

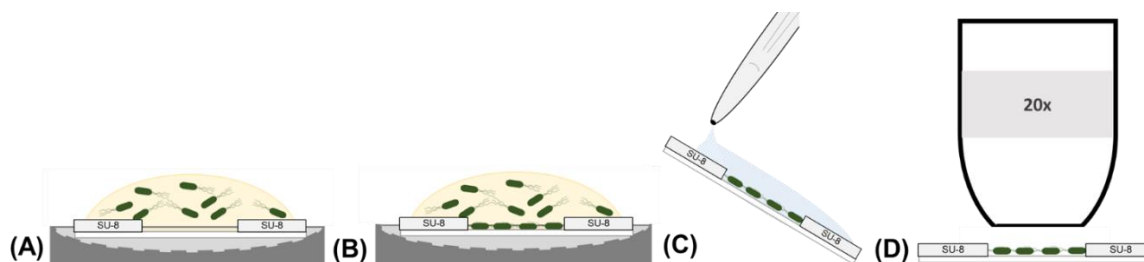


**Figure 4.1.1: Biofilm assay methods: substrate inoculated with 1 mL DCB-1 medium, 0.05 OD<sub>600</sub> *G. sulfurreducens*. (A) Cells attached to substrate (B) Substrate removed at designated time point and rinsed with 10 mL DI water, 2 mL IPA, and dried with pressurized air (0.2  $\mu$ m filter). (C) Imaged with brightfield microscope, 20x objective.**

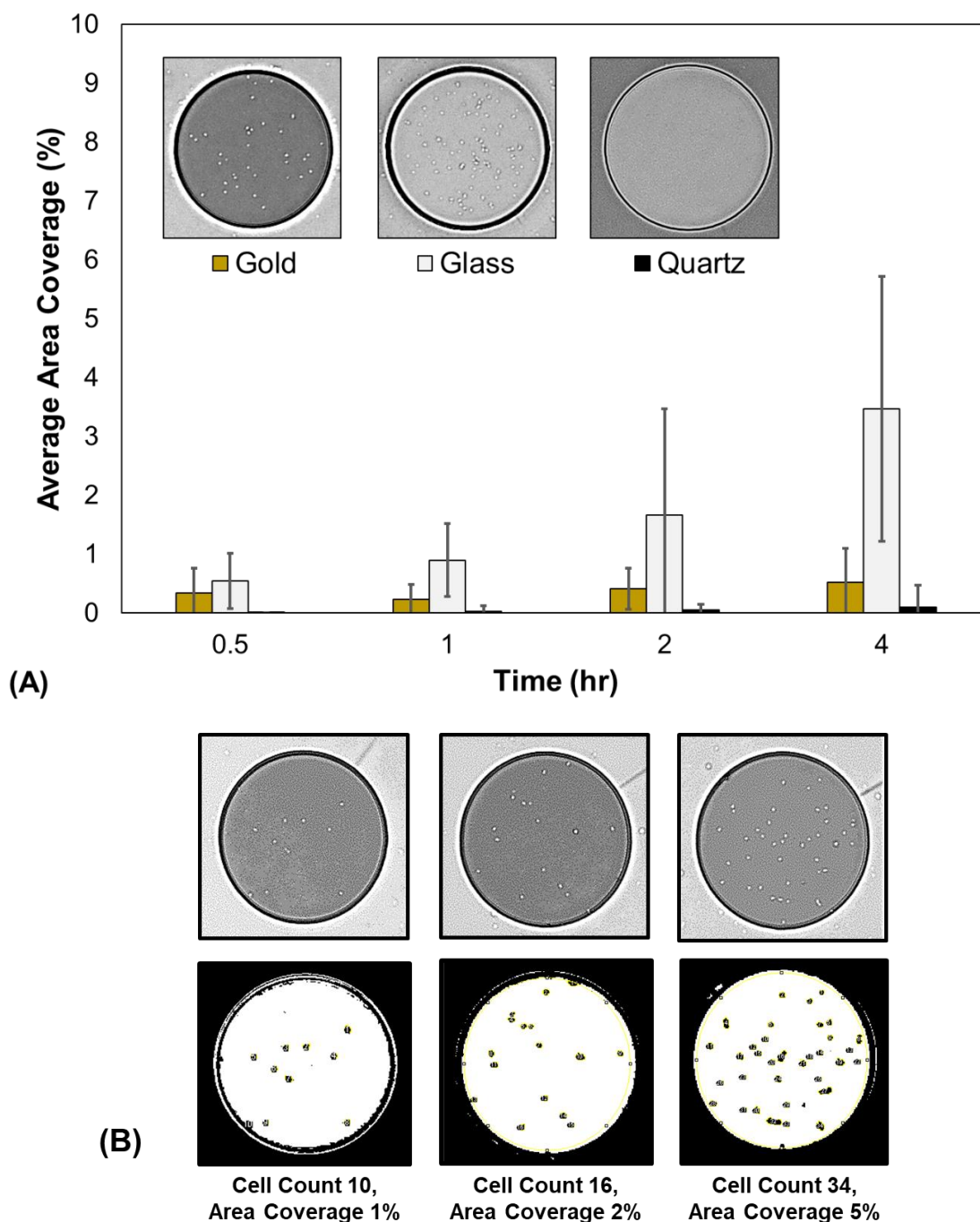


**Figure 4.1.2: *G. sulfurreducens* seeding in SU-8 microwell. (A) Average area coverage  $\pm$  standard deviation on gold, glass and quartz with representative images of *G. sulfurreducens* seeding at four hours. (B) Area coverage standards based on ImageJ particle analysis function.**

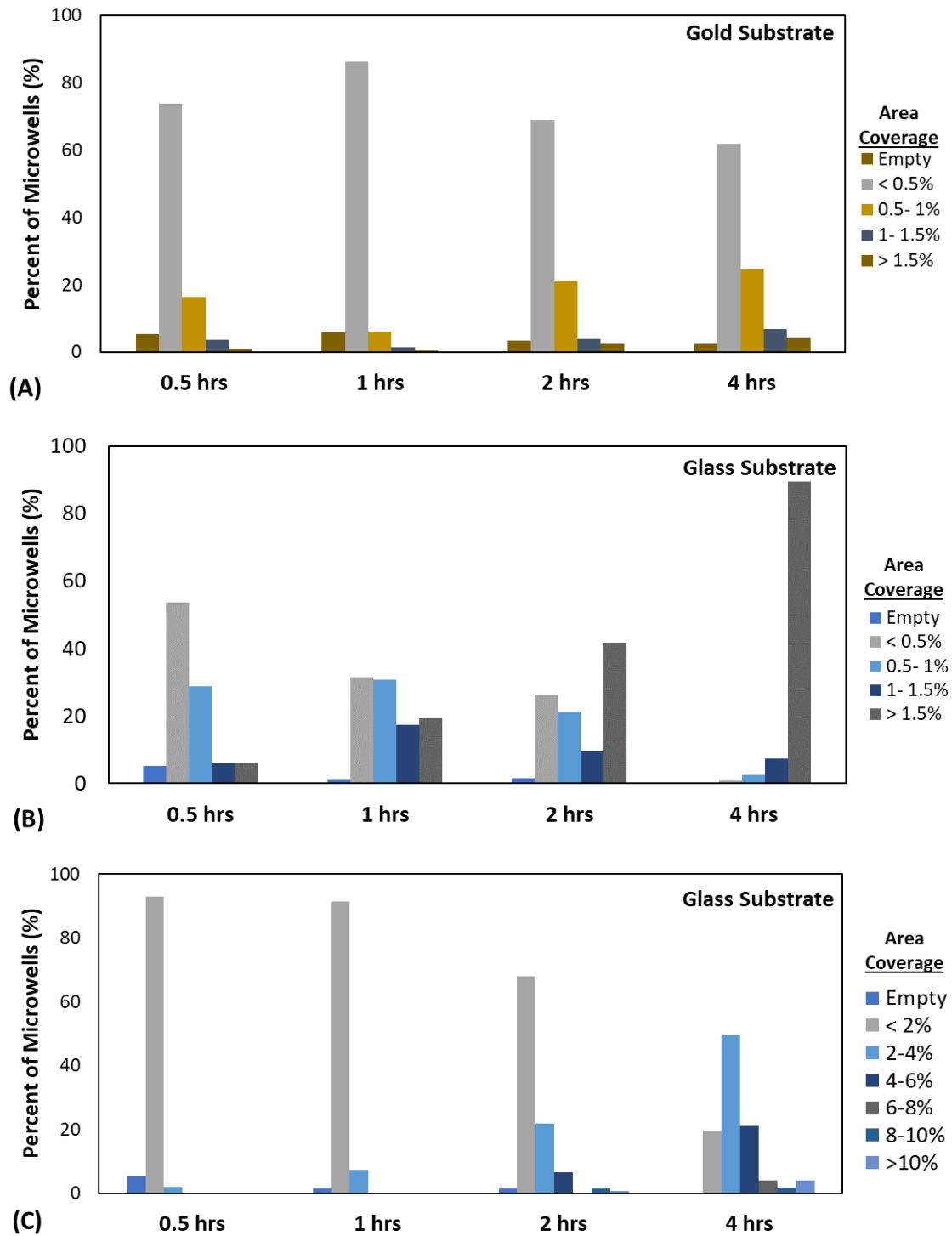


**Figure 4.1.3: Distribution of *G. sulfurreducens* seeding in microwell platform with material substrate. (A) Distribution of gold and (B) glass from 0-1.5% area coverage. (C) Distribution of glass from 0-10% area coverage.**

Differences in area coverage may be explained by physicochemical properties of the different material substrates. Surface energy can be inferred from contact angle measurements, with hydrophobic surfaces having low surface energy (Yilbas et al., 2018). Water contact angle measurements revealed the glass coverslip and the thin-film gold have similar hydrophilicities at 69° and 68° respectively (Automated Goniometer with DROPImage Advanced v2.5, Ramé-hart, Model 590, F4 Series). The absence of cell attachment to quartz may be explained by hydrophobicity, water contact angle of 54°, which is substantially less than gold and water. Differences between glass and gold may be due to the surface chemistry of the metal and non-metal substrates. These results dictate a at least 4 hours are needed to seed *G. sulfurreducens* in a gold microelectrode platform. The attachment preferences to glass may interfere with an electrochemical signal at the start of an electrochemical experiment for certain electrode designs (e.g. nanoelectrodes, interdigitated electrodes).

The image processing script extracted numerical data on cell size and position to assess whether the microwell structure biased cell attachment to the base material. The 4-hour gold dataset was selected for this analysis to characterize *G. sulfurreducens* seeding in a microwell-microelectrode platform. Figure 4.1.4, B reports spatial information on *G. sulfurreducens* attachment within the microwells.

Spatial distribution compared the location of attached cells across the microwell in reference to the center. The microwell was partitioned in 5 µm radial increments to create annulus regions resembling a dartboard (Figure 4.1.4, A). The image analysis measured the microwell regions in pixels but is reported in microns for simplicity. The annulus surface area increases with increased distance from the center, thus cell attachment was normalized by annulus area and reported as a percentage of cells attached to each region. The exterior annulus region (45- 50 µm) was excluded from this analysis due to specifications from the image processing algorithm (see section 3.1 for details).

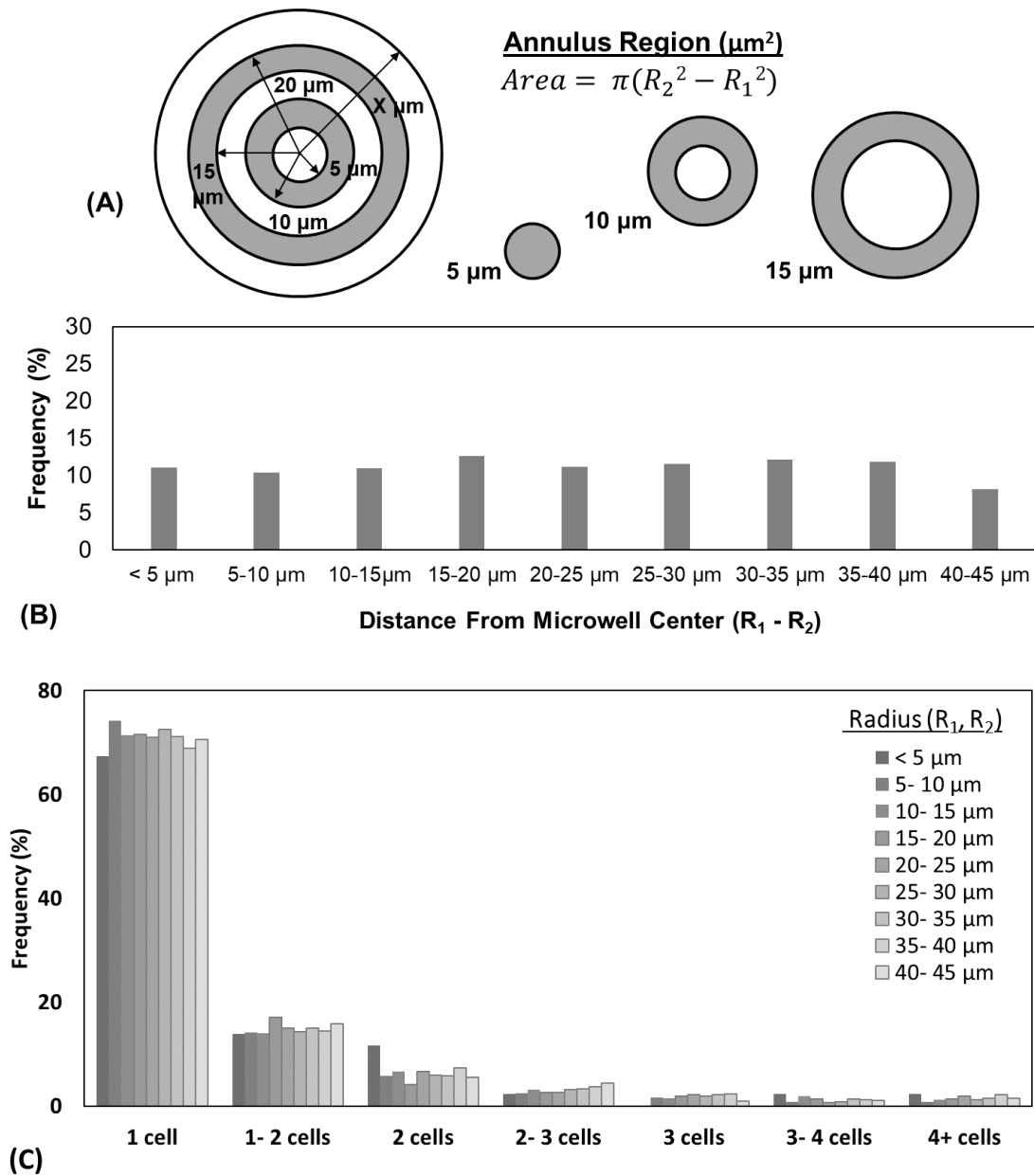


**Figure 4.1.4: Characterization of cell seeding within a microwell, gold substrate, 4 hours. (A) Diagram of annulus regions in microwell. (B) Spatial distribution of *G. sulfurreducens* area coverage in microwell. (C) Distribution of *G. sulfurreducens* seeding as a function of cell anchor size and location in the microwell.**

As time progresses, cells congregate and form nucleation sites, or cell anchors, the beginning of a biofilm. Figure 4.1.4, C incorporates size into the spatial data to determine if the microwell structure biased the location of emerging cell anchors (i.e. whether clumps of cells are biased in the center of the well). Figure 4.1.4, C presents the distribution with a rough estimate of cell number based on pixel range but is not an exact measure. After 4 hours, surface area coverage on gold is primarily single cell attachment to the substrate. Figure 4.1.4, C suggests the microwell structure does not bias cell attachment to the material substrate.

The design and characterization of this platform established a foundation for a new genera of biofilm studies. A parylene lift-off layer can be readily adapted to direct microwell seeding. This is a delicate process and not recommended for anaerobic experiments (the glovebox restricts dexterity). The parylene lift-off layer can stochastically assemble mixed bacterial communities (Timm et al., 2017). This is a promising approach to assess the influence of pioneer community members on initial cell attachment and varying substrate material. The platform can be capped with agar for time-lapse imaging, as was done with the silicon microwell platform in Timm et al. (2017). Confocal laser scanning microscopy can be incorporated to visualize three-dimensional attachment along the wall of a transparent microwell.

## **Materials and Methods**

### *Nanofabrication*

Gold thin films were deposited on quartz prior using an Electron Beam Evaporator (Thermionic VE-240). An adhesive layer was created with 5 nm of titanium, followed by 20 nm deposition of gold. SU-8 2005 (MicroChem Corp., Westborough, MA) was spun-cast onto the substrate at 2000 RPM for 90 seconds to achieve a thickness of  $5 \pm 0.5 \mu\text{m}$ . A soft bake was conducted at 95 °C, and was performed for 2 min prior to exposure at 110 mJ/cm<sup>2</sup> with a SUSS & Micro Tec (MA6/BA6) Mask Contact Aligner. After exposure, the substrate was placed on 95°C hot plate for 2.5 min, followed by development with Microchem SU-8 Developer

(Westborough, MA) using the spray-puddle method for 30 s. The substrate was rinsed with additional SU-8 Developer, then rinsed again with isopropyl alcohol (IPA), and dried with filtered, pressurized nitrogen.

### *Bacterial Culture*

A strain of *G. sulfurreducens* was received from the Microbial Electrochemistry group at the Naval Research Lab (Washington D.C). The cells were inoculated in DCB-1 medium and grown to stationary phase under anaerobic conditions (Löffler, Sanford & Tiedje, 1996; Helmus et al. 2012). The DCB-1 medium contained 20 mmol acetate and 40 mmol fumarate. The stationary liquid culture was inoculated at 1:100 dilution in new medium and grown for two days. The culture was then inoculated again at a 1:10 dilution and grown for two more days.

### *Biofilm Formation Assay*

The devices were stored in plastic containers, cleaned with a five-minute oxygen plasma, and loaded into the anaerobic chamber 2 days prior to the experiment to degas oxygen from the materials. After two days of growth, the culture was measured and diluted to 0.05 OD<sub>600</sub> for the cell attachment study. The microwell platforms were arranged in a horizontal position and 1 mL of culture was pipetted on to each device. At the end of the designated time, the culture was pipetted up from the platform and removed from the anaerobic chamber and rinsed with 1 mL of DI water via pipette for ten iterations. The device was then rinsed twice with 1 mL of isopropanol (IPA) and dried with filtered pressurized nitrogen to minimize drying artifacts. A summary of these methods can be found in Figure 4.1.1.

### *Microscopy*

An Olympus IX51 microscope (Shinjuku, Tokyo) was used to collect optical image data. Brightfield microscope images were taken of the microwell at random with the 20x objective, with one microwell per image. A minimum 50 microwell images were captured per device, demonstrating *en masse* experimentation.



### *Image Processing*

An image processing algorithm was scripted for the microwell device using ImageJ to process thousands of microwell images from the attachment studies. In sum, the algorithm applies an edge detection to emphasize the foreground objects, then applies a threshold to generate a region of interest (ROI) mask of the microwell. On a duplicate image, edge detection, threshold, filter, and particle analysis functions are applied within the microwell ROI to quantify the attached cells (Figure 3.1.1).

## **4.2 Parallel Interrogation of *G. sulfurreducens* Biofilms via Electrochemical Surface Plasmon Resonance**

*This work was part a collaboration with The Naval Research Lab (NRL) and The Center for Nanophase Material Sciences (CNMS) at Oak Ridge National Laboratory (ORNL). Fabrication of the platform took place at the Nanofabrication Research Laboratory, ORNL as part of the CNMS User Program. The Microbial Electrochemistry group, NRL performed electrochemical Surface plasmon resonance testing. This collaboration included participation in the Navel Research Enterprise Internship Program (summer, 2017), and an internship with the Microbial Electrochemistry group. Funding for the internship was provided by the American Society for Engineering Education.*

Electrochemical surface plasmon resonance (ESPR) is a promising approach to investigating electron transfer in electroactive biofilms (Golden et al., 2018). This instrumentation is highly sensitive to changes in a metal surface, capable of detecting electron transfer from a bacterial cytochrome to the gold electrode. Specifically, the instrument detects changes in the redox state at the electrode surface from changes in the refractive index, reported by a charge-coupled device (CCD) detector as changes in pixel intensity (Golden et al., 2018). With the unique

features of this spectroscopic technique, Golden et al. found evidence of electron storage in *G. sulfurreducens* c-type cytochromes which took up to 12 hours to re-oxidize in ESPR electrochemical experiments.

The ESPR specialty slide can be augmented with nanofabrication techniques to confine biofilms and enable parallel experimentation. Such adaption magnifies the data collection and broadens ESPR experimentation capabilities. This section demonstrates the utility and compatibility of the ESPR (micro)well platform in the study of *G. sulfurreducens* biofilms.

### **Feasibility Testing and Application**

ESPR platforms were fabricated at Oak Ridge National Laboratory (ORNL) and were brought (or shipped) to the Naval Research Laboratory (NRL) for testing. Three different types of ESPR platforms were crafted for the study of electroactive biofilms: 1) ESPR microwell platform 2) ESPR PDMS well platform 3) ESPR Multielectrode well platform. Fabrication of these ESPR platforms can be found in “Electrochemical Surface Plasmon Resonance Platform” (section 2.3).

Experimental setup varied slightly with the different ESPR platforms as the ESPR PDMS well platforms were designed for deterministic seeding. The ESPR PDMS well platform and the ESPR multielectrode well platform were seeded with a pipette in an anaerobic chamber, then transferred to the ESPR system. The ESPR chamber was filled with medium to provide an electrolytic solution for a common reference electrode and a common counter electrode. The ESPR microwell platform was placed directly into the ESPR chamber, filled with medium, and inoculated with 10% *G. sulfurreducens*, total volume. A detailed description of the SPR system and setup can be found in Golden et al., 2015.

The ESPR platforms can measure electroactive biofilm growth by current output when a voltage is applied to the system, a process known as chronoamperometry.

As the biofilm grows, there is an increase in the number of *G. sulfurreducens* cells, which subsequently increases the number of metabolic processes. The applied voltage drives the cells to transfer electrons to the working electrode (SPR specialty slide). Electron transfer is detected by a charge-coupled device (CCD) camera (as changes in pixel intensity), which captures spatiotemporal changes with sequential images. Current is defined as the flow of electrons, therefore biofilm growth results in an increase in current under an applied voltage.

Figure 4.2.1 demonstrates the ability to monitor biofilm growth in the PDMS well platform with the ESPR system as pixel intensity increased with biofilm growth. Biomass has a greater refractive index than water, thus the seeded wells appears white in the image. Biofilm growth was only detected in the wells seeded with *G. sulfurreducens* culture at the onset which demonstrates the ability to deterministically seed cultures in the PDMS well platform (Figure 4.2.1).

Cyclic Voltammetry (CV) is an essential method for understanding electrochemical phenomena and has been adapted to the study of electroactive biofilms (Beyenal and Babauta, 2015). CV applies a voltage potential and changes the voltage at a fixed rate (i.e. scan rate). The potentials are applied with respect to a known reference potential (e.g. Ag/AgCl) included in the system. This interrogates the potential difference for the redox reactions in the system, searching for polarization potentials which will yield current flow via electron transfer in the redox reactions (Beyenal and Babauta, 2015). This relationship between the applied potential and current is referred to as a voltammogram, and electrochemical behavior can be inferred from the shape of the voltammogram (Beyenal and Babauta, 2015).

Cyclic voltammetry (CV) experiments were performed with the potentiostat (scan rate 1 mV/s). The CV scans were performed during stationary phase in turnover conditions (i.e. the cells were metabolizing acetate). Current response in the *G. sulfurreducens* biofilm was monitored by the change in pixel intensity. CV scans

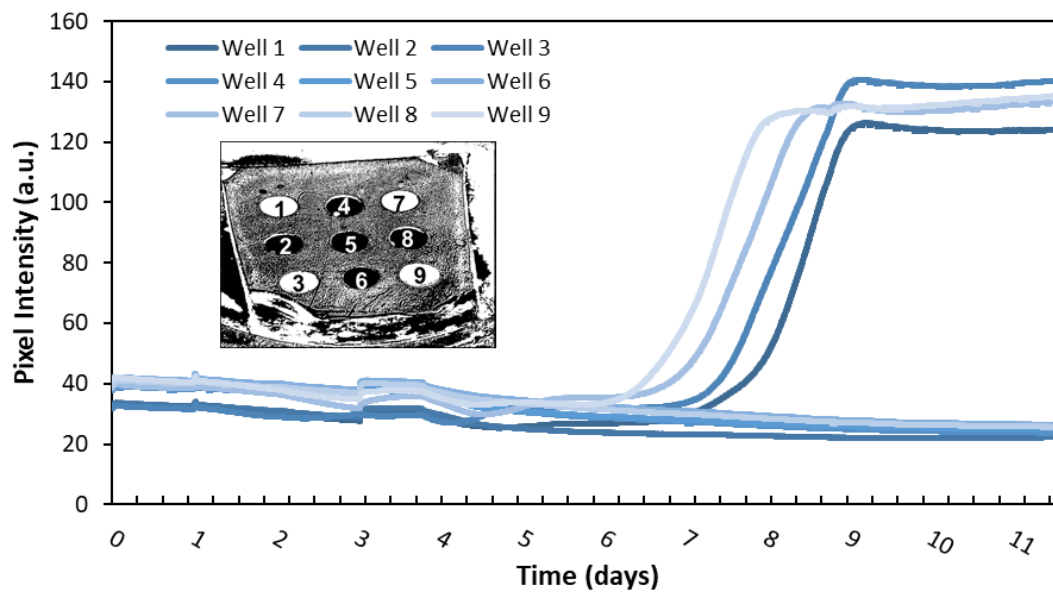


**Figure 4.2.1: Change in SPR pixel intensity of *G. sulfurreducens* cultures in PDMS wells 1, 7, 3, 9 (insert).**

on the *G. sulfurreducens* electroactive biofilm were successfully performed on ESPR microwell platform and the ESPR PDMS well platform (Figure 4.2.2). Each platform measured a unique electrochemical signal in the well. The CV scan confirms that the ESPR PDMS well platform can simultaneously measure unique electroactive biofilms in the PDMS wells. The 49 voltammograms of the ESPR microwell platform were spread over 115 pixels, so the voltammograms were adjusted by a baseline pixel intensity to compare the voltammogram shapes more easily (Figure 4.2.2, A). Differences in pixel intensity amplitude may be due to various gradients in the bioreactor (e.g. temperature, oxygen, etc.), which subsequently affects *G. sulfurreducens* growth and redox reactions. The variation in the system demonstrates the ability of the ESPR microwell platform to capture unique voltammograms.

Future experimentation could include an agitator to ensure proper mixing. The ESPR PDMS well platform only measures voltammograms in the wells seeded with *G. sulfurreducens*, further demonstrating the ability of the platform to assess unique electroactive biofilms (Figure 4.2.2, B). The ESPR PDMS well platform voltammograms are consistent with the results in Golden et al. (2018).

One application for the ESPR microwell platform is high-throughput screening of marine sediment for electrigenes. Marine sediment is home to numerous strains of anaerobic, metal-reducing bacteria, and some of these bacteria are capable of extracellular electron transport. The microwell structure partitions the ESPR slide and can be used to identify electrigenes in the marine sediment (bacteria which demonstrate electrochemical behavior). The microwells provide a guide for cell extraction to enable culturing and identification of the electrigenes.

The PDMS well platform is a promising experimental approach for simultaneously comparing voltammograms of *G. sulfurreducens* mutants. Mass experimentation of *G. sulfurreducens* mutants with various c-type cytochrome deletions and type

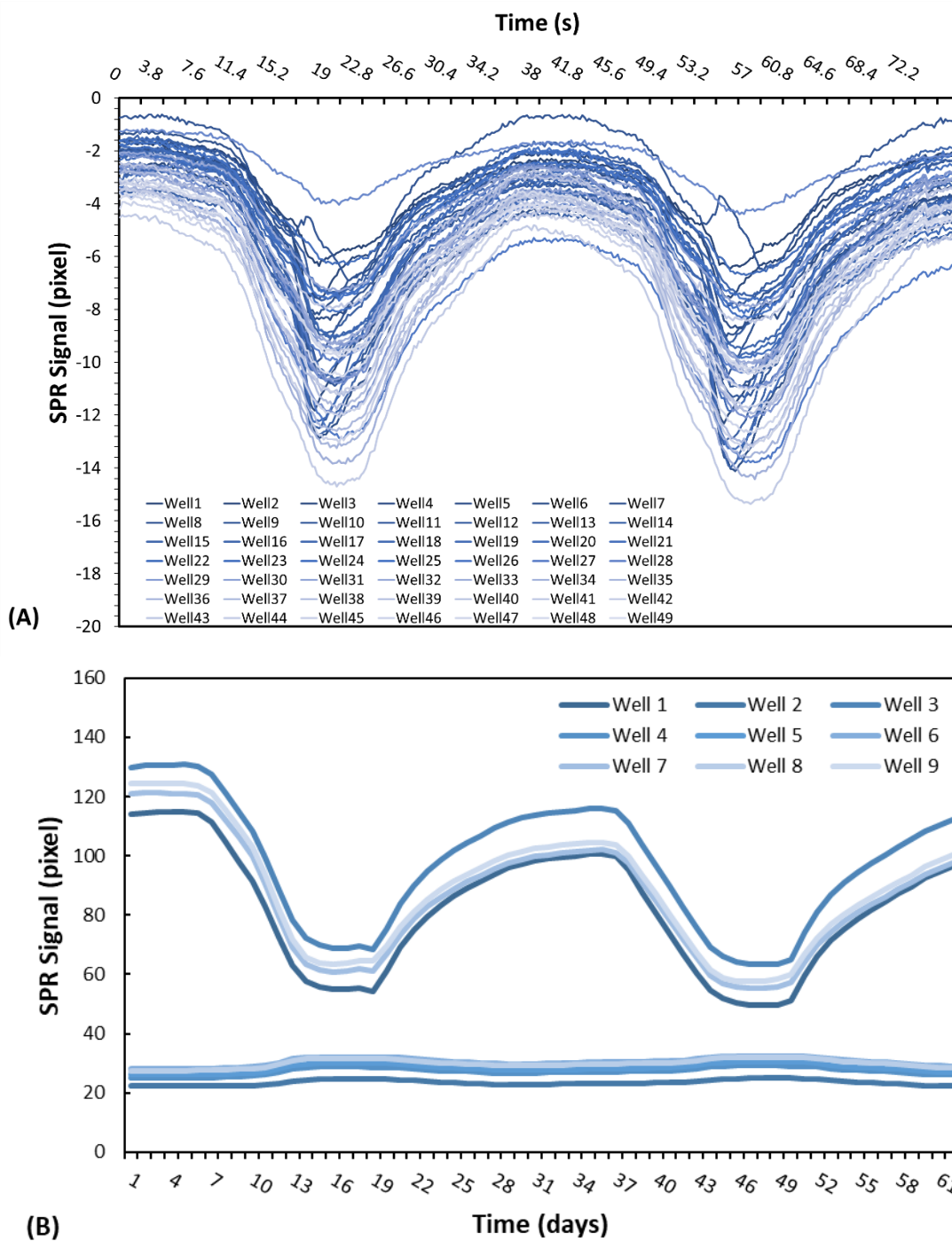


**Figure 4.2.2: Cyclic voltammetry *G. sulfurreducens* activity at the surface of the SPR slide in turnover, stationary conditions: 2 scans with scan rate of 1 mV/s, applied potential of 0.20 V to -0.75 V vs. Ag/AgCl. (A) ESPR microwell platform, 49 simultaneous measurement; (B) ESPR PDMS well platform with deterministic seeding in 4 PDMS wells.**

IV pilin would yield tremendous insight to electron transfer in the *G. sulfurreducens* biofilm. Such experiments would complement electrochemical experiments with interdigitated electrodes in traditional electrochemical bioreactors as ESPR uniquely measures electron transfer at the electrode surface.

## Materials and Methods

*A version of this work was originally published by J. Golden, M. D., Yates, M. Halsted, and L., Tender:*

*Golden, J., Yates, M. D., Halsted, M. and Tender, L. Application of electrochemical surface plasmon resonance (ESPR) to the study of electroactive microbial biofilms. (2018). Physical Chemistry Chemical Physics. 20, 25648-25656. Doi: 10.1039/C8CP03898H*

### *G. sulfurreducens culture*

This work followed the culture procedures used in Yates et al. (2017; 2016). *G. sulfurreducens* culture was grown to 0.5 OD<sub>600</sub> in sterile, anaerobic NB medium ((g/L: 0.38 KCl, 0.2 NH<sub>4</sub>Cl, 0.069 NaH<sub>2</sub>PO<sub>4</sub>·H<sub>2</sub>O, 0.04 CaCl<sub>2</sub>·2H<sub>2</sub>O, 0.2 MgSO<sub>4</sub>·7H<sub>2</sub>O, 2 NaHCO<sub>3</sub>; 10 ml/L trace minerals; final pH 6.8) containing acetate (20 mM) and fumarate (40 mM). To achieve this, the culture was incubated for two days at 30°C, until the culture reached 0.5 OD<sub>600</sub>. The 30 mL chamber was filled with NB medium, 10 mM acetate but no fumarate as the potentiostat served as the terminal electron acceptor during turnover conditions. The ESPR microwell platform was placed in the SPR chamber and inoculated with *G. sulfurreducens* culture, 10% total volume. The ESPR well platforms were seeded with a pipette in the anaerobic chamber with 10 µL, 0.5 OD<sub>600</sub>.

### *Fabrication of ESPR platform*

All platforms used a standard SPR substrate (GWC Technologies), SF10 glass slides with 7 nm thick titanium adhesive layer and 38 nm gold layer. The gold

multielectrode platform was deposited in-house on SF10 glass substrate with Thermionic VE-240 electron beam evaporator. Nanofabrication specifics are described in “Electrochemical Surface Plasmon Resonance Platform” (section 3.3). Silver epoxy bound the electrical connections to the slide edge and was cured at 80 °C for 2 hours. A five-minute oxygen plasma sterilized the platform prior to experimentation.

### *Instrumentation*

An SPRImager Horizon, GWC Technologies: Kretschmann configuration and CCD detector, was used for SPRi measurements ( $800 \pm 6$  nm manually adjustable fixed angle). A custom chamber (30mL) contained *G. sulfurreducens* culture. The base of the chamber was the SPR substrate sealed with a 2 cm diameter nitrile rubber O-ring. The electrical connection was outside the chamber and the gold film faced up. A diagram of this experimental set-up can be found in Golden et al. (2015). A 1470E, AMETEK potentiostat was used to perform cyclic voltammetry and monitor changes in electrochemical current output. The SPR angle was set between 75-185-pixel intensity (8 bits, maximum range 0-255).

### *Experimental Set-up*

The SPR slide was sealed and index matching fluid (Cargille Master Calibration Liquid, no. 19268,  $n=1.6304$ ) mounted the SPRi prism to the bottom of the ESPR substrate (i.e. to the side without gold). To maintain anaerobic conditions, the chamber was sealed, with opening for a reference electrode (Ag/AgCl, 3 MKCL, Bioanalytical Systems), a counter reference electrode (1/4"- diameter graphite rod), and a sparge cannula flowed a carbon dioxide-nitrogen mixture to maintain positive pressure (20 CO<sub>2</sub>:80 N<sub>2</sub>). The entire system was held in a 30°C incubator. *G. sulfurreducens* was grown at an applied voltage of 0.30 V vs. Ag/AgCl.



## **CHAPTER FIVE**

### **CELL ATTACHMENT STUDIES USING SUBSTRATE FUNCTIONALIZATION AND IMAGE PROCESSING**

*A version of this work is being prepared for publication.*

The rhizosphere is the region of soil influenced by plant roots, home to countless microbial communities (Singh et al., 2004; Lugtenberg and Kamilova, 2009; Brown et al., 2012; Berendsen, Pieterse, and Bakker, 2012; Pandit et al., 2020). The biological systems in the rhizosphere are integral in cycling some of the earth's most precious elements and minerals (e.g. nitrogen, carbon, calcium, phosphorus, sulfur, iron, water, silica etc.) (Drigo et al., 2012; Pii et al., 2016; Pandit et al., 2020). Understanding the incredibly complex rhizosphere ecosystem is hindered by the fact these systems cannot be visualized directly in the soil. Current experimental efforts include greenhouse and field experiments and laboratory bench-top experiments on agar (Singh et al., 2004). Conventional approaches are limited in their ability to perform bacterial cultures in the rhizosphere with access to temporal and spatial data on cell behavior; this can be addressed with novel experimental platforms (Massalha et al., 2017; Aufrecht et al., 2017; Aufrecht et al., 2018). Nanofabrication techniques offer exquisite control of surface properties across subcellular, cellular and community scales (Wang et al., 2011; Hol and Dekker, 2014). When paired with appropriate microscopy and image processing, these platforms can facilitate visualization and quantitative descriptions of these dynamic biological processes.

Bacterial communities subsist in biofilms, which can form on abiotic and biotic surfaces alike, such as soil particles and plant roots. Physical and chemical cues have a profound effect on biofilm formation, insight into these governing forces can be gained from fine control of surface properties (e.g. charge, hydrophobicity, roughness, topography, etc.) (Mozes et al., 1987; Costerton et al., 1999;

Gottenbos et al., 2002; Garrett, Bhakoo, and Zhang, 2008; Glass et al., 2011; Aizenberg et al., 2011; Epstein et al., 2011; Harimawan et al., 2011; Bendaoud et al., 2011; Friedlander et al., 2013; Tuson and Weibel, 2013; Crawford et al., 2012; Song and Ren, 2015). This work contributes to the study of the plant-microbe interface with an experimental approach to modify surface chemistry and examine the impact on cell attachment and biofilm formation. These methods can be adapted to the study of cell-surface interactions in numerous bacterial systems.

## **5.1 The Effect of Hydrophobicity on *Pantoea* sp. YR343 Cell Attachment and Biofilm Formation**

Thiol and silane chemistries can be used to modify surfaces, coating them with molecules with different functional groups for biofilm studies (Tan and Craighead, 2010; Privett et al., 2011; Glass et al., 2011; Wang et al., 2013; Tuson and Weibel, 2013; Friedlander et al., 2015; Maroni et al., 2015; Galbiati, 2016). Wang et al. utilized a hydrocarbon silane to survey attachment of *Staphylococcus epidermidis*, *Pseudomonas aeruginosa*, *Pseudomonas putida*, and *Escherichia coli* by performing cell counts from a video recording (2013). Another study utilized thiol self-assembled monolayers to evaluate the role of hydrophobicity on flagella adhesion, and the platform played a key role in identifying flagella as an integral component in *Escherichia coli* attachment to hydrophobic surfaces (Friedlander et al., 2015). Flagella adhesion was quantified with quartz crystal microbalance and dissipation (QCM-D), which leverages the extreme resonance sensitivity of a quartz crystal to quantify absorbed mass by change in resonance frequency (Friedlander et al., 2015). While this is a suitable approach to quantify biomass, these methods do not describe biofilm morphology.

This work examines *Pantoea* sp. YR343 attachment to hydrophilic and hydrophobic substrates, under static conditions, by use of functionalized silanes.

The *Pantoea* strain was engineered to express green fluorescent protein (GFP), enabling fluorescent microscopy for quantifying cell attachment and surface coverage. A custom image processing script quantified cell area coverage and enumerated *Pantoea* morphology.

## Results and Discussion

Silicon dioxide coated substrates were modified to examine the impact on cell attachment using the following chemistries: fluorinated chain, a hydrocarbon chain, an ester and an amine group. These substrates were characterized by hydrophobicity, as indicated by water contact angle measurement in Table 5.1.1. Materials with a contact angle greater than 90° are considered hydrophobic.

*Pantoea* sp. YR343 attachment to functionalized substrates were tested under static conditions. Substrates were submerged in 3 mL of R2A culture medium inoculated with *Pantoea* sp. YR343-GFP, at an optical density of 0.1 (600 nm). Substrates were removed from the culture at selected time points and rinsed with 10 mL distilled water to remove loosely attached cells. Care was taken to apply the water near the edge of the substrate and flow water across the sample. The substrate was dried with pressurized air to minimize any drying artifacts and subsequently imaged using a fluorescence microscope (Figure 5.1.1). Fluorescence images of the early biofilm were collected from multiple positions across each sample to capture representative cell behavior. An ImageJ script applied a built-in threshold function, Huang or Default, to generate a binary image (Figure 3.2.1). The binary image produced from each threshold function was evaluated, selected, and manually adjusted to most accurately reflect surface area coverage, i.e. cell attachment (Choudhry, 2016). A binary function inverted the image to facilitate counting and sizing of the gaps present in the honeycomb morphology (a full description of these methods can be found in section 3.2).

**Table 5.1.1: Summary of silane acronyms and water contact angle measurements.**

	PFOTS	OTS	MTMS	APTMS
<b>Chemical Name</b>	Trichloro (1H, 1H, 2H, 2H-perfluorooctyl) silane	n-octadecyl (trimethoxy) silane	Methoxytriethyl eneoxypropyl-trimethoxy silane	3-aminopropyl trimethoxy silane
<b>Surface Property</b>	Hydrophobic	Hydrophobic	Hydrophilic	Hydrophilic
<b>Contact Angle</b>	104°	93°	45°	53°

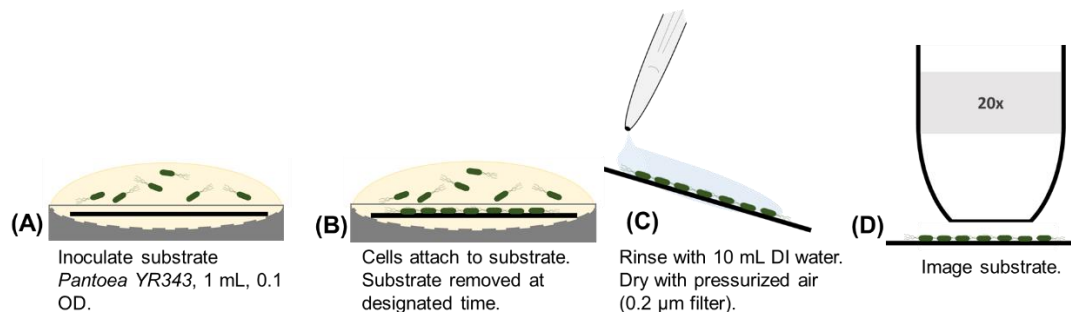


**Figure 5.1.1: Biofilm assay methods for functionalized silane platform. (A)** Substrates were submerged in 3 mL of R2A growth medium inoculated with *Pantoea* sp. YR343-GFP at an optical density (OD<sub>600</sub>) reading of 0.1. **(B)** Biofilm formation occurs for a set incubation period for each time point. **(C)** Substrates were removed at the designated time and rinsed with 10 mL of DI water, and dried with pressurized air (0.2 µm filter). **(D)** Imaging was carried out with a with 20x objective.

Figure 5.1.2 summarizes the effect of hydrophobicity on cell attachment. *Pantoea* sp. YR343 covered over 70% of the hydrophobic, silane-treated surfaces (PFOTS and OTS) after twenty hours (Figure 5.1.2). There was negligible attachment to the hydrophilic silane-treated surfaces (APTMS and MTMS) and control surfaces of glass, silicon, and quartz (not shown in Figure 5.1.2). These results are consistent with the literature, as bacteria have been shown to be negatively charged and favor attachment to hydrophobic, neutral surfaces (Donlan, 2002; Mai and Corner, 2007; Song, Koo and Ren, 2015; Berne et al., 2018).

## **5.2 Enumeration of *Pantoea* sp. YR343 Biofilm Propagation and Morphology**

Honeycomb biofilm morphology (also referred to as web-like, net-like, networks, and branching morphology) is not unique to *Pantoea* sp. YR343, and has been previously observed in the literature, under a variety of conditions, with different species of bacteria (Donlan et al., 2002; Marsh, Luo and Wang, 2003; Takhistov and George, 2005; Bridier et al., 2010; Serra et al., 2013; Mosquera-Fernández, 2014; Guilbaud et al., 2015). This morphology is unique to gram-negative bacteria. Numerous studies examine honeycomb biofilms for *Listeria monocytogenes*, a pathogenic gram-positive bacteria from the food processing industry (Chavant et al., 2002; Mosquera-Fernández, 2014; Guilbaud et al., 2015). Image processing can extract quantitative information from these images to explain intuitive trends with increased statistical rigor (Yang et al., 2001; Verma et al., 2012; Choudhry, 2016). This work utilizes a semi-automated ImageJ script, previously described in Section 3.2, to quantify the evolution of the *Pantoea* sp. YR343 biofilm morphology based on the number and size of gaps observed in the honeycomb pattern.

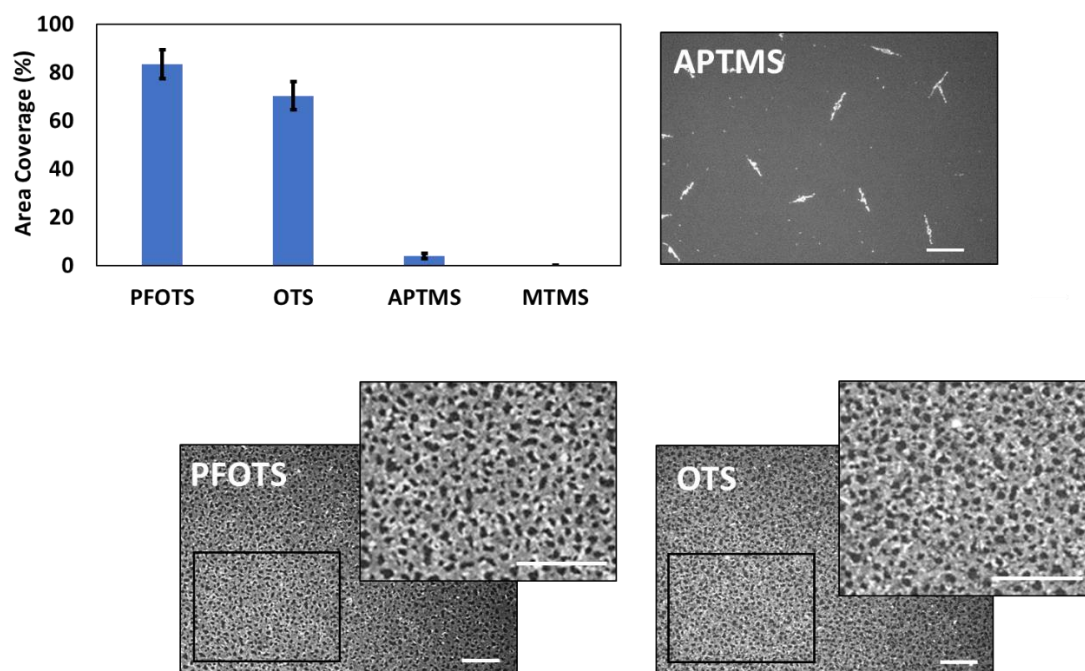


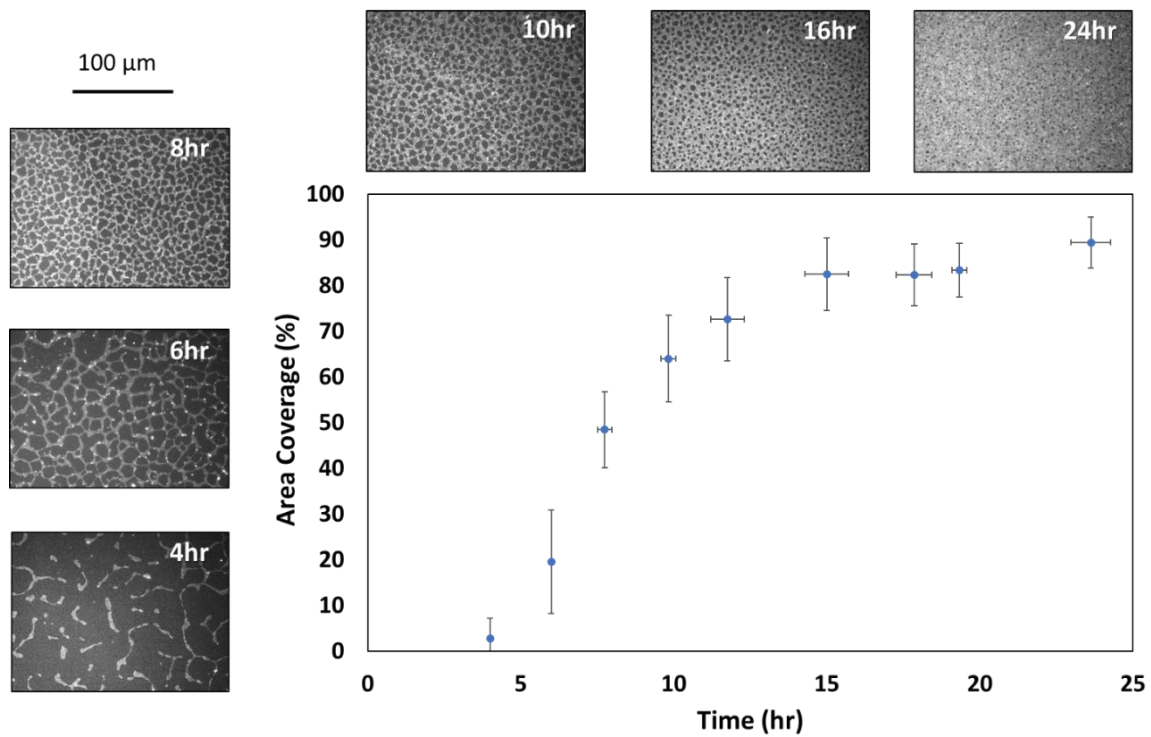
**Figure 5.1.2: *Pantoea* sp. YR343 area coverage on hydrophobic and hydrophilic surfaces after 20 hours: Trichloro(1H,1H,2H,2H-perfluorooctyl) silane (PFOTS), n-octadecyl (trimethoxy) silane (OTS), 3-aminopropyl trimethoxy silane (APTMS), Methoxytriethylenoxypropyl- trimethoxy silane (MTMS); scale bar 25  $\mu$ m.**

## Results and Discussion

The *Pantoea* sp. YR343 biofilm morphology could not be computed directly because of the interconnected honeycomb pattern. The ImageJ particle analysis function identified the (black) gaps in the inverted image as the object of interest. This “gap analysis” quantified the gap size, number of gaps, and surface area coverage (%). Subtraction of the gap area coverage from 100 yields the percentage of surface area covered by the cells (a full description of these methods can be found in section 3.2). Figure 5.2.1 describes *Pantoea* sp. YR343 attachment to PFOTS giving percent average area coverage for each time point. Representative images to convey the evolution of the honeycomb biofilm morphology.

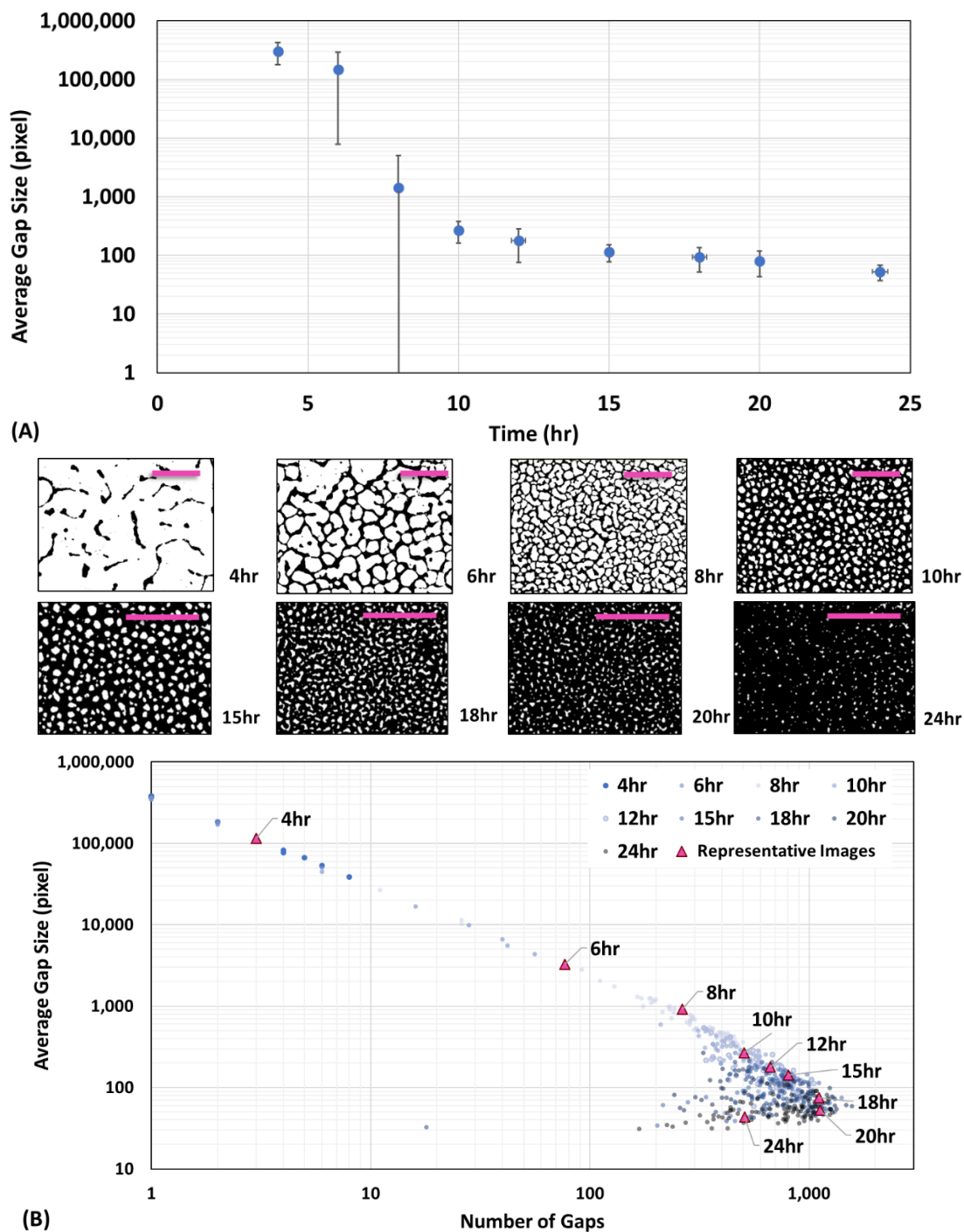
*Pantoea* sp. YR343 biofilm begins with linear branches of cells which extend in length and intersect with other branches to weave a net-like or “honeycomb” appearance. The honeycomb gaps are segmented with branches of cells as the biofilm continues to propagate. This consequently decreases the gap size and increases the number of gaps in the honeycomb biofilm (Figure 5.2.2). The gaps become increasingly small and are eventually filled by cells (Figure 5.2.2). Substantially fewer gaps remain in the 24-hour dataset. Gaps less than the cell size may be present but have been excluded from these analyses due to user-defined minimum allowable gap sizes. These visual observations are supported with quantitative information extracted from the image via gap analysis (Figure 5.2.2). A single *Pantoea* YR343 cell is 18-38 pixels; the image is approximately 380,000 pixels.

Figure 5.2.2, B illustrates an exponential decrease in average gap size accompanied by an exponential increase in the number of gaps. From this logarithmic behavior we infer *Pantoea* sp. YR343 cells segment gaps in the honeycomb biofilm as part of the biofilm propagation mechanism where one large gap becomes two small gaps, and the average size of these two gaps equates to



**Figure 5.2.1: Time course of *Pantoea* sp. YR343 attachment to Trichloro(1H,1H,2H,2H-perfluorooctyl) silane (PFOTS). Error Bar: 1 Std Dev.**





**Figure 5.2.2: Characterization of *Pantoea* sp. YR343 morphology. (A) Relationship between Average gap size across dataset and time. (B) Relationship between average gap size and number per image, represented by a data point. Representative images from each time point correspond to the pink triangle data point on the plot, scale bar is 50µm.**

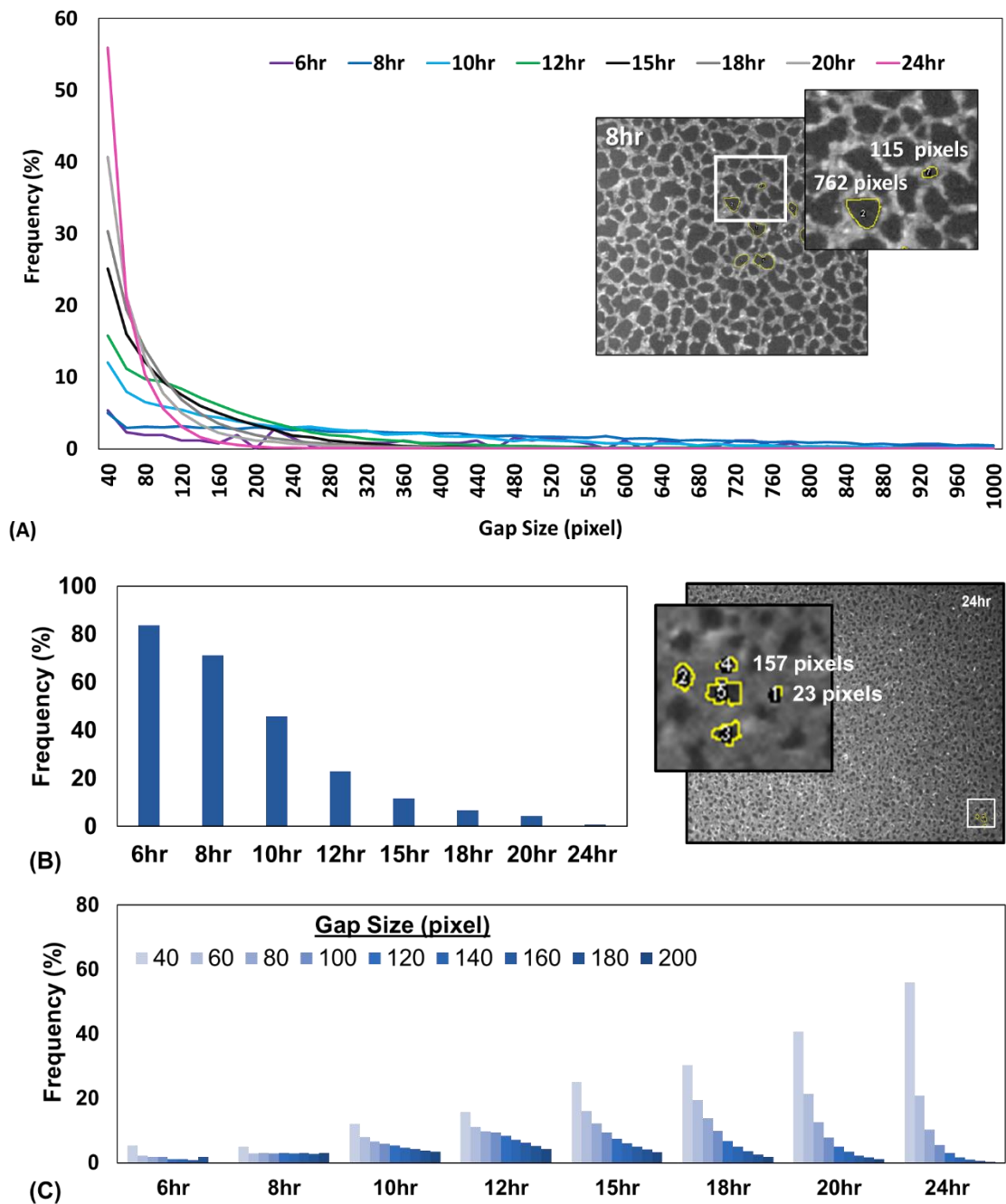


**Figure 5.2.3: Distribution of gap size across *Pantoea* sp. YR343 time points: (A) Distribution of gap size (percentage of gaps exceeding 1,000 pixels size is not shown in plot); inset shows a comparative measure of gap size in pixels; (B) Distribution of gap size greater than 200 pixels; (C) Distribution of gap size less than 200 pixels.**

half the size of the large gap. This behavior follows a slope of -1, which is the approximate slope of the *Pantoea* sp. YR343 dataset in Figure 5.2.2, B between 4 and 15 hours. Many, but not all, of the gaps in the honeycomb biofilm eventually become so small that they are filled by cells (18-24 hours), and this consequently decreases the number of gaps (i.e. creates a bend in the dataset). The representative images shown in Figure 5.2.2, B correspond to the triangle data points and offer a simplified example.

Figure 5.2.3 shows the gap size distribution at each time point. The 4-hour dataset is not included in the distribution because the time point morphology is dominated by unconnected, linear branches of cells. The few gaps that formed during the 4-hour time point are on the order of 10,000 to 100,000 pixels. Approximately 84% of the gaps in the 6-hour dataset exceed 200 pixels, and 71% of the 8-hour dataset (Figure 5.3.2, B). Frequency decreases as gap size increases within each time point, and the magnitude of this trend grows as time progresses. Approximately 40% of the 20-hour dataset is comprised of gaps with less than 40 pixels in size, and this jumps to 60% in 24-hour dataset (Figure 5.2.3, C).

The experimental methods presented here complement the qualitative data gathered from confocal laser scanning microscopy (CLSM) and electron microscopy (Figure 5.2.4). Confocal laser scanning microscopy has the benefit of capturing three-dimensional data and is advantageous for interrogating wet biofilms (Figure 5.2.4, D, E, F). To facilitate CLSM imaging, Trichloro (1H, 1H, 2H, 2H-perfluorooctyl) silane (PFOTS) was applied to a confocal microscopy dish and filled with 3 mL culture of OD<sub>600</sub> 0.1 *Pantoea* sp. YR343. Scanning electron microscopy (SEM) was performed on silicon substrates after fluorescence imaging. SEM can interrogate biofilms on sub-micron scales and can visualize cellular appendages (Figure 5.3.6, C, G). The honeycomb biofilm is visible in the images of each microscopy method, albeit less pronounced in the x-y plane of a wet, three-dimensional biofilm (Figure 5.2.4, B).

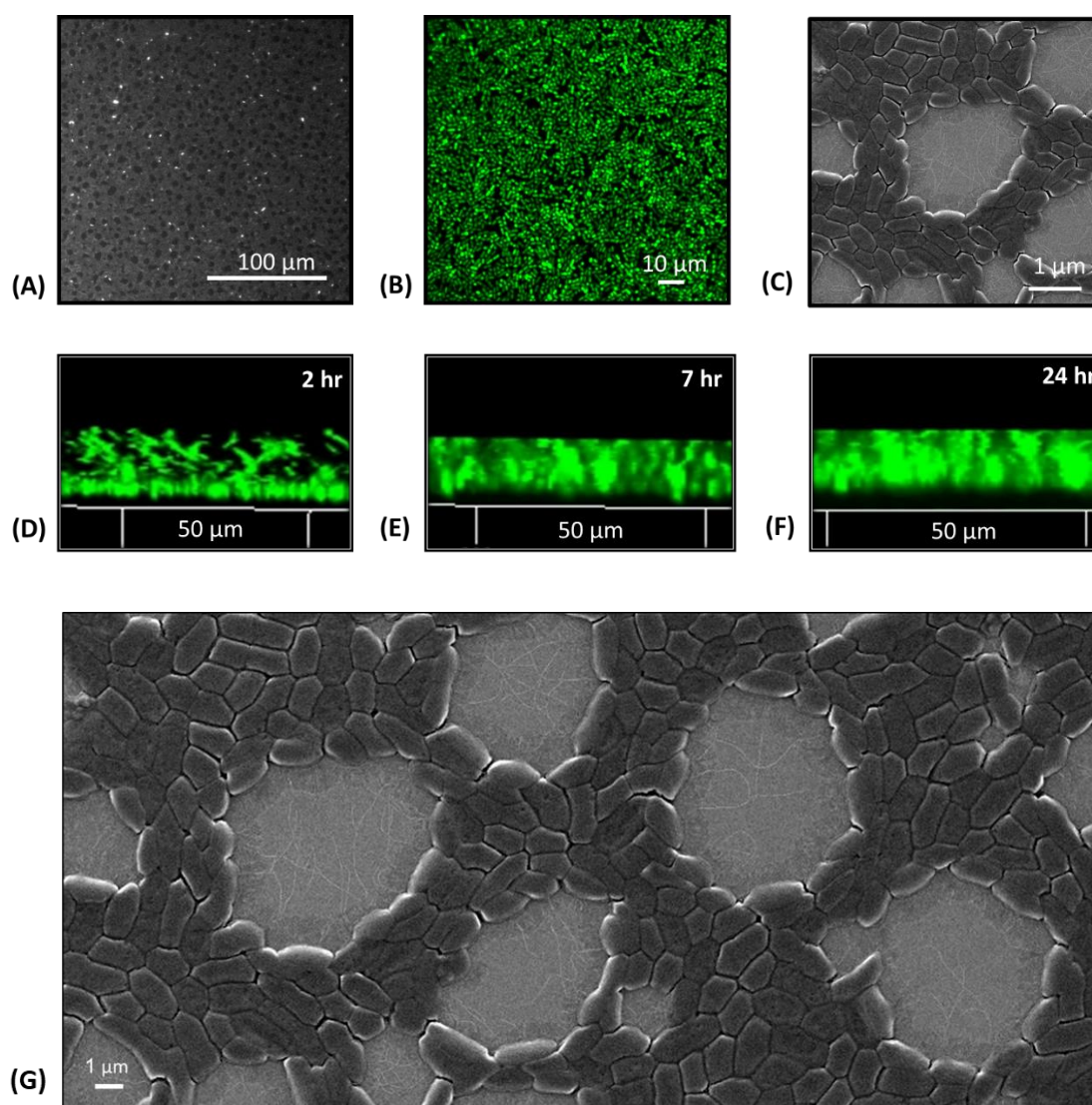


**Figure 5.2.4: An evaluation of *Pantoea* sp. YR343 biofilm propagation on PFOTS-silicon substrate using different microscopy methods. (A) Fluorescence microscopy after 10 hours attachment. Sample was rinsed with 10 mL DI water and dried with pressurized air. (B) Scanning Electron Microscopy after 10 hours of attachment. Sample was rinsed with 10 mL DI water, dried with pressurized air, and coated with 5 nm gold. (C) Wet biofilm at 13 hours, Confocal Laser Scanning Microscopy. (D) Vertical profile of *Pantoea* sp. YR343 biofilm at 2 hours (0-16 μm). (E) Vertical profile of *Pantoea* sp. YR343 biofilm at 7 hours (0-12 μm). (F) Vertical profile of *Pantoea* sp. YR343 biofilm at 24 hours (0-12 μm). (G) *Pantoea* sp. YR343 biofilm propagation on PFOTS-Si substrate, 10 hours (Zeiss Scanning Electron Microscope, 5 nm gold coating).**

The CLSM z-axis profile of the biofilm appears to have a dense layer of cells at 24 hours (Figure 5.2.4, F). Experimentation suggests this profile is comprised of loosely attached cells. These cells may be a result of settling artifacts, or loosely attached cells in a highly porous biofilm. Regardless of origin, these cells are seemingly washed away during the rinse step. Removal of loosely attached cells is necessary in the study of cell-surface interactions to differentiate between cells that have merely settled on the surface (i.e. on top of the biofilm) from cells that are actively part of the biofilm.

Analysis of irreversibly attached cells provides insight on the underlying biofilm foundation, as presented here with enumeration of the *Pantoea* sp. YR343 honeycomb morphology. The CLSM images of a three-dimensional biofilm demonstrate the advantages of using multiple, complementary methods in bacterial biofilm studies.

Porosity and channels have been observed in biofilms. These features are hypothesized to facilitate mass transfer of nutrients, waste, oxygen (Flemming and Wingender, 2010; Petrova and Sauer, 2012; Mosquera-Fernández et al., 2014). The gaps in the honeycomb *Pantoea* sp. YR343 biofilm may serve to facilitate mass transport and exchange of materials. One explanation of the spatiotemporal trend (i.e. gap size decreases as time increases) is that the gap size is greatest when cells are actively growing and dividing (e.g. exponential growth phase). New cells then fill the gaps as the biofilm reaches optimum coverage at stationary growth phase. Additional CLSM experiments are recommended to further assess the three-dimensional component of *Pantoea* sp. YR343 biofilm propagation (section 6.3).

Scanning Electron Microscopy (SEM) is advantageous for close examination of a biofilm. SEM observed a monolayer of cells in the honeycomb biofilm with flagella spanning the gaps (Figure 5.2.4, G). The flagella appear to be intertwined and this

is aligned with the cellular rope observations in Serra et al., (2013). These intertwined flagella may increase adhesion to the surface and thus increase the likelihood that motile cells attach by providing a point for attachment. The flagella may even guide nascent cells to segment the gap. Occasionally chains of cells extend from one side of the biofilm into part of the gap. Alternatively, the flagella may be independent of the honeycomb morphology. These flagella could be the remains of loosely attached cells, tethered by the flagella, that were removed during the rinse step. These observations spurred us to initiate experiments with the *Pantoea* sp. YR343 flagella mutants.

### **5.3 The Influence of FliR on *Pantoea* sp. YR343 Biofilm Propagation.**

Flagella play a key role in the initial stages of biofilm formation. In addition to providing a motor for swimming and surface motility flagella can mediate attachment by overcoming repulsive forces near the surface (Lemon, Higgins, and Kolter, 2007; Petrova and Sauer, 2012; Friedlander et al., 2013; Friedlander et al., 2015; Kearns, 2010; Guttenplan and Kearns, 2013; Berne et al., 2018). Flagella increase the surface area of attachment and have been shown to anchor cells to surfaces (Lemon, Higgins, and Kolter, 2007; Tuson and Weibel, 2013; Friedlander et al., 2013; Friedlander et al., 2015; Berne et al., 2018). Like *Pantoea* sp. YR343, *Listeria monocytogenes* form honeycomb biofilms and flagella have been demonstrated to play an integral role in this morphology as the absence of flagella resulted in unstructured biofilms (Lemon, Higgins, and Kolter, 2007; Guilbaud et al., 2015). In spatiotemporal experiments with *Escherichia coli*, Serra et al. found mutants that could not rotate their flagella and mutants lacking flagellar filaments were defective in forming a honeycomb pattern (2013). Here we examined the impact of mutations in the flagella protein FliR on *Pantoea* sp. YR343 biofilm attachment and morphology.

## Results and Discussion

FliR is a conserved integral protein in the basal body complex that plays a key role in the structure and function of the flagellar export apparatus (Nakamura and Minamino, 2019) (Figure 1.1.5). Using this mutant, we found that the area coverage of  $\Delta$ fliR biofilms is approximately half that of wildtype biofilms, yet the standard deviation is approximately doubled (Figure 5.3.1). The variation may be explained by the decrease in surface adhesion due to loss of the flagella adhesin. When examined with SEM, no flagella were observed on the mutant cells (Figure 5.3.2). Consistent with previous reports, a lack of flagella adhesin or defects to the flagella adhesin likely explains the  $\Delta$ fliR area coverage and variation (Lemon et al., 2007; Serra et al., 2013; Friedlander et al., 2013; Friedlander et al., 2015). Relatively large sections of the biofilm appeared to detach during the rinse step, and these experimental observations align with the notion that the  $\Delta$ fliR biofilm lacks enough adhesion.

Using our image processing algorithm, we quantified *Pantoea* sp. YR343  $\Delta$ fliR biofilm morphology compared to wild type cells (Figure 5.3.3). This analysis shows that there are dramatic differences in the gap size distribution, with many of the gaps in the *Pantoea* sp. YR343  $\Delta$ fliR dataset exceed 200 pixels (Figure 5.3.3, A). Interestingly, gap sizes below 200 pixels in the  $\Delta$ fliR dataset are evenly distributed across time points (Figure 5.3.3, B). This is consistent with Figure 5.3.4 which shows a scattered relationship between average gap size and number that does not change with respect to time.

*Pantoea* sp. YR343  $\Delta$ fliR seemingly follows the same spatial trend as *Pantoea* sp. YR343 WT between average gap size and number of gaps in an image but *Pantoea* sp. YR343  $\Delta$ fliR does not progress at the same rate (Figure 5.3.4). This is likely explained by the high degree of variation in *Pantoea* sp. YR343  $\Delta$ fliR dataset across time points. Figure 5.3.4, B captures the differences in the *Pantoea*

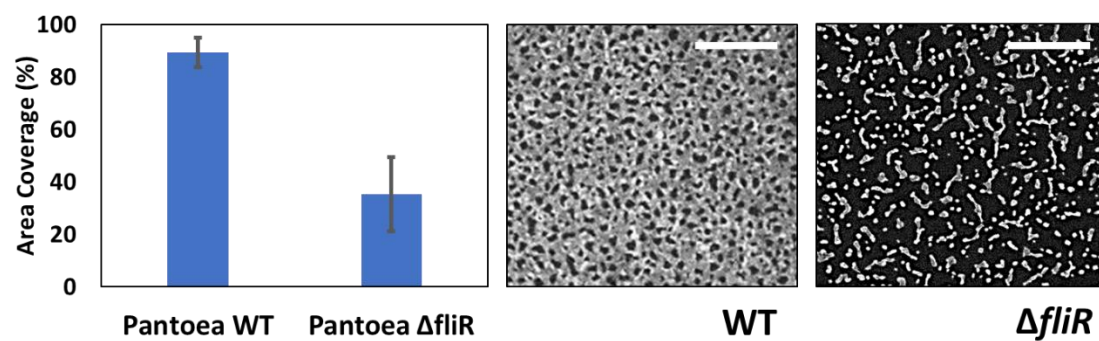


**Figure 5.3.1: Effect of *Pantoea* sp. YR343  $\Delta$ *fliR* mutants on attachment to PFOTS-Silicon substrate, area coverage after 24 hours. Scale bar 25  $\mu$ m.**



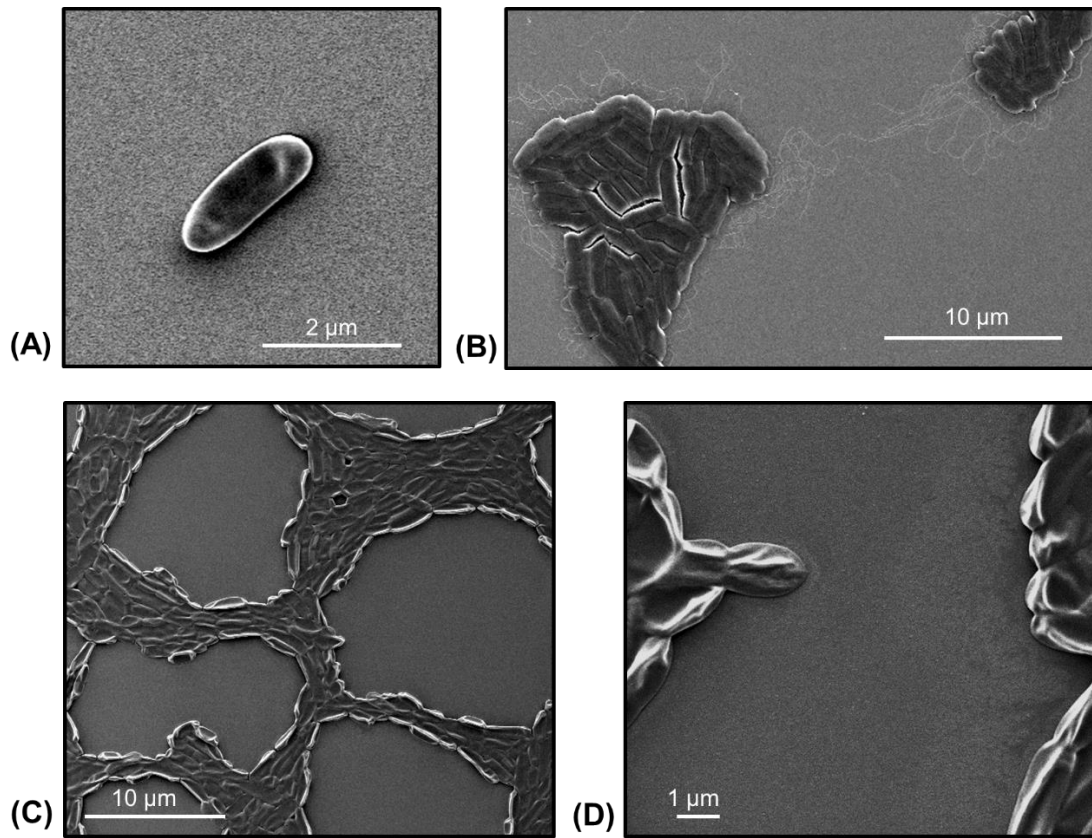


**Figure 5.3.2: Early attachment of *Pantoea* sp. YR343 WT and flagella mutants to PFOTS-Si substrate (Zeiss Scanning Electron Microscope, 5 nm gold coating). (A) *Pantoea* sp. YR343  $\Delta fliR$ , 3 hours. (B) *Pantoea* sp. YR343 WT 4 hours. (C, D) *Pantoea* sp. YR343  $\Delta fliR$  mutant on PFOTS-Si substrate, 24 hours (Zeiss Scanning Electron Microscope, 5 nm gold coating).**

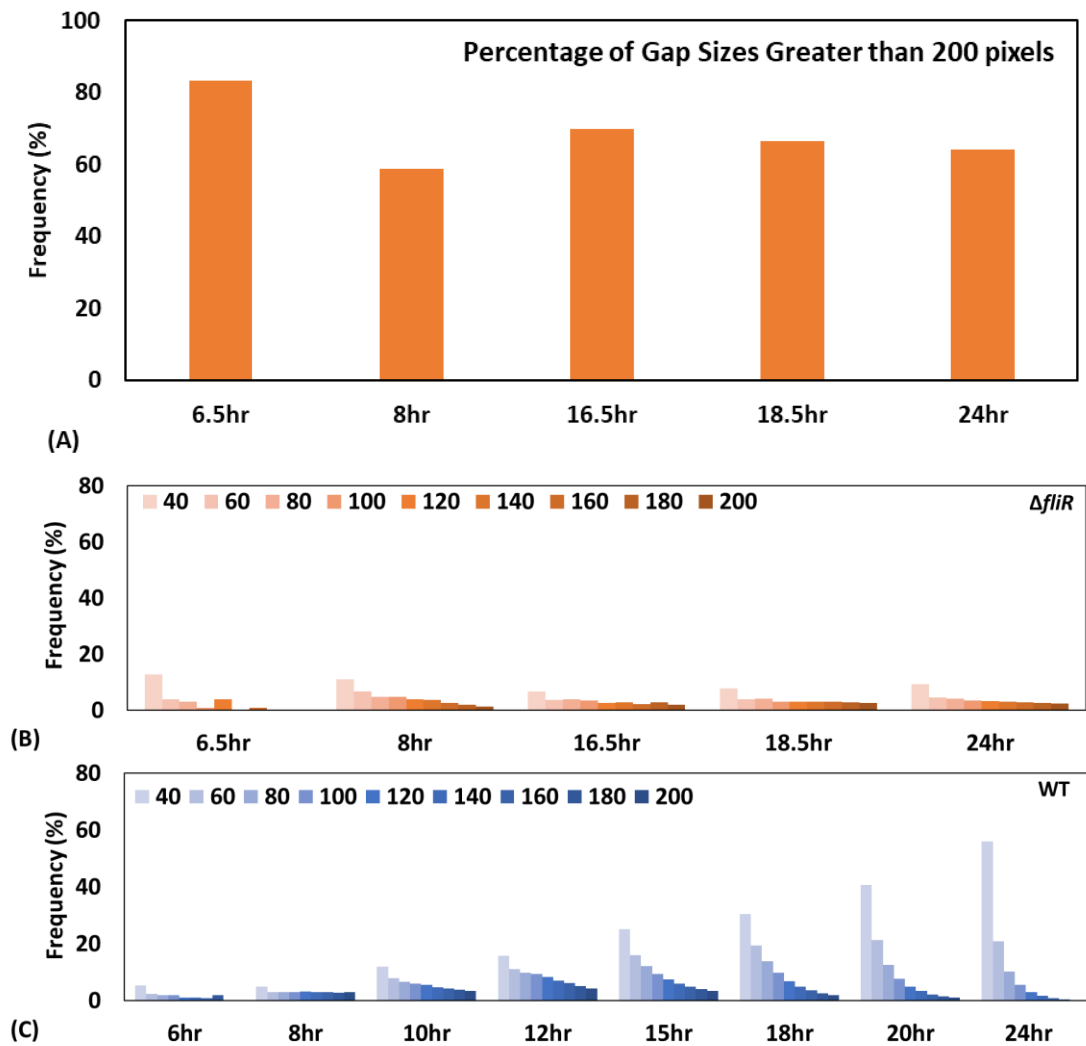


**Figure 5.3.3: *Pantoea* sp. YR343  $\Delta fliR$  gap distribution compared to WT. Percentage of greater than 200-pixel size (A). Distribution of *Pantoea* sp. YR343  $\Delta fliR$  (B) vs. *Pantoea* sp. YR343 WT (C).**

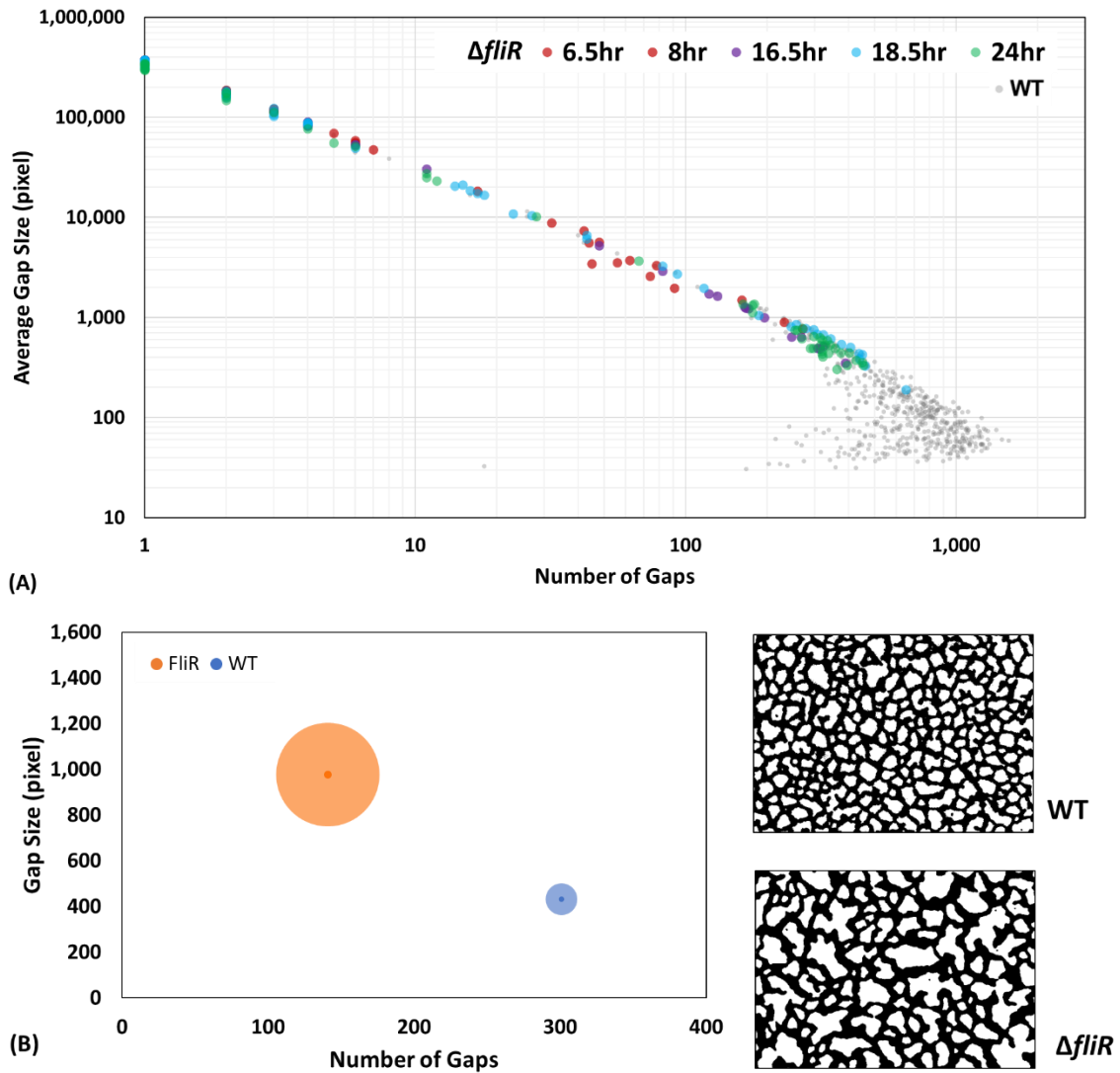


**Figure 5.3.4: Differences between *Pantoea* sp. YR343 WT and *Pantoea* sp. YR343  $\Delta fliR$  biofilm morphology. (A) Relationship between  $\Delta fliR$  average gap size and number per image, represented by each data point and overlaid on WT dataset. (B) Quantitative comparison of biofilm morphology where bubble size denotes standard deviation in gap size, with representative images for *Pantoea* sp. YR343 WT (53% area coverage) and *Pantoea* sp. YR343  $\Delta fliR$  (52% area coverage).**

sp. YR343  $\Delta fliR$  and WT morphology by comparing metrics of two (representative) biofilm images with equal surface area coverage. The radius of the bubble corresponds to the standard deviation in the image gap size, and the dot in the center of the bubble indicates the average gap size for each image. The radius of the bubble is independent of the gap number and is represented by bubble position. These results suggest FliR protein wields a critical influence on *Pantoea* sp. YR343 biofilm propagation.

A flagella deletion mutant is recommended for future experimental work to confer the importance of flagella on *Pantoea* sp. YR343 biofilm propagation and morphology. Paralyzed flagella mutants, such as mutations to the motor complex, are also recommended for future work. The paralyzed flagella mutants will not be motile, but the mere presence of flagella may assist cell-surface adhesion. This experimental work might inform on the mechanism of honeycomb morphology and the degree to which the morphology is biologically mediated. If the biofilm propagation and morphology of the paralyzed flagella mutant matches that of WT, this would suggest the flagella adhesion is attributed to physical interactions with the surface chemistry.

## 5.4 Materials and Methods

### *Surface chemistry modification*

Silicon wafers, coated with 10 nm silicon dioxide (thermal oxide process: Temperature: 1000°C, O<sub>2</sub>: 3000sccm, H<sub>2</sub>O: 3ml/min, Pressure: 1atm, Time: 80 min), were diced into 20 mm by 20 mm square chips with dicing saw. The chips were cleaned with pressurized air with a 0.2  $\mu$ m filter, followed by a minimum of 5 minutes in a Harrick Plasma PDC-001 air plasma cleaner (Ithaca, NY). Vapor deposition was performed in an enclosed dish on a hot plate with the following methods: 20 $\mu$ L/ 80 cm trichloro(1H,1H,2H,2H-perfluorooctyl) silane (PFOTS) (Sigma-Aldrich, St. Louis, MO), 4 hours at 85°C; 40 $\mu$ L/ 80 cm APTMS, 2 hours at

150°C; 40µL/ 80 cm, 2 hours at 150°C, followed by 2 hours no heat for OTS; 6hours 150°C for MTMS.

### *Bacterial Culture and Device Testing*

Engineered strains of *Pantoea sp. YR343* expressing green fluorescent protein were engineered by expression of EGFP from a Gate-way modified pBBR1-MCSe plasmid, maintained with 10 µg gentamycin, ml (Pelletier et al., 2008). *Pantoea sp. YR343* were inoculated in of R2A liquid medium (from a plate of R2A agar) and grown to stationary phase overnight. A 1:100 dilution was performed, and the culture was grown to early exponential phase (approx. 4hrs) and diluted to an optical density (OD<sub>600</sub>) of 0.1 (at 600nm), verified with a BioTek Synergy 2 microplate reader, 600 nm.

The silane-treated substrates were each placed in concave dishes and filled with 3 mL of *Pantoea sp. YR343* liquid culture, 0.1 OD<sub>600</sub>. Upon inoculation, the dishes were covered and let sit for a specified amount of time. Tweezers removed the substrate from the liquid culture at a designated time point. The substrate was rinsed with 10 mL DI water to remove loosely attached cells, and dried with pressurized air, 0.2 µL filter, to minimize drying artifacts.

### *Sample Imaging*

Image data was collected with an Olympus IX51 microscope (Shinjuku, Tokyo) complete with an epifluorescence using a Chroma 41001FITC (Bellows Falls, VT) filter cube (480nm excitation band pass filter with a 40nm band width and 535nm emission band pass filter with a 50nm band width). FEI Novalab 600 Dual-Beam System was used to collect Scanning Electron Microscopy (SEM) images of the *Pantoea sp. YR343* cell attachment. Confocal fluorescence microscopy was performed using a Zeiss LSM710 confocal laser scanning microscope with a Plan-Apochromat 63x/1.40 oil immersion objective (Carl Zeiss Microimaging, Thornwood, NY).

### *Image Processing and Cell Quantification*

Images were analyzed in Fiji ImageJ. Image processing was executed with semi-automated scripts to generate binary images. Scripts were tailored for each stack of images, but all scripts applied built-in functions for background subtraction, threshold, and filters. The binary images were manually adjusted to match the original image. To extract numerical data from the honeycomb biofilm, another image script inverted each image and applied the built-in particle analysis function with a limit of 18 pixels. By inverting the images, the biofilm gaps became the region of interest and facilitated collection of morphology data. The built-in particle analysis function collected data on total particle area, percent area coverage, average particle size, and the number of particles. Cell area coverage was calculated by subtracting the gap area coverage percent from one hundred.

### *Mutant strain construction*

These methods are described fully in Bible et al. (2020). In short, biparental mating introduced the plasmid pRL27 and encoded a mini-Tn5 transposon into *Pantoea* sp. YR343 (DGC2884 pSRK-Gm). *Pantoea* sp. YR343 was grown in the presence of kanamycin (50  $\mu\text{g mL}^{-1}$ ) and gentamycin (10  $\mu\text{g mL}^{-1}$ ) to remove *E. coli* strain EA145 (Bible et al., 2020). The transposon library was screened, and genomic DNA was isolated from each mutant using the Promega Wizard Genomic DNA Extraction Kit, (Bible et al., 2020). Colonies were picked, the plasmid DNA was isolated with the QIAprep Spin Miniprep Kit (Qiagen), and plasmids were sequenced at the Molecular Biology Resource Facility at the University of Tennessee, Knoxville (Bible et al., 2020). The plasmids were sequenced using the primers tpnRL17-1 and tpnRL13-1, and the results were analyzed using BlastX from NCBI to identify the region of DNA flanking each transposon (Bible et al., 2020).

## **CHAPTER SIX FUTURE DIRECTIONS**

This section presents preliminary results from biofilm experiments with *Pantoea* sp. YR343. Additional experimental replicates are recommended as part of the future work. Prescription of future experiments for the study of *Pantoea* sp. YR343 biofilms are also included in this section. Temperature was found to affect the rate of *Pantoea* sp. YR343 biofilm propagation; thus, temperature should be recorded in all future *Pantoea* sp. YR343 experiments. A temperature-controlled lab environment is recommended for all future work.

### **6.1 The Effect of Temperature on *Pantoea* sp. YR343 Biofilm Propagation**

The bulk of the experimental work in Chapter 5 was conducted in lab room temperatures estimated to be in the low sixties (15-17°C). On several occasions the air-conditioned lab environment was exceptionally cold and estimated to be in the fifties (10-15°C). Despite these qualitative observations in the temperature, the experiments were reproducible, and there were no observable effects on *Pantoea* sp. YR343 biofilm formation. For this reason, temperature was not recorded as part of the experimental methods. After some time, there were system changes to the building heating, ventilation, and air conditioning (HVAC) unit. The lab warmed to normal room temperature conditions (20-22°C). The increase in temperature environment increased the rate of *Pantoea* sp. YR343 biofilm formation (Figure 6.1.1, A). Changes to the HVAC system occurred in 2019, thus the “2019” dataset label. The original dataset was collected in 2018 and 2019 but is simplified as the “2018” dataset.

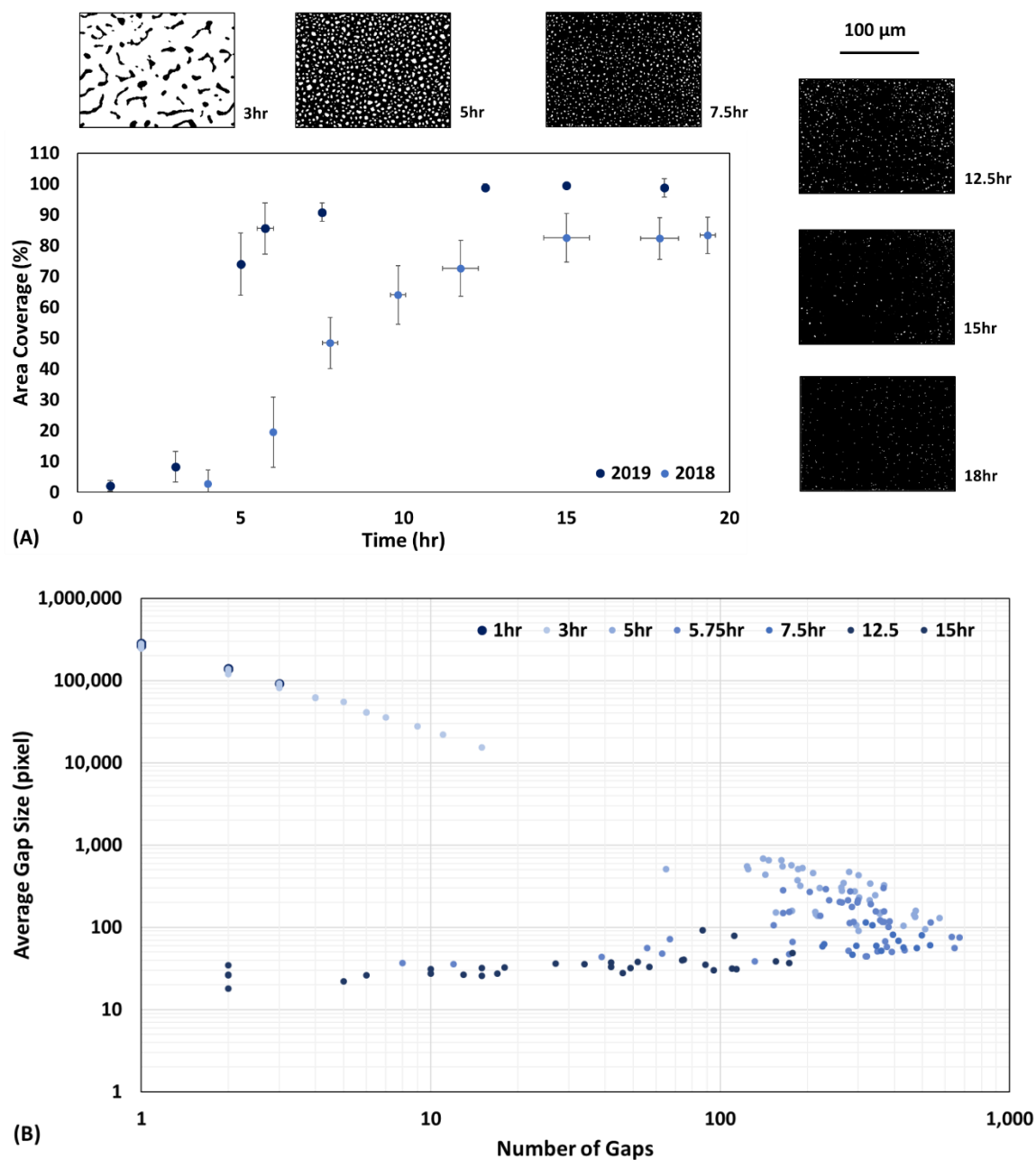


**Figure 6.1.1: *Pantoea* sp. YR343 biofilm propagation and morphology in normal room temperature conditions. (A) Time course of *Pantoea* sp. YR343 attachment to Trichloro(1H,1H,2H,2H-perfluorooctyl) silane (PFOTS) for 2018 and 2019 datasets; Error Bar: 1 Std Dev. (B) Relationship between gap size and number. Each data point corresponds to the average gap size in an image and the total number of gaps in the image.**



The *Pantoea* sp. YR343 biofilm maintained the honeycomb morphology pattern in the 2019 dataset and propagation occurred at a much faster rate. The 2019 dataset exceeded 90% surface area coverage after just 8 hours, whereas the 2018 dataset only reached 50% area coverage. The 2019 dataset followed the same spatial trend between average gap size and number of gaps in an image (Figure 6.1.1, B). Many of the images approached the limit of complete surface area coverage, indicated by the number of data points with only 10-100 gaps per image.

Temperature appears to effect biofilm formation of the *Pantoea* sp. YR343  $\Delta fliR$  mutant, albeit the relationship is less prominent, which may be due to the high degree of variation in the *Pantoea* sp. YR343  $\Delta fliR$  mutant datasets (Figure 6.1.2). The effect of temperature on the *Pantoea* sp. YR343 biofilm propagation may be explained by extrapolymeric substance (EPS). Previous studies identified an optimum temperature between 20-31°C for extrapolymeric substance (EPS) formation, and previous work found a decrease in 10°C below the optimum temperature hindered EPS production (Gupta et al., 2020; Gandhi et al., 1997; Sutherland, 2001a; Sutherland 2001b). The optimum temperature of the *Pantoea* sp. YR343 is 28°C, thus experimental conditions between 15-17°C would suppress EPS production (Bible et al., 2016). The increased rate of biofilm propagation in the 2019 dataset may be a result of combined adhesion from flagella and EPS, as compared to the flagella being the primary route for adhesion in the 2018 dataset. Interestingly, temperature did not appear to have a large effect on the cell numbers in the bulk solution (Figure 6.1.2, B).

*Pantoea* sp. YR343 in the bulk solution reached stationary phase after approximately 15 hours for both datasets. The liquid culture was mixed and sampled to measure optical density of the bulk solution after the substrate was removed (recall experimental setup in Figure 5.1.1). Most of the substrate was covered by the honeycomb biofilm after 10 hours, 2018 dataset, and after just 5 hours, 2019 dataset.

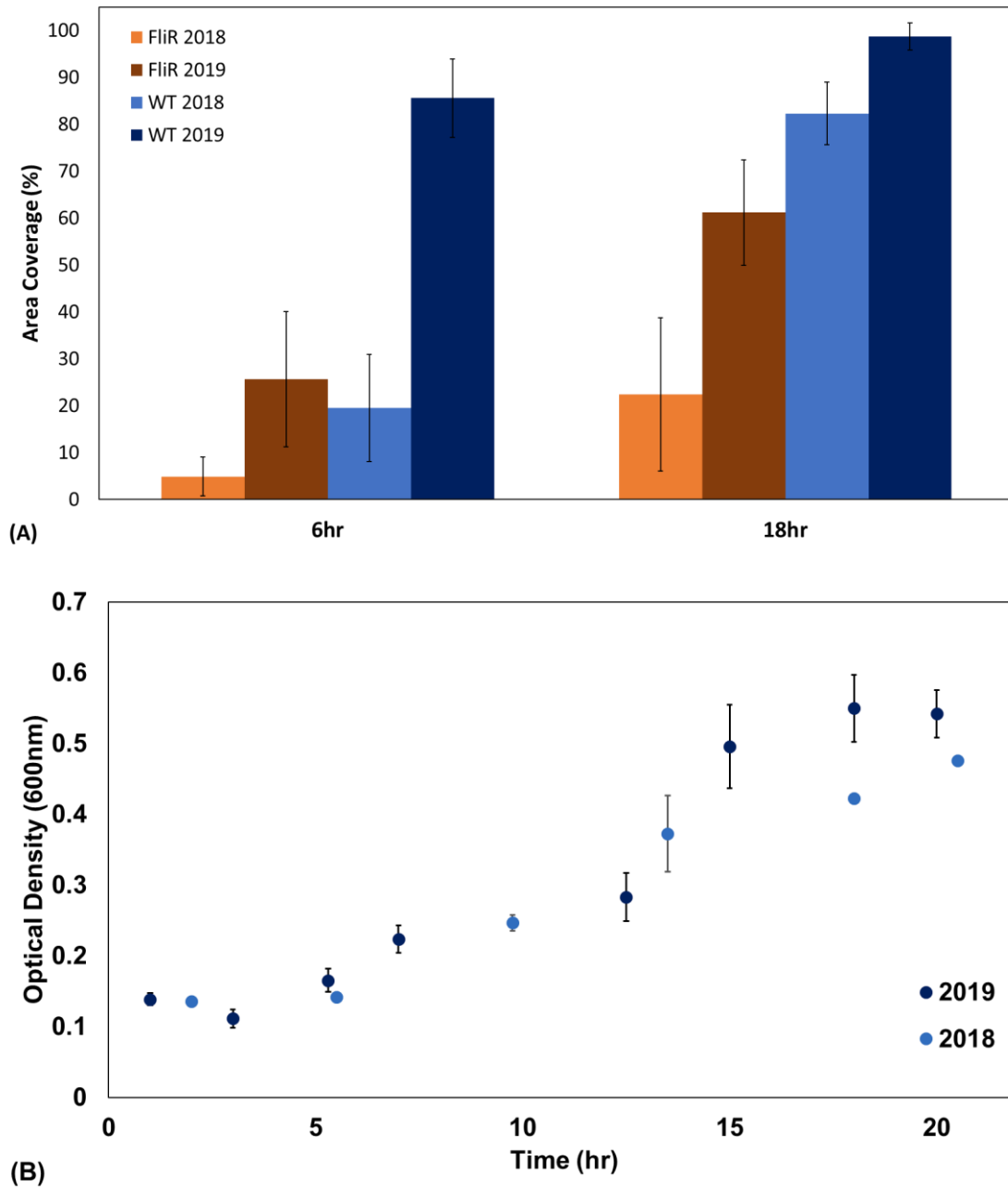


**Figure 6.1.2: The effect of temperature on *Pantoea* sp. YR343. (A) Comparing the effect of temperature on WT and  $\Delta fliR$  attachment to Trichloro(1H,1H,2H,2H-perfluorooctyl) silane (PFOTS); Error Bar: 1 Std Dev. (B) The effect of temperature on the cell number in the bulk solution.**

In sum, temperature appears to have a substantial effect on the biofilm yet little effect on *Pantoea* sp. YR343 in the liquid culture. These findings are consistent with the *Listeria monocytogenes* biofilm literature, which found an increase in attachment of *L. monocytogenes* to stainless steel with an increase in temperature, independent of the cell concentration in bulk solution (Chavant et al., 2002; Mai & Corner, 2007).

Differences in the 2018 and 2019 datasets exposed the effect of temperature on *Pantoea* sp. YR343 biofilm propagation. This work should be repeated in a controlled environment with incremental temperatures to pinpoint an optimum temperature for *Pantoea* sp. YR343 biofilm propagation. Incorporating EPS mutants and flagella mutants into controlled temperature experiments can elucidate which of these adhesins, if any, are affected by temperature.

## **6.2 The Influence of Cell Recruitment and Attachment on Honeycomb Biofilm Morphology**

To understand the contribution of cell attachment on biofilm growth, *Pantoea* sp. YR343 biofilms were grown in R2A medium. Cells attached to the substrate, from a liquid culture, during a specified seeding period (Figure 6.2.1). The substrate is removed from the culture, rinsed with DI water, and placed in new medium. The preliminary results found *Pantoea* sp. YR343 biofilms, with a seeding period of 3 hours, continued biofilm growth in new medium (Figure 6.2.2). The seeded biofilm lags the standard culture, and this lag could be due to the stress of rinsing the cells with distilled water, or from the lack of cells attaching from liquid culture. Figure 6.2.2 demonstrates the seeded *Pantoea* sp. YR343 cells continue honeycomb biofilm propagation in new media. Optical density (OD<sub>600</sub>) of the liquid culture was measured after the substrate was removed, and these results suggests cells were present in bulk solution (Table 6.2.1). Flow cell experiments are recommended to

**Table 6.2.1: Optical Density at 600 nm of liquid media after the substrate was removed from liquid culture.**

	WT		$\Delta fliR$	
Total Time	Seed	Standard	Seed	Standard
13-hour	$0.26 \pm 0.03$	$0.28 \pm 0.03$	$0.09 \pm 0.03$	$0.42 \pm 0.06$
15-hour	$0.31 \pm 0.06$	$0.50 \pm 0.05$	$0.10 \pm 0.02$	$0.49 \pm 0.05$

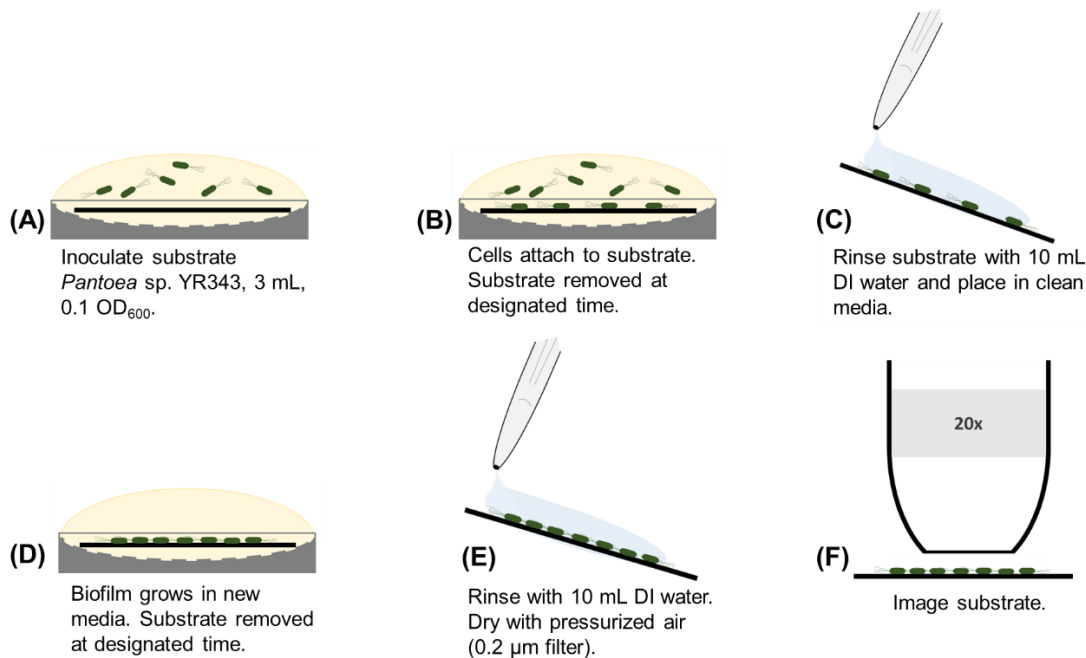
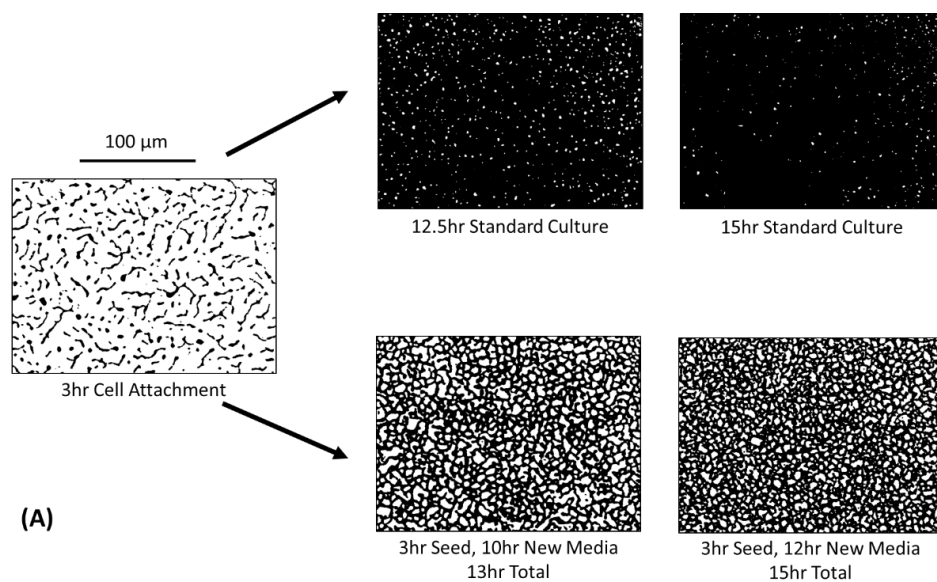
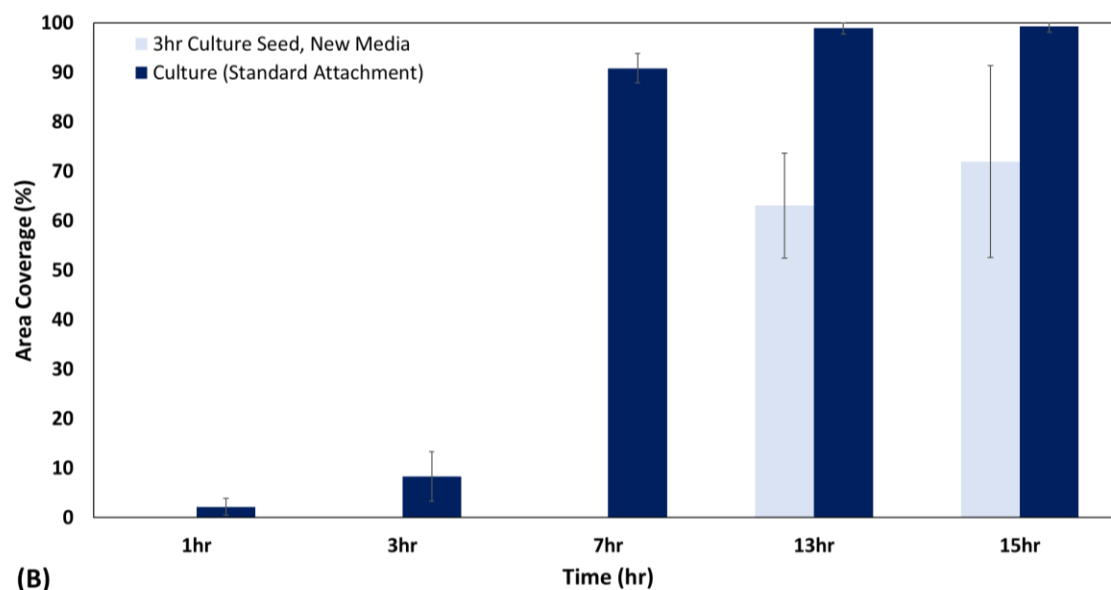


**Figure 6.2.1: Biofilm assay methods for functionalized silane platform. (A)** Substrate were submerged in 3 mL of R2A growth medium inoculated with *Pantoea* sp. YR343-GFP at an optical density (OD<sub>600</sub>) reading of 0.1, and **(B)** nucleation sites form. **(C)** Substrate is removed after a seed period, rinsed with 10 mL of DI water. **(D)** Substrates are placed in new media and incubated. **(E)** Substrate is removed at designated time, rinsed with 10 mL of DI water, and dried with pressurized air (0.2  $\mu$ m filter). **(F)** Imaging was carried out with a with 20x objective.



(A)



(B)

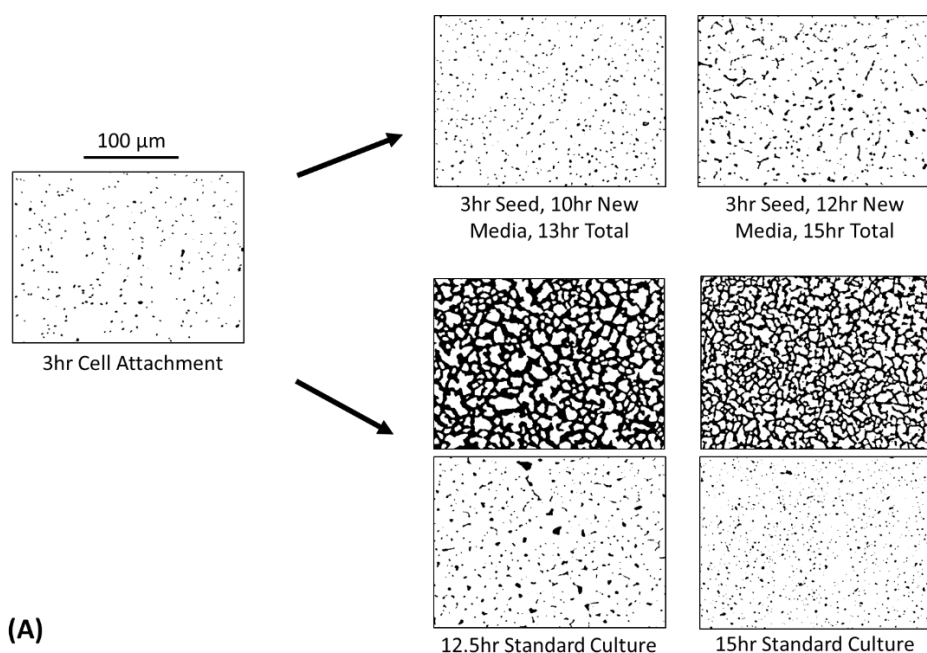
**Figure 6.2.2: *Pantoea* sp. YR343 WT attachment to PFOTS-Silicon substrate. (A) The role of cell attachment on *Pantoea* sp. YR343 WT biofilm propagation where “seed” signifies the cell attachment period (B) Area coverage of a 3-hour seed culture compared to standard culture.**

fully remove cells from bulk solution to understand the role of cell division on biofilm growth and honeycomb morphology. Such experiments can be combined with confocal microscopy for single cell resolution and imaging of the wet biofilm.

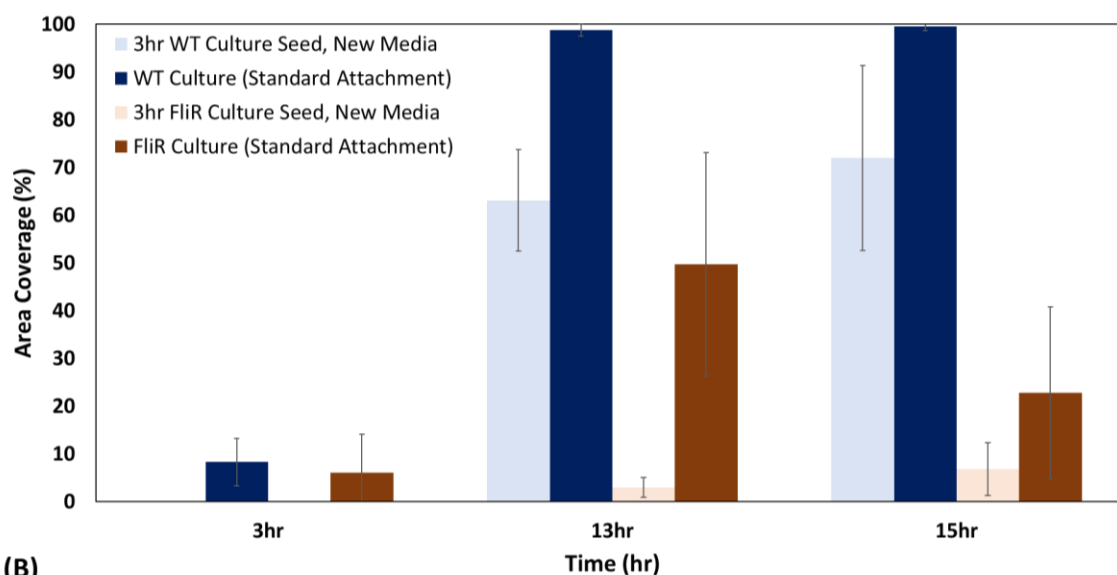
Unlike *Pantoea* sp. YR343 WT, propagation of the *Pantoea* sp. YR343  $\Delta fliR$  biofilm appears to stop after the seeding period (Figure 6.2.3). *Pantoea* sp. YR343 WT appears to establish adequate cell anchors after 3 hours (Figure 6.2.3). A look at shorter WT seed times suggests that *Pantoea* sp. YR343 must establish cell anchors, before the rinse step, for the biofilm to continue growth in new medium (Figure 6.2.4). By this logic, *Pantoea* sp. YR343  $\Delta fliR$  biofilms do not propagate in new medium because cell anchors did not adequately form within this timeframe (Figure 6.2.3 and 6.2.4). This is consistent with the  $\Delta fliR$  compromising the flagella adhesin.

Biofilms are famously known to withstand environmental stressors. Figure 6.2.4 suggests the *Pantoea* sp. YR343 cannot establish adequate cell anchors during the 1-hour seed culture, implying that biofilm genes were not expressed. If essential biofilm genes are not expressed after 1-hour seed culture, the attached cells likely perish during the rinse step, therefore a biofilm does not form in new medium. Alternatively, Figure 6.2.4 may be explained by the messenger signaling molecule cyclic diguanylate monophosphate (c-di-GMP) which is closely linked to biofilm formation (Bible et al., 2020). The attached cells in the 1-hour seed culture may survive the rinse-step, but c-di-GMP levels are suppressed due to the seemingly inhospitable environment (Bible et al., 2020). Chemical analysis on the bulk solution may yield insight on signaling molecules in future experiments.

A seeding period of 5 hours is recommended for *Pantoea* sp. YR343  $\Delta fliR$  biofilm experiments to test whether the  $\Delta fliR$  biofilm failed to propagate because the number of attached cells did not reach a minimum threshold. *Pantoea* sp. YR343



(A)



(B)

**Figure 6.2.3: *Pantoea* sp. YR343 WT and  $\Delta fliR$  attachment to PFOTS-Silicon substrate. (A) The role of cell attachment on *Pantoea* sp. YR343  $\Delta fliR$  biofilm propagation where “seed” signifies the cell attachment period; two images represent the variation in the  $\Delta fliR$  biofilm for the time point. (B) Area coverage of a 3-hour seed *Pantoea* sp. YR343 WT and  $\Delta fliR$  cultures compared to the respective standard cultures.**

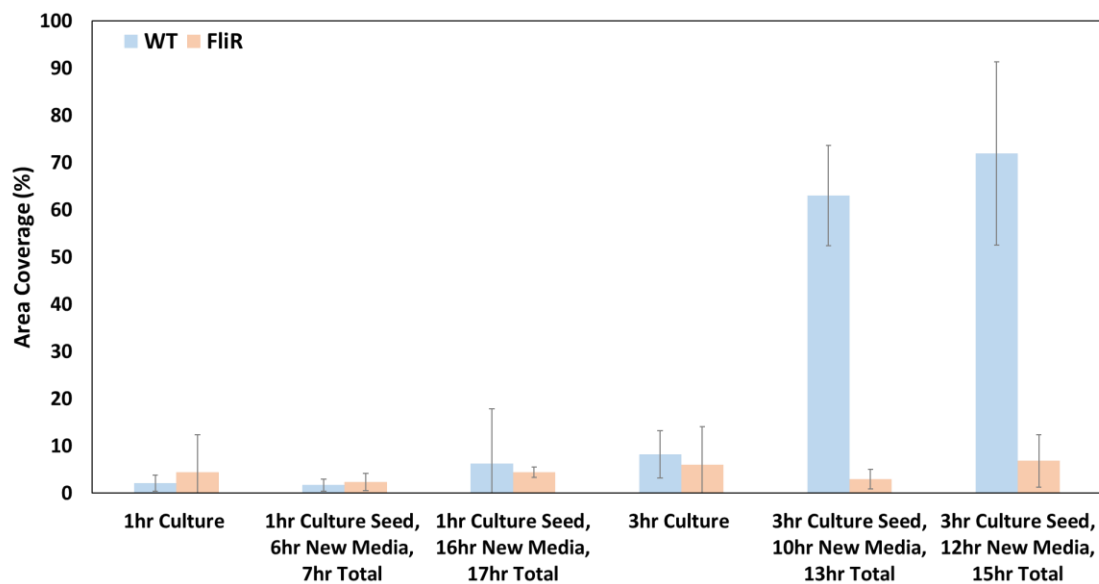


**Figure 6.2.4: *Pantoea* sp. YR343 WT and  $\Delta fliR$  attachment to PFOTS-Silicon substrate with 1-hour and 3-hour “seed” attachment. Cells attached during the seed period, then the substrate was removed from the culture, rinsed with DI water, and placed in new medium.**



*ΔfliR* biofilm averages 13% surface area coverage after 5 hours, 11% standard deviation. Extra replicates will address the variation in area coverage for *Pantoea* sp. YR343 *ΔfliR* seeding experiments.

### **6.3 Next Steps: Investigate *Pantoea* sp. YR343 biofilm propagation with Confocal Laser Scanning Microscopy**

Confocal Laser Scanning Microscopy (CLSM) is a powerful tool for studying bacterial biofilms. CLSM experiments may illuminate insight on the *Pantoea* sp. YR343 honeycomb biofilm propagation and morphology. Time lapse seed experiments with CLSM will help to distinguish between biofilm growth (on the surface) and cell attachment (from bulk solution). This section reflects on past observations from CLSM microscopy, outlines futures experiments, and presents hypotheses pertaining to the *Pantoea* sp. YR343 honeycomb biofilm. The CLSM microscopy experiments will benefit from a flow cell set-up, but it is not required. Flow cells remove cells that may be present in bulk solution and reduce background fluorescence.

Previous confocal microscopy work (section 5.2) observed three-dimensional profiles of *Pantoea* sp. YR343 biofilm extending past 12  $\mu\text{m}$  at 24 hours. Imaging from the “top” of the biofilm (CLSM, x-y plane), a number of the fluorescent cells appeared to be spinning like a ball joint, as though tethered. This is consistent with the literature and the idea that flagella tether cells to the surface and each other (Petrova and Sauer, 2012; Friedlander et al., 2013; Serra et al., 2013; Guttenplan and Kearns, 2013; Steinberg and Kolodkin-Gal, 2015; Bennett et al., 2016). This observation also begets whether the monolayer biofilm is the scaffold of a highly porous biofilm anchored by flagella, and otherwise loosely attached. The cells may have been sheered from the flagella during the rinse step, possibly explaining the flagella mesh in the center of the gaps.

Questions surrounding the *Pantoea* sp. YR343 three-dimensional biofilm structure can be addressed with a CLSM time-lapse, seed experiment. This experiment will follow previous experimental methods with a few exceptions. Trichloro (1H, 1H, 2H, 2H-perfluorooctyl) silane (PFOTS) is applied to a confocal microscopy dish to facilitate high-resolution imaging of a wet biofilm. A 3 mL culture of OD<sub>600</sub> 0.1 *Pantoea* sp. YR343 is seeded for 3 hours on the confocal microscopy dish, rinsed with 10 mL of distilled water, and replenished with 5 mL new medium. The confocal microscopy dish is then set-up for a CLSM time-lapse of an area with attached cells. This experiment eliminates the possibility that a three-dimensional biofilm is an artifact of cells settling to the surface. This time-lapse experiment will elucidate how the biofilm propagates in the x-y plane and z-axis. The time-lapse will capture images at a specified interval (e.g. 30 min) on the x-y plane and perform a three-dimensional scan. An automated imaging program can be set-up for a period of 24 hours to capture the evolution of the *Pantoea* sp. YR343 morphology from multiple dimensions. The three-dimensional scans will provide insight on the biofilm architecture; Serra et al., observed three-dimensional honeycomb biofilm morphology in *Escherichia coli* with CLSM imaging (2013).

This experiment can be modified to investigate the role of flagella in *Pantoea* sp. YR343 biofilm propagation. One modification is to perform this experiment with a *Pantoea* sp. YR343 with a flagella deletion strain. If the biofilm propagates in multiple dimensions, then the flagella is not critical to *Pantoea* sp. YR343 biofilm propagation. A second modification is to perform the seed experiment with a seed time-lapse experiment with a flagella label to visualize how the flagella may influence biofilm propagation. Following the procedure outlined in Zhao et al., *Pantoea* sp. YR343 can be engineered to include a tetracysteine tag into the flagellin. FIAsh/ReAsH is a high affinity, high specificity dye, that can be added to the medium, post-seed, for real-time imaging, and has the advantage of remaining non-fluorescent until it binds to the tetracysteine tag. Different fluorescent colors should be used for the flagella and the rest of the cell.

Many insights can be gained from such an experiment. First, the dye will illuminate whether daughter cells retain flagella, and if those cells remain attached to the surface or detach. If daughter cells retain flagella and remain attached to the surface, then this would indicate the flagella are integral to *Pantoea* sp. YR343 biofilm formation, beyond initial attachment and adhesion. Short intervals or videos may be needed to capture this evolution. If daughter cells retain flagella, then the dye may illuminate whether the presence of flagella precede cells in segmenting gaps in the honeycomb biofilm (i.e. cells attach next to or on top of flagella). Such behavior might suggest the flagellar appendages “reach” or “grasp” for cells to improve adhesion, as Friedlander et al. observed with *E. coli* (2013). Lastly, if a three-dimensional biofilm structure forms, the dye may illuminate whether the flagella plays a structural role in the three-dimensional architecture.

Lastly, PFOTS can be patterned onto a confocal microscopy dish (section 2.4), and incorporated into another iteration of the experiment, to ascertain whether *Pantoea* sp. YR343 can use flagella to overcome undesirable surfaces (e.g. glass) in biofilm propagation. In sum, there is much promise for CLSM time-lapse experiments, and this work will complement the high-throughput image processing script.

## **6.4 Concluding Remarks**

Microbial systems inconspicuously influence our world. From soils to bioreactors, bacteria have a dramatic effect on natural and synthetic environments alike. The ability to understand, optimize, and direct the activity of complex microbial systems holds significant potential for the bioeconomy and society at large. Nanofabrication techniques can complement conventional laboratory methods to gain an understanding of microbial systems in the bioeconomy.

This dissertation presented ten novel platforms, created with nanofabrication techniques, for the study of microbial systems. These platforms are compatible with microscopic and spectroscopic techniques, and image data from the platforms was quantified with custom image processing algorithms. These platforms were demonstrated in studies of *Geobacter sulfurreducens* and *Pantoea* sp. YR343 as part of a greater effort to understand electroactive biofilms and rhizobacteria biofilms, respectively.

Investigation of *Pantoea* sp. YR343 biofilms with functionalized silane platforms revealed honeycomb biofilm morphology, enumerated with a custom image processing algorithm. This platform explored the biological questions on the effect of *Pantoea* sp. YR343 flagella on biofilm propagation and morphology. FliR, a flagella export protein, was found to have a substantial impact on cell attachment as the *Pantoea* sp. YR343  $\Delta fliR$  showed reduced surface area coverage compared to *Pantoea* sp. YR343 WT and altered biofilm morphology. Silane functionalization can be adapted to glass and combined with confocal laser scanning microscopy to assess how the *Pantoea* sp. YR343 flagella affects biofilm propagation and morphology. A fundamental understanding of rhizobacteria biofilms will contribute to the plant-microbe interface research effort. The *Pantoea* sp. YR343 biofilm investigation captures how nanofabrication techniques can be combined with conventional laboratory methods to elucidate the complexities of the rhizosphere and other microbial communities.

## LIST OF REFERENCES

Ali, M. A., Naveed, M., Mustafa, A., & Abbas, A. (2017). The Good, the Bad, and the Ugly of Rhizosphere Microbiome. In V. Kumar, M. Kumar, S. Sharma, & R. Prasad (Eds.), *Probiotics and Plant Health* (pp. 253-290). Singapore: Springer Singapore.

Almaguer-Flores, A., Silva-Bermudez, P., Galicia, R., & Rodil, S. E. (2015). Bacterial adhesion on amorphous and crystalline metal oxide coatings. *Materials Science and Engineering: C*, 57, 88-99.  
doi:<https://doi.org/10.1016/j.msec.2015.07.031>

Al-Shabib, N. A., Husain, F. M., Ahmed, F., Khan, R. A., Ahmad, I., Alsharaeh, E., . . . Aliev, G. (2016). Biogenic synthesis of Zinc oxide nanostructures from *Nigella sativa* seed: Prospective role as food packaging material inhibiting broad-spectrum quorum sensing and biofilm. *Scientific Reports*, 6, 36761.  
doi:10.1038/srep36761

Ammar, R., Paton, T. A., Torti, D., Shlien, A., & Bader, G. D. (2015). Long read nanopore sequencing for detection of HLA and CYP2D6 variants and haplotypes. *F1000Research*, 4, 17-17. doi:10.12688/f1000research.6037.2

An, Y. H., & Friedman, R. J. (1998). Concise review of mechanisms of bacterial adhesion to biomaterial surfaces. *J Biomed Mater Res*, 43(3), 338-348.  
doi:10.1002/(sici)1097-4636(199823)43:3<338::aid-jbm16>3.0.co;2-b

Asina, F. N. U., Brzonova, I., Kozliak, E., Kubátová, A., & Ji, Y. (2017). Microbial treatment of industrial lignin: Successes, problems and challenges. *Renewable and Sustainable Energy Reviews*, 77, 1179-1205.  
doi:<https://doi.org/10.1016/j.rser.2017.03.098>

Aufrecht, J. A., Ryan, J. M., Hasim, S., Allison, D. P., Nebenführ, A., Doktycz, M. J., & Retterer, S. T. (2017). Imaging the Root Hair Morphology of *Arabidopsis*

Seedlings in a Two-layer Microfluidic Platform. *JoVE*(126), e55971.

doi:doi:10.3791/55971

Aufrecht, J. A., Timm, C. M., Bible, A., Morrell-Falvey, J. L., Pelletier, D. A., Doktycz, M. J., & Retterer, S. T. (2018). Quantifying the Spatiotemporal Dynamics of Plant Root Colonization by Beneficial Bacteria in a Microfluidic Habitat. *Advanced Biosystems*, 2(6), 1800048. doi:10.1002/adbi.201800048

Azeredo, J., Azevedo, N. F., Briandet, R., Cerca, N., Coenye, T., Costa, A. R., . . . Sternberg, C. (2017). Critical review on biofilm methods. *Critical Reviews in Microbiology*, 43(3), 313-351. doi:10.1080/1040841X.2016.1208146

Babu, R. P., O'Connor, K., & Seeram, R. (2013). Current progress on bio-based polymers and their future trends. *Progress in Biomaterials*, 2(1), 8. doi:10.1186/2194-0517-2-8

Bendaoud, M., Vinogradov, E., Balashova, N. V., Kadouri, D. E., Kachlany, S. C., & Kaplan, J. B. (2011). Broad-spectrum biofilm inhibition by *Kingella kingae* exopolysaccharide. *Journal of Bacteriology*, 193(15), 3879. doi:10.1128/JB.00311-11

Bennett, R. R., Lee, C. K., De Anda, J., Nealson, K. H., Yildiz, F. H., O'Toole, G. A., . . . Golestanian, R. (2016). Species-dependent hydrodynamics of flagellum-tethered bacteria in early biofilm development. *Journal of The Royal Society Interface*, 13(115), 20150966. doi:10.1098/rsif.2015.0966

Berg, G. (2009). Plant–microbe interactions promoting plant growth and health: perspectives for controlled use of microorganisms in agriculture. *Applied Microbiology and Biotechnology*, 84(1), 11-18. doi:10.1007/s00253-009-2092-7

Berne, C., Ellison, C. K., Ducret, A., & Brun, Y. V. (2018). Bacterial adhesion at the single-cell level. *Nature Reviews Microbiology*, 16(10), 616-627. doi:10.1038/s41579-018-0057-5

Bible, A. N., Fletcher, S. J., Pelletier, D. A., Schadt, C. W., Jawdy, S. S., Weston, D. J., . . . Morrell-Falvey, J. L. (2016). A Carotenoid-Deficient Mutant in *Pantoea* sp. YR343, a Bacteria Isolated from the Rhizosphere of *Populus deltoides*, Is Defective in Root Colonization. *Frontiers in Microbiology*, 7(491).

doi:10.3389/fmicb.2016.00491

Bond, D. R., Strycharz-Glaven, S. M., Tender, L. M., & Torres, C. I. (2012). On electron transport through *Geobacter* biofilms. *ChemSusChem*, 5(6), 1099-1105.

doi:10.1002/cssc.201100748

Branda, S. S., Vik, S., Friedman, L., & Kolter, R. (2005). Biofilms: the matrix revisited. *Trends Microbiol*, 13(1), 20-26. doi:10.1016/j.tim.2004.11.006

Bridier, A., Dubois-Brissonnet, F., Boubetra, A., Thomas, V., & Briandet, R. (2010). The biofilm architecture of sixty opportunistic pathogens deciphered using a high throughput CLSM method. *Journal of Microbiological Methods*, 82(1), 64-70. doi:https://doi.org/10.1016/j.mimet.2010.04.006

Busalmen, J. P., & de Sánchez, S. R. (2001). Influence of pH and ionic strength on adhesion of a wild strain of *Pseudomonas* sp. to titanium. *Journal of Industrial Microbiology and Biotechnology*, 26(5), 303-308. doi:10.1038/sj.jim.7000133

Cai, W.-J., Hu, X., Huang, W.-J., Murrell, M. C., Lehrter, J. C., Lohrenz, S. E., . . . Gong, G.-C. (2011). Acidification of subsurface coastal waters enhanced by eutrophication. *Nature Geoscience*, 4(11), 766-770. doi:10.1038/geo1297

Cardullo, R. A. (2003). Fundamentals of Image Processing in Light Microscopy. In L. Wilson & P. Matsudaira (Eds.), *Methods in Cell Biology* (Vol. 72, pp. 217-242): Academic Press.

Carminati, A., & Vetterlein, D. (2013). Plasticity of rhizosphere hydraulic properties as a key for efficient utilization of scarce resources. *Annals of botany*, 112(2), 277-290. doi:10.1093/aob/mcs262



Chavant, P., Martinie, B., Meylheuc, T., Bellon-Fontaine, M.-N., & Hebraud, M. (2002). *Listeria monocytogenes* LO28: Surface Physicochemical Properties and Ability To Form Biofilms at Different Temperatures and Growth Phases. *Applied and Environmental Microbiology*, 68(2), 728. doi:10.1128/AEM.68.2.728-737.2002

Chen, Q., Chen, Y.-C., Zhang, Z., Wu, B., Coleman, R., & Fan, X. (2017). An integrated microwell array platform for cell lasing analysis. *Lab Chip*, 17(16), 2814-2820. doi:10.1039/C7LC00539C

Choudhry, P. (2016). High-Throughput Method for Automated Colony and Cell Counting by Digital Image Analysis Based on Edge Detection. *PLoS ONE*, 11(2), e0148469. doi:10.1371/journal.pone.0148469

Cologgi, D. L., Speers, A. M., Bullard, B. A., Kelly, S. D., & Reguera, G. (2014). Enhanced uranium immobilization and reduction by *Geobacter sulfurreducens* biofilms. *Appl Environ Microbiol*, 80(21), 6638-6646. doi:10.1128/aem.02289-14

Colvin, K. M., Irie, Y., Tart, C. S., Urbano, R., Whitney, J. C., Ryder, C., . . . Parsek, M. R. (2012). The Pel and Psl polysaccharides provide *Pseudomonas aeruginosa* structural redundancy within the biofilm matrix. *Environmental Microbiology*, 14(8), 1913-1928. doi:10.1111/j.1462-2920.2011.02657.x

Coppedè, N., Janni, M., Bettelli, M., Maida, C. L., Gentile, F., Villani, M., . . . Zappettini, A. (2017). An in vivo biosensing, biomimetic electrochemical transistor with applications in plant science and precision farming. *Scientific Reports*, 7(1), 16195. doi:10.1038/s41598-017-16217-4

Costerton, J. W., Lewandowski, Z., Caldwell, D. E., Korber, D. R., & Lappin-Scott, H. M. (1995). Microbial biofilms. *Annu Rev Microbiol*, 49, 711-745. doi:10.1146/annurev.mi.49.100195.003431

Dale, V. H., Kline, K. L., Parish, E. S., Cowie, A. L., Emory, R., Malmshiemer, R. W., . . . Wellisch, M. (2017). Status and prospects for renewable energy using wood pellets from the southeastern United States. *GCB Bioenergy*, 9(8), 1296-1305. doi:10.1111/gcbb.12445

Das, P., Mukherjee, S., & Sen, R. (2008). Antimicrobial potential of a lipopeptide biosurfactant derived from a marine *Bacillus circulans*. *J Appl Microbiol*, 104(6), 1675-1684. doi:10.1111/j.1365-2672.2007.03701.x

Das, T., Sehar, S., & Manefield, M. (2013). The roles of extracellular DNA in the structural integrity of extracellular polymeric substance and bacterial biofilm development. *Environmental Microbiology Reports*, 5(6), 778-786. doi:10.1111/1758-2229.12085

Davies, D. G., Parsek, M. R., Pearson, J. P., Iglewski, B. H., Costerton, J. W., & Greenberg, E. P. (1998). The involvement of cell-to-cell signals in the development of a bacterial biofilm. *Science*, 280(5361), 295-298. doi:10.1126/science.280.5361.295

Dheilly, A., Linossier, I., Darchen, A., Hadjiev, D., Corbel, C., & Alonso, V. (2008). Monitoring of microbial adhesion and biofilm growth using electrochemical impedancemetry. *Applied Microbiology and Biotechnology*, 79(1), 157-164. doi:10.1007/s00253-008-1404-7

Donlan, R. M. (2002). Biofilms: microbial life on surfaces. *Emerg Infect Dis*, 8(9), 881-890. doi:10.3201/eid0809.020063

Drigo, B., Kowalchuk, G. A., Knapp, B. A., Pijl, A. S., Boschker, H. T. S., & van Veen, J. A. (2013). Impacts of 3 years of elevated atmospheric CO<sub>2</sub> on rhizosphere carbon flow and microbial community dynamics. *Global Change Biology*, 19(2), 621-636. doi:10.1111/gcb.12045

- Engel, C., Schattenberg, F., Dohnt, K., Schröder, U., Müller, S., & Krull, R. (2019). Long-Term Behavior of Defined Mixed Cultures of *Geobacter sulfurreducens* and *Shewanella oneidensis* in Bioelectrochemical Systems. *Frontiers in Bioengineering and Biotechnology*, 7(60). doi:10.3389/fbioe.2019.00060
- Epstein, A. K., Hochbaum, A. I., Kim, P., & Aizenberg, J. (2011). Control of bacterial biofilm growth on surfaces by nanostructural mechanics and geometry. *Nanotechnology*, 22(49), 494007. doi:10.1088/0957-4484/22/49/494007
- Estenson, K., Hurst, G. B., Standaert, R. F., Bible, A. N., Garcia, D., Chourey, K., . . . Morrell-Falvey, J. L. (2018). Characterization of Indole-3-acetic Acid Biosynthesis and the Effects of This Phytohormone on the Proteome of the Plant-Associated Microbe *Pantoea* sp. YR343. *J Proteome Res*, 17(4), 1361-1374. doi:10.1021/acs.jproteome.7b00708
- Fish, K., Osborn, A. M., & Boxall, J. B. (2017). Biofilm structures (EPS and bacterial communities) in drinking water distribution systems are conditioned by hydraulics and influence discolouration. *Science of The Total Environment*, 593-594, 571-580. doi:https://doi.org/10.1016/j.scitotenv.2017.03.176
- Flemming, H.-C., & Wingender, J. (2010). The biofilm matrix. *Nature Reviews Microbiology*, 8(9), 623-633. doi:10.1038/nrmicro2415
- Fradinho, J. C., Oehmen, A., & Reis, M. A. M. (2019). Improving polyhydroxyalkanoates production in phototrophic mixed cultures by optimizing accumulator reactor operating conditions. *International Journal of Biological Macromolecules*, 126, 1085-1092. doi:https://doi.org/10.1016/j.ijbiomac.2018.12.270
- Friedlander, R. S., Vlamakis, H., Kim, P., Khan, M., Kolter, R., & Aizenberg, J. (2013). Bacterial flagella explore microscale hummocks and hollows to increase

adhesion. *Proceedings of the National Academy of Sciences*, 110(14), 5624-5629. doi:10.1073/pnas.1219662110

Friedlander, R. S., Vogel, N., & Aizenberg, J. (2015). Role of Flagella in Adhesion of *Escherichia coli* to Abiotic Surfaces. *Langmuir*, 31(22), 6137-6144. doi:10.1021/acs.langmuir.5b00815

Galbiati, M. (2016). Introduction to Self-Assembled Monolayers (pp. 45-81).

Garrett, T. R., Bhakoo, M., & Zhang, Z. (2008). Bacterial adhesion and biofilms on surfaces. *Progress in Natural Science*, 18(9), 1049-1056. doi:https://doi.org/10.1016/j.pnsc.2008.04.001

Gefen, O., Gabay, C., Mumcuoglu, M., Engel, G., & Balaban, N. Q. (2008). Single-cell protein induction dynamics reveals a period of vulnerability to antibiotics in persister bacteria. *Proc Natl Acad Sci U S A*, 105(16), 6145-6149. doi:10.1073/pnas.0711712105

Geissmann, Q. (2013). OpenCFU, a new free and open-source software to count cell colonies and other circular objects. *PLoS ONE*, 8(2), e54072. doi:10.1371/journal.pone.0054072

Gelfand, I., Sahajpal, R., Zhang, X., Izaurralde, R. C., Gross, K. L., & Robertson, G. P. (2013). Sustainable bioenergy production from marginal lands in the US Midwest. *Nature*, 493, 514. doi:10.1038/nature11811

Glass, N. R., Tjeung, R., Chan, P., Yeo, L. Y., & Friend, J. R. (2011). Organosilane deposition for microfluidic applications. *Biomicrofluidics*, 5(3), 36501-365017. doi:10.1063/1.3625605

Golden, J., Yates, M. D., Halsted, M., & Tender, L. (2018). Application of electrochemical surface plasmon resonance (ESPR) to the study of electroactive

microbial biofilms. *Physical Chemistry Chemical Physics*, 20(40), 25648-25656.  
doi:10.1039/C8CP03898H

Golden, J. P., Burden, D. K., Fears, K. P., Barlow, D. E., So, C. R., Burns, J., . . .  
Tender, L. M. (2016). Imaging Active Surface Processes in Barnacle Adhesive  
Interfaces. *Langmuir*, 32(2), 541-550. doi:10.1021/acs.langmuir.5b03286

Gottel, N. R., Castro, H. F., Kerley, M., Yang, Z., Pelletier, D. A., Podar, M., . . .  
Schadt, C. W. (2011). Distinct microbial communities within the endosphere and  
rhizosphere of *Populus deltoides* roots across contrasting soil types. *Appl  
Environ Microbiol*, 77(17), 5934-5944. doi:10.1128/aem.05255-11

Gottenbos, B., van der Mei, H. C., Klatter, F., Nieuwenhuis, P., & Busscher, H. J.  
(2002). In vitro and in vivo antimicrobial activity of covalently coupled quaternary  
ammonium silane coatings on silicone rubber. *Biomaterials*, 23(6), 1417-1423.  
doi:https://doi.org/10.1016/S0142-9612(01)00263-0

Gouda, S., Kerry, R. G., Das, G., Paramithiotis, S., Shin, H.-S., & Patra, J. K.  
(2018). Revitalization of plant growth promoting rhizobacteria for sustainable  
development in agriculture. *Microbiological Research*, 206, 131-140.  
doi:https://doi.org/10.1016/j.micres.2017.08.016

Guilbaud, M., Piveteau, P., Desvaux, M., Brisse, S., & Briandet, R. (2015).  
Exploring the diversity of *Listeria monocytogenes* biofilm architecture by high-  
throughput confocal laser scanning microscopy and the predominance of the  
honeycomb-like morphotype. *Applied and Environmental Microbiology*, 81(5),  
1813. doi:10.1128/AEM.03173-14

Guttenplan, S. B., & Kearns, D. B. (2013). Regulation of flagellar motility during  
biofilm formation. *FEMS Microbiology Reviews*, 37(6), 849-871.  
doi:10.1111/1574-6976.12018

Halsted, M., Wilmoth, J. L., Briggs, P. A., Hansen, R. R., Briggs, D. P., Timm, A. C., & Retterer, S. T. (2016). Development of transparent microwell arrays for optical monitoring and dissection of microbial communities. *Journal of Vacuum Science & Technology B*, 34(6), 06KI03. doi:10.1116/1.4962739

Hansen, R. R., Shubert, K. R., Morrell-Falvey, J. L., Lokitz, B. S., Doktycz, M. J., & Retterer, S. T. (2014). Microstructured block copolymer surfaces for control of microbe adhesion and aggregation. *Biosensors (Basel)*, 4(1), 63-75.  
doi:10.3390/bios4010063

Harimawan, A., Rajasekar, A., & Ting, Y.-P. (2011). Bacteria attachment to surfaces – AFM force spectroscopy and physicochemical analyses. *Journal of Colloid and Interface Science*, 364(1), 213-218.  
doi:https://doi.org/10.1016/j.jcis.2011.08.021

Hebishima, T., Matsumoto, Y., Watanabe, G., Soma, G.-i., Kohchi, C., Taya, K., . . . Hirota, Y. (2011). Oral Administration of Immunopotentiator from *Pantoea agglomerans* 1 (IP-PA1) Improves the Survival of B16 Melanoma-Inoculated Model Mice. *Experimental Animals*, 60(2), 101-109. doi:10.1538/expanim.60.101

Hecht, V. L., Temperton, V. M., Nagel, K. A., Rascher, U., & Postma, J. A. (2016). Sowing Density: A Neglected Factor Fundamentally Affecting Root Distribution and Biomass Allocation of Field Grown Spring Barley (*Hordeum Vulgare* L.). *Frontiers in plant science*, 7, 944-944. doi:10.3389/fpls.2016.00944

Helmus, R. A., Liermann, L. J., Brantley, S. L., & Tien, M. (2012). Growth advantage in stationary-phase (GASP) phenotype in long-term survival strains of *Geobacter sulfurreducens*. *FEMS Microbiology Ecology*, 79(1), 218-228.  
doi:10.1111/j.1574-6941.2011.01211.x

Herrera, C. M., Koutsoudis, M. D., Wang, X., & von Bodman, S. B. (2008). *Pantoea stewartii* subsp. *stewartii* exhibits surface motility, which is a critical

aspect of Stewart's wilt disease development on maize. *Mol Plant Microbe Interact*, 21(10), 1359-1370. doi:10.1094/mpmi-21-10-1359

Heydorn, A., Nielsen, A. T., Hentzer, M., Sternberg, C., Givskov, M., Ersbøll, B. K., & Molin, S. (2000). Quantification of biofilm structures by the novel computer program comstat. *Microbiology*, 146(10), 2395-2407. doi:https://doi.org/10.1099/00221287-146-10-2395

Hlawacek, G., Veligura, V., Gastel, R. v., & Poelsema, B. (2014). Helium ion microscopy. *Journal of Vacuum Science & Technology B*, 32(2), 020801. doi:10.1116/1.4863676

Hol, F. J. H., & Dekker, C. (2014). Zooming in to see the bigger picture: Microfluidic and nanofabrication tools to study bacteria. *Science*, 346(6208), 1251821. doi:10.1126/science.1251821

Holman, H.-Y. N., Miles, R., Hao, Z., Wozel, E., Anderson, L. M., & Yang, H. (2009). Real-Time Chemical Imaging of Bacterial Activity in Biofilms Using Open-Channel Microfluidics and Synchrotron FTIR Spectromicroscopy. *Analytical Chemistry*, 81(20), 8564-8570. doi:10.1021/ac9015424

Hu, J., & Bohn, P. W. (2017). Optical Biosensing of Bacteria and Bacterial Communities. *Journal of Analysis and Testing*, 1(1), 4. doi:10.1007/s41664-017-0002-z

Ingham, C. J., Sprenkels, A., Bomer, J., Molenaar, D., van den Berg, A., van Hylckama Vlieg, J. E. T., & de Vos, W. M. (2007). The micro-Petri dish, a million-well growth chip for the culture and high-throughput screening of microorganisms. *Proceedings of the National Academy of Sciences*, 104(46), 18217-18222. doi:10.1073/pnas.0701693104

- Jain, S., Adeyeye, A. O., Chan, S. Y., & Boothroyd, C. B. (2004). Interface properties of iron oxide films. *Journal of Physics D: Applied Physics*, 37(19), 2720-2725. doi:10.1088/0022-3727/37/19/016
- Jakubovics, N. S., Shields, R. C., Rajarajan, N., & Burgess, J. G. (2013). Life after death: the critical role of extracellular DNA in microbial biofilms. *Lett Appl Microbiol*, 57(6), 467-475. doi:10.1111/lam.12134
- Jiang, X., Hu, J., Fitzgerald, L. A., Biffinger, J. C., Xie, P., Ringeisen, B. R., & Lieber, C. M. (2010). Probing electron transfer mechanisms in *Shewanella oneidensis* MR-1 using a nanoelectrode platform and single-cell imaging. *Proceedings of the National Academy of Sciences*, 107(39), 16806-16810. doi:10.1073/pnas.1011699107
- Jiang, X., Hu, J., Petersen, E. R., Fitzgerald, L. A., Jackan, C. S., Lieber, A. M., . . . Biffinger, J. C. (2013). Probing single- to multi-cell level charge transport in *Geobacter sulfurreducens* DL-1. *Nature Communications*, 4(1), 2751. doi:10.1038/ncomms3751
- Karakoy, M., Gultepe, E., Pandey, S., Khashab, M. A., & Gracias, D. H. (2014). Silane surface modification for improved bioadhesion of esophageal stents. *Applied surface science*, 311, 684-689. doi:10.1016/j.apsusc.2014.05.136
- Kearns, D. B. (2010). A field guide to bacterial swarming motility. *Nature Reviews Microbiology*, 8(9), 634-644. doi:10.1038/nrmicro2405
- Kim, J., Park, H. D., & Chung, S. (2012). Microfluidic approaches to bacterial biofilm formation. *Molecules (Basel, Switzerland)*, 17(8), 9818-9834. doi:10.3390/molecules17089818
- Kocot, A. M., & Olszewska, M. A. (2017). Biofilm formation and microscopic analysis of biofilms formed by *Listeria monocytogenes* in a food processing context. *LWT*, 84, 47-57. doi:https://doi.org/10.1016/j.lwt.2017.05.042



Kumar, S. V., Taylor, G., Hasim, S., Collier, C. P., Farmer, A. T., Campagna, S. R., . . . Morrell-Falvey, J. (2019). Loss of carotenoids from membranes of *Pantoea* sp. YR343 results in altered lipid composition and changes in membrane biophysical properties. *Biochim Biophys Acta Biomembr*, 1861(7), 1338-1345. doi:10.1016/j.bbamem.2019.05.009

Lebedev, N., Strycharz-Glaven, S. M., & Tender, L. M. (2014). High Resolution AFM and Single-Cell Resonance Raman Spectroscopy of *Geobacter sulfurreducens* Biofilms Early in Growth. *Frontiers in Energy Research*, 2(34). doi:10.3389/fenrg.2014.00034

Li, B., & Logan, B. E. (2004). Bacterial adhesion to glass and metal-oxide surfaces. *Colloids and Surfaces B: Biointerfaces*, 36(2), 81-90. doi:https://doi.org/10.1016/j.colsurfb.2004.05.006

Lindner, A. B., Madden, R., Demarez, A., Stewart, E. J., & Taddei, F. (2008). Asymmetric segregation of protein aggregates is associated with cellular aging and rejuvenation. *Proc Natl Acad Sci U S A*, 105(8), 3076-3081. doi:10.1073/pnas.0708931105

Little, A. E. F., Robinson, C. J., Peterson, S. B., Raffa, K. E., & Handelsman, J. (2008). Rules of Engagement: Interspecies Interactions that Regulate Microbial Communities *Annual Review of Microbiology* (Vol. 62, pp. 375-401).

Liu, Y., & Bond, D. R. (2012). Long-distance electron transfer by *G. sulfurreducens* biofilms results in accumulation of reduced c-type cytochromes. *ChemSusChem*, 5(6), 1047-1053. doi:10.1002/cssc.201100734

Liu, Y., Kim, H., Franklin, R. R., & Bond, D. R. (2011). Linking spectral and electrochemical analysis to monitor c-type cytochrome redox status in living *Geobacter sulfurreducens* biofilms. *ChemPhysChem*, 12(12), 2235-2241. doi:10.1002/cphc.201100246

Ljosa, V., & Carpenter, A. E. (2009). Introduction to the quantitative analysis of two-dimensional fluorescence microscopy images for cell-based screening. *PLoS Comput Biol*, 5(12), e1000603. doi:10.1371/journal.pcbi.1000603

Logan, B. E. (2005). Simultaneous wastewater treatment and biological electricity generation. *Water Sci Technol*, 52(1-2), 31-37.

Logan, B. E., & Regan, J. M. (2006). Microbial Fuel Cells—Challenges and Applications. *Environ Sci Technol*, 40(17), 5172-5180. doi:10.1021/es0627592

Long, Z., Nugent, E., Javer, A., Cicuta, P., Sclavi, B., Cosentino Lagomarsino, M., & Dorfman, K. D. (2013). Microfluidic chemostat for measuring single cell dynamics in bacteria. *Lab Chip*, 13(5), 947-954. doi:10.1039/c2lc41196b

Lorite, G. S., Janissen, R., Clerici, J. H., Rodrigues, C. M., Tomaz, J. P., Mizaikoff, B., . . . Cotta, M. A. (2013). Surface Physicochemical Properties at the Micro and Nano Length Scales: Role on Bacterial Adhesion and *Xylella fastidiosa* Biofilm Development. *PLoS ONE*, 8(9), e75247. doi:10.1371/journal.pone.0075247

Lovley, D. R. (2006). Bug juice: harvesting electricity with microorganisms. *Nature Reviews Microbiology*, 4(7), 497-508. doi:10.1038/nrmicro1442

Lovley, D. R. (2011). Live wires: direct extracellular electron exchange for bioenergy and the bioremediation of energy-related contamination. *Energy & Environmental Science*, 4(12), 4896-4906. doi:10.1039/C1EE02229F

Lovley, D. R. (2012). Electromicrobiology. *Annual Review of Microbiology*, 66(1), 391-409. doi:10.1146/annurev-micro-092611-150104

Lovley, D. R., & Nevin, K. P. (2013). Electrobiocommodities: powering microbial production of fuels and commodity chemicals from carbon dioxide with electricity.

Current Opinion in Biotechnology, 24(3), 385-390.

doi:<https://doi.org/10.1016/j.copbio.2013.02.012>

Lugtenberg, B., & Kamilova, F. (2009). Plant-growth-promoting rhizobacteria.

Annu Rev Microbiol, 63, 541-556. doi:10.1146/annurev.micro.62.081307.162918

Mai, T. L., & Conner, D. E. (2007). Effect of temperature and growth media on the attachment of *Listeria monocytogenes* to stainless steel. Int J Food Microbiol, 120(3), 282-286. doi:10.1016/j.ijfoodmicro.2007.09.006

Malvankar, N. S., Vargas, M., Nevin, K., Tremblay, P.-L., Evans-Lutterodt, K., Nykypanchuk, D., . . . Lovley, D. R. (2015). Structural Basis for Metallic-Like Conductivity in Microbial Nanowires. mBio, 6(2), e00084-00015.

doi:10.1128/mBio.00084-15

Malvankar, N. S., Vargas, M., Nevin, K. P., Franks, A. E., Leang, C., Kim, B.-C., . . . Lovley, D. R. (2011). Tunable metallic-like conductivity in microbial nanowire networks. Nat Nanotechnol, 6(9), 573-579. doi:10.1038/nnano.2011.119

Maroni, P., Montes Ruiz-Cabello, F. J., Cardoso, C., & Tiraferri, A. (2015).

Adsorbed Mass of Polymers on Self-Assembled Monolayers: Effect of Surface Chemistry and Polymer Charge. Langmuir, 31(22), 6045-6054.

doi:10.1021/acs.langmuir.5b01103

Marsh, E. J., Luo, H., & Wang, H. (2003). A three-tiered approach to differentiate *Listeria monocytogenes* biofilm-forming abilities. FEMS Microbiol Lett, 228(2), 203-210. doi:10.1016/s0378-1097(03)00752-3

Massalha, H., Korenblum, E., Malitsky, S., Shapiro, O. H., & Aharoni, A. (2017).

Live imaging of root–bacteria interactions in a microfluidics setup. Proceedings of the National Academy of Sciences, 114(17), 4549.

doi:10.1073/pnas.1618584114

Merritt, J. H., Kadouri, D. E., & O'Toole, G. A. (2005). Growing and analyzing static biofilms. *Current protocols in microbiology*, Chapter 1, Unit-1B.1.  
doi:10.1002/9780471729259.mc01b01s00

Miles, C. (2019). The combine will tell the truth: On precision agriculture and algorithmic rationality. *Big Data & Society*, 6(1), 2053951719849444.  
doi:10.1177/2053951719849444

Millet, L. J., Aufrecht, J., Labbé, J., Uehling, J., Vilgalys, R., Estes, M. L., . . . Retterer, S. T. (2019). Increasing access to microfluidics for studying fungi and other branched biological structures. *Fungal Biology and Biotechnology*, 6(1), 8.  
doi:10.1186/s40694-019-0071-z

Mitchell, S. A., Poulsson, A. H., Davidson, M. R., Emmison, N., Shard, A. G., & Bradley, R. H. (2004). Cellular attachment and spatial control of cells using micro-patterned ultra-violet/ozone treatment in serum enriched media. *Biomaterials*, 25(18), 4079-4086. doi:10.1016/j.biomaterials.2003.11.010

Mosquera-Fernández, M., Rodríguez-López, P., Cabo, M. L., & Balsa-Canto, E. (2014). Numerical spatio-temporal characterization of *Listeria monocytogenes* biofilms. *International Journal of Food Microbiology*, 182-183, 26-36.  
doi:https://doi.org/10.1016/j.ijfoodmicro.2014.05.005

Mozes, N., Marchal, F., Hermesse, M. P., Van Haecht, J. L., Reuliaux, L., Leonard, A. J., & Rouxhet, P. G. (1987). Immobilization of microorganisms by adhesion: Interplay of electrostatic and nonelectrostatic interactions. *Biotechnol Bioeng*, 30(3), 439-450. doi:10.1002/bit.260300315

Mueller, R. F., Characklis, W. G., Jones, W. L., & Sears, J. T. (1992). Characterization of initial events in bacterial surface colonization by two *Pseudomonas* species using image analysis. *Biotechnol Bioeng*, 39(11), 1161-1170. doi:10.1002/bit.260391113

- Mukherjee, A., Walker, J., Weyant, K. B., & Schroeder, C. M. (2013). Characterization of flavin-based fluorescent proteins: an emerging class of fluorescent reporters. *PLoS ONE*, 8(5), e64753. doi:10.1371/journal.pone.0064753
- Mukherjee, A. K., & Das, K. (2010). Microbial Surfactants and Their Potential Applications: An Overview. In R. Sen (Ed.), *Biosurfactants* (pp. 54-64). New York, NY: Springer New York.
- Murphy, D. B., & Davidson, M. W. (2012). *Fundamentals of Light Microscopy and Electronic Imaging*. Somerset, UNITED STATES: John Wiley & Sons, Incorporated.
- Murphy, K., Hansen, R., Nath, S., Retterer, S., Collier, P., Boreyko, J., . . . Team, C. M. S. (2015). Spatial Control of Condensation using Chemical Micropatterns. Paper presented at the APS Division of Fluid Dynamics Meeting Abstracts. <https://ui.adsabs.harvard.edu/abs/2015APS..DFDE36002M>
- Nagarajan, H., Embree, M., Rotaru, A.-E., Shrestha, P. M., Feist, A. M., Palsson, B. Ø., . . . Zengler, K. (2013). Characterization and modelling of interspecies electron transfer mechanisms and microbial community dynamics of a syntrophic association. *Nature Communications*, 4(1), 2809. doi:10.1038/ncomms3809
- Nakamura, S., & Minamino, T. (2019). Flagella-Driven Motility of Bacteria. *Biomolecules*, 9(7), 279. doi:10.3390/biom9070279
- Nakata, K., Inagawa, H., & Soma, G. (2011). Lipopolysaccharide IP-PA1 from *Pantoea agglomerans* prevents suppression of macrophage function in stress-induced diseases. *Anticancer Res*, 31(7), 2437-2440.
- Norman, T. M., Lord, N. D., Paulsson, J., & Losick, R. (2013). Memory and modularity in cell-fate decision making. *Nature*, 503(7477), 481-486. doi:10.1038/nature12804

- Okshevsky, M., & Meyer, R. L. (2015). The role of extracellular DNA in the establishment, maintenance and perpetuation of bacterial biofilms. *Critical Reviews in Microbiology*, 41(3), 341-352. doi:10.3109/1040841X.2013.841639
- Palmer, J., Flint, S., & Brooks, J. (2007). Bacterial cell attachment, the beginning of a biofilm. *Journal of Industrial Microbiology & Biotechnology*, 34(9), 577-588. doi:10.1007/s10295-007-0234-4
- Petrova, O. E., & Sauer, K. (2012). Sticky Situations: Key Components That Control Bacterial Surface Attachment. *Journal of Bacteriology*, 194(10), 2413-2425. doi:10.1128/jb.00003-12
- Pierpaoli, E., Carli, G., Pignatti, E., & Canavari, M. (2013). Drivers of Precision Agriculture Technologies Adoption: A Literature Review. *Procedia Technology*, 8, 61-69. doi:https://doi.org/10.1016/j.protcy.2013.11.010
- Pii, Y., Borruso, L., Brusetti, L., Crecchio, C., Cesco, S., & Mimmo, T. (2016). The interaction between iron nutrition, plant species and soil type shapes the rhizosphere microbiome. *Plant Physiology and Biochemistry*, 99, 39-48. doi:https://doi.org/10.1016/j.plaphy.2015.12.002
- Piliarik, M., Vaisocherová, H., & Homola, J. (2009). Surface Plasmon Resonance Biosensing. In A. Rasooly & K. E. Herold (Eds.), *Biosensors and Biodetection* (pp. 65-88). Totowa, NJ: Humana Press.
- Polisetti, S., Bible, A. N., Morrell-Falvey, J. L., & Bohn, P. W. (2016). Raman chemical imaging of the rhizosphere bacterium *Pantoea* sp. YR343 and its co-culture with *Arabidopsis thaliana*. *Analyst*, 141(7), 2175-2182. doi:10.1039/C6AN00080K
- Prasad, R., Bhattacharyya, A., & Nguyen, Q. D. (2017). Nanotechnology in Sustainable Agriculture: Recent Developments, Challenges, and Perspectives. *Frontiers in Microbiology*, 8, 1014-1014. doi:10.3389/fmicb.2017.01014

Pringle, J. H., & Fletcher, M. (1983). Influence of substratum wettability on attachment of freshwater bacteria to solid surfaces. *Applied and Environmental Microbiology*, 45(3), 811-817.

Privett, B. J., Youn, J., Hong, S. A., Lee, J., Han, J., Shin, J. H., & Schoenfish, M. H. (2011). Antibacterial Fluorinated Silica Colloid Superhydrophobic Surfaces. *Langmuir*, 27(15), 9597-9601. doi:10.1021/la201801e

Puckett, S. D., Taylor, E., Raimondo, T., & Webster, T. J. (2010). The relationship between the nanostructure of titanium surfaces and bacterial attachment. *Biomaterials*, 31(4), 706-713. doi:10.1016/j.biomaterials.2009.09.081

Quinn, L. D., Straker, K. C., Guo, J., Kim, S., Thapa, S., Kling, G., . . . Voigt, T. B. (2015). Stress-Tolerant Feedstocks for Sustainable Bioenergy Production on Marginal Land. *BioEnergy Research*, 8(3), 1081-1100. doi:10.1007/s12155-014-9557-y

Raaijmakers, J. M., Paulitz, T. C., Steinberg, C., Alabouvette, C., & Moënne-Loccoz, Y. (2009). The rhizosphere: a playground and battlefield for soilborne pathogens and beneficial microorganisms. *Plant and Soil*, 321(1), 341-361. doi:10.1007/s11104-008-9568-6

Rabbi, S. M. F., Tighe, M. K., Flavel, R. J., Kaiser, B. N., Guppy, C. N., Zhang, X., & Young, I. M. (2018). Plant roots redesign the rhizosphere to alter the three-dimensional physical architecture and water dynamics. *New Phytologist*, 219(2), 542-550. doi:10.1111/nph.15213

Ramey, B. E., Koutsoudis, M., Bodman, S. B. v., & Fuqua, C. (2004). Biofilm formation in plant-microbe associations. *Current Opinion in Microbiology*, 7(6), 602-609. doi:https://doi.org/10.1016/j.mib.2004.10.014

Reguera, G. (2018). Microbial nanowires and electroactive biofilms. *FEMS Microbiology Ecology*, 94(7). doi:10.1093/femsec/fiy086

Reguera, G., McCarthy, K. D., Mehta, T., Nicoll, J. S., Tuominen, M. T., & Lovley, D. R. (2005). Extracellular electron transfer via microbial nanowires. *Nature*, 435(7045), 1098-1101. doi:10.1038/nature03661

Retterer, S. T., Morrell-Falvey, J. L., & Doktycz, M. J. (2018). Nano-Enabled Approaches to Chemical Imaging in Biosystems. *Annual Review of Analytical Chemistry*, 11(1), 351-373. doi:10.1146/annurev-anchem-061417-125635

Rogers, J. N., Stokes, B., Dunn, J., Cai, H., Wu, M., Haq, Z., & Baumes, H. (2017). An assessment of the potential products and economic and environmental impacts resulting from a billion ton bioeconomy. *Biofuels, Bioproducts and Biorefining*, 11(1), 110-128. doi:10.1002/bbb.1728

Rollefson, J. B., Stephen, C. S., Tien, M., & Bond, D. R. (2011). Identification of an extracellular polysaccharide network essential for cytochrome anchoring and biofilm formation in *Geobacter sulfurreducens*. *J Bacteriol*, 193(5), 1023-1033. doi:10.1128/jb.01092-10

Sánchez-Cañizares, C., Jorrín, B., Poole, P. S., & Tkacz, A. (2017). Understanding the holobiont: the interdependence of plants and their microbiome. *Current Opinion in Microbiology*, 38, 188-196. doi:https://doi.org/10.1016/j.mib.2017.07.001

Sannigrahi, P., Ragauskas, A. J., & Tuskan, G. A. (2010). Poplar as a feedstock for biofuels: A review of compositional characteristics. *Biofuels, Bioproducts and Biorefining*, 4(2), 209-226. doi:10.1002/bbb.206

Schultz, D., Onuchic, J. N., & Ben-Jacob, E. (2012). Turning death into creative force during biofilm engineering. *Proceedings of the National Academy of Sciences*, 109(46), 18633-18634. doi:10.1073/pnas.1215227109

Serra, D. O., Richter, A. M., Klauck, G., Mika, F., & Hengge, R. (2013). Microanatomy at Cellular Resolution and Spatial Order of Physiological



Differentiation in a Bacterial Biofilm. *mBio*, 4(2), e00103-00113.

doi:10.1128/mBio.00103-13

Shakya, M., Gottel, N., Castro, H., Yang, Z. K., Gunter, L., Labbe, J., . . . Schadt, C. W. (2013). A multifactor analysis of fungal and bacterial community structure in the root microbiome of mature *Populus deltoides* trees. *PLoS ONE*, 8(10), e76382. doi:10.1371/journal.pone.0076382

Shang, Y., Hasan, M. K., Ahammed, G. J., Li, M., Yin, H., & Zhou, J. (2019). Applications of Nanotechnology in Plant Growth and Crop Protection: A Review. *Molecules* (Basel, Switzerland), 24(14), 2558. doi:10.3390/molecules24142558

Shi, L., Dong, H., Reguera, G., Beyenal, H., Lu, A., Liu, J., . . . Fredrickson, J. K. (2016). Extracellular electron transfer mechanisms between microorganisms and minerals. *Nature Reviews Microbiology*, 14(10), 651-662. doi:10.1038/nrmicro.2016.93

Sieuwert, S., De Bok, F. A. M., Mols, E., De Vos, W. M., & Van Hylckama Vlieg, J. E. T. (2008). A simple and fast method for determining colony forming units. *Letters in Applied Microbiology*, 47(4), 275-278. doi:10.1111/j.1472-765X.2008.02417.x

Silhavy, T. J., Kahne, D., & Walker, S. (2010). The bacterial cell envelope. *Cold Spring Harb Perspect Biol*, 2(5), a000414. doi:10.1101/cshperspect.a000414

Snider, R. M., Strycharz-Glaven, S. M., Tsoi, S. D., Erickson, J. S., & Tender, L. M. (2012). Long-range electron transport in *Geobacter sulfurreducens* biofilms is redox gradient-driven. *Proceedings of the National Academy of Sciences*, 109(38), 15467. doi:10.1073/pnas.1209829109

Song, F., Brasch, M. E., Wang, H., Henderson, J. H., Sauer, K., & Ren, D. (2017). How Bacteria Respond to Material Stiffness during Attachment: A Role of

*Escherichia coli* Flagellar Motility. *ACS Applied Materials & Interfaces*, 9(27), 22176-22184. doi:10.1021/acsami.7b04757

Song, F., Koo, H., & Ren, D. (2015). Effects of Material Properties on Bacterial Adhesion and Biofilm Formation. *Journal of Dental Research*, 94(8), 1027-1034. doi:10.1177/0022034515587690

Steidl, R. J., Lampa-Pastirk, S., & Reguera, G. (2016). Mechanistic stratification in electroactive biofilms of *Geobacter sulfurreducens* mediated by pilus nanowires. *Nature Communications*, 7(1), 12217. doi:10.1038/ncomms12217

Steinberg, N., & Kolodkin-Gal, I. (2015). The Matrix Reloaded: Probing the Extracellular Matrix Synchronizes Bacterial Communities. *Journal of Bacteriology*, 197(13), 2092-2103. doi:10.1128/JB.02516-14

Stewart, E. J., Madden, R., Paul, G., & Taddei, F. (2005). Aging and Death in an Organism That Reproduces by Morphologically Symmetric Division. *PLOS Biology*, 3(2), e45. doi:10.1371/journal.pbio.0030045

Strycharz, S. M., Malanoski, A. P., Snider, R. M., Yi, H., Lovley, D. R., & Tender, L. M. (2011). Application of cyclic voltammetry to investigate enhanced catalytic current generation by biofilm-modified anodes of *Geobacter sulfurreducens* strain DL1 vs. variant strain KN400. *Energy & Environmental Science*, 4(3), 896-913. doi:10.1039/C0EE00260G

Strycharz-Glaven, S. M., & Tender, L. M. (2012). Study of the Mechanism of Catalytic Activity of *G. Sulfurreducens* Biofilm Anodes during Biofilm Growth. *ChemSusChem*, 5(6), 1106-1118. doi:10.1002/cssc.201100737

Sugimura, H., Hozumi, A., Kameyama, T., & Takai, O. (2002). Organosilane self-assembled monolayers formed at the vapour/solid interface. *Surface and Interface Analysis*, 34(1), 550-554. doi:10.1002/sia.1358

Sutherland, I. W. (2001). Biofilm exopolysaccharides: a strong and sticky framework. *Microbiology*, 147(1), 3-9. doi:<https://doi.org/10.1099/00221287-147-1-3>

Takhistov, P., & George, B. (2004). Linearized kinetic model of *Listeria monocytogenes* biofilm growth. *Bioprocess Biosyst Eng*, 26(4), 259-270. doi:10.1007/s00449-004-0357-1

Takhistov, P., & George, B. (2005). Early events and pattern formation in *Listeria monocytogenes* biofilms. *Biofilms*, 1(4), 351-359. doi:10.1017/S1479050504001504

Tan, C. P., Cipriany, B. R., Lin, D. M., & Craighead, H. G. (2010). Nanoscale resolution, multicomponent biomolecular arrays generated by aligned printing with parylene peel-off. *Nano Lett*, 10(2), 719-725. doi:10.1021/nl903968s

Tan, C. P., & Craighead, H. G. (2010). Surface Engineering and Patterning Using Parylene for Biological Applications. *Materials*, 3(3), 1803-1832. doi:10.3390/ma3031803

Tan, C. P., Seo, B. R., Brooks, D. J., Chandler, E. M., Craighead, H. G., & Fischbach, C. (2009). Parylene peel-off arrays to probe the role of cell-cell interactions in tumour angiogenesis. *Integr Biol (Camb)*, 1(10), 587-594. doi:10.1039/b908036h

Tang, Y., Zeng, X., & Liang, J. (2010). Surface Plasmon Resonance: An Introduction to a Surface Spectroscopy Technique. *Journal of chemical education*, 87(7), 742-746. doi:10.1021/ed100186y

Timm, A. C., Halsted, M. C., Wilmoth, J. L., & Retterer, S. T. (2017). Assembly and Tracking of Microbial Community Development within a Microwell Array Platform. *J Vis Exp*(124). doi:10.3791/55701

Timm, C. M., Hansen, R. R., Doktycz, M. J., Retterer, S. T., & Pelletier, D. A. (2015). Microstencils to generate defined, multi-species patterns of bacteria. *Biomicrofluidics*, 9(6), 064103. doi:10.1063/1.4935938

Timm, C. M., Pelletier, D. A., Jawdy, S. S., Gunter, L. E., Henning, J. A., Engle, N., . . . Weston, D. J. (2016). Two Poplar-Associated Bacterial Isolates Induce Additive Favorable Responses in a Constructed Plant-Microbiome System. *Frontiers in plant science*, 7(497). doi:10.3389/fpls.2016.00497

Tomaras, A. P., Dorsey, C. W., Edelmann, R. E., & Actis, L. A. (2003). Attachment to and biofilm formation on abiotic surfaces by *Acinetobacter baumannii*: involvement of a novel chaperone-usher pili assembly system. *Microbiology*, 149(Pt 12), 3473-3484. doi:10.1099/mic.0.26541-0

Tresse, O., Lebreton, V., Benezech, T., & Faille, C. (2006). Comparative evaluation of adhesion, surface properties, and surface protein composition of *Listeria monocytogenes* strains after cultivation at constant pH of 5 and 7. *J Appl Microbiol*, 101(1), 53-62. doi:10.1111/j.1365-2672.2006.02968.x

Truong, V. K., Lapovok, R., Estrin, Y. S., Rundell, S., Wang, J. Y., Fluke, C. J., . . . Ivanova, E. P. (2010). The influence of nano-scale surface roughness on bacterial adhesion to ultrafine-grained titanium. *Biomaterials*, 31(13), 3674-3683. doi:10.1016/j.biomaterials.2010.01.071

Tuson, H. H., & Weibel, D. B. (2013). Bacteria–surface interactions. *Soft Matter*, 9(17), 4368-4380. doi:10.1039/C3SM27705D

Vaisocherova, H., Zhang, Z., Yang, W., Cao, Z., Cheng, G., Taylor, A. D., . . . Jiang, S. (2009). Functionalizable surface platform with reduced nonspecific protein adsorption from full blood plasma--material selection and protein immobilization optimization. *Biosens Bioelectron*, 24(7), 1924-1930. doi:10.1016/j.bios.2008.09.035

van der Vlies, A. J., Barua, N., Nieves-Otero, P. A., Platt, T. G., & Hansen, R. R. (2019). On Demand Release and Retrieval of Bacteria from Microwell Arrays Using Photodegradable Hydrogel Membranes. *ACS Applied Bio Materials*, 2(1), 266-276. doi:10.1021/acsabm.8b00592

van Schie, P. M., & Fletcher, M. (1999). Adhesion of Biodegradative Anaerobic Bacteria to Solid Surfaces. *Applied and Environmental Microbiology*, 65(11), 5082-5088.

Verma, O. P., Sharma, R., & Kumar, D. (2012). Binarization based Image Edge Detection using Bacterial Foraging Algorithm. *Procedia Technology*, 6, 315-323. doi:https://doi.org/10.1016/j.protcy.2012.10.038

Walterson, A. M., & Stavrinos, J. (2015). *Pantoea*: insights into a highly versatile and diverse genus within the Enterobacteriaceae. *FEMS Microbiology Reviews*, 39(6), 968-984. doi:10.1093/femsre/fuv027

Wang, H., Sodagari, M., Chen, Y., He, X., Newby, B.-m. Z., & Ju, L.-K. (2011). Initial bacterial attachment in slow flowing systems: Effects of cell and substrate surface properties. *Colloids and Surfaces B: Biointerfaces*, 87(2), 415-422. doi:https://doi.org/10.1016/j.colsurfb.2011.05.053

Wang, H., Sodagari, M., Ju, L.-K., & Zhang Newby, B.-m. (2013). Effects of shear on initial bacterial attachment in slow flowing systems. *Colloids and Surfaces B: Biointerfaces*, 109, 32-39. doi:https://doi.org/10.1016/j.colsurfb.2013.03.016

Wang, L., Nie, Y., Tang, Y.-Q., Song, X.-M., Cao, K., Sun, L.-Z., . . . Wu, X.-L. (2016). Diverse Bacteria with Lignin Degrading Potentials Isolated from Two Ranks of Coal. *Frontiers in Microbiology*, 7, 1428-1428. doi:10.3389/fmicb.2016.01428

- Wang, S., Huang, X., Shan, X., Foley, K. J., & Tao, N. (2010). Electrochemical Surface Plasmon Resonance: Basic Formalism and Experimental Validation. *Analytical Chemistry*, 82(3), 935-941. doi:10.1021/ac902178f
- White III, R. A., Callister, S. J., Moore, R. J., Baker, E. S., & Jansson, J. K. (2016). The past, present and future of microbiome analyses. *Nature Protocols*, 11, 2049. doi:10.1038/nprot.2016.148
- Wilmoth, J. L., Doak, P. W., Timm, A., Halsted, M., Anderson, J. D., Ginovart, M., . . . Fuentes-Cabrera, M. (2018). A Microfluidics and Agent-Based Modeling Framework for Investigating Spatial Organization in Bacterial Colonies: The Case of *Pseudomonas Aeruginosa* and H1-Type VI Secretion Interactions. *Front Microbiol*, 9, 33. doi:10.3389/fmicb.2018.00033
- Wilpiseski, R. L., Aufrecht, J. A., Retterer, S. T., Sullivan, M. B., Graham, D. E., Pierce, E. M., . . . Elias, D. A. (2019). Soil Aggregate Microbial Communities: Towards Understanding Microbiome Interactions at Biologically Relevant Scales. *Applied and Environmental Microbiology*, 85(14), e00324-00319. doi:10.1128/aem.00324-19
- Xie, X., Criddle, C., & Cui, Y. (2015). Design and fabrication of bioelectrodes for microbial bioelectrochemical systems. *Energy & Environmental Science*, 8(12), 3418-3441. doi:10.1039/C5EE01862E
- Yang, X., Beyenal, H., Harkin, G., & Lewandowski, Z. (2001). Evaluation of biofilm image thresholding methods. *Water Research*, 35(5), 1149-1158. doi:https://doi.org/10.1016/S0043-1354(00)00361-4
- Zeng, S., Baillargeat, D., Ho, H.-P., & Yong, K.-T. (2014). Nanomaterials enhanced surface plasmon resonance for biological and chemical sensing applications. *Chemical Society Reviews*, 43, 3426-3452. doi:10.1039/c3cs60479a

Zeppenfeld, T., Balkenhol, N., Kóvacs, K., & Carminati, A. (2017). Rhizosphere hydrophobicity: A positive trait in the competition for water. *PLoS ONE*, 12(7), e0182188-e0182188. doi:10.1371/journal.pone.0182188

Zhang, H., Xie, X., Kim, M. S., Korniyev, D. A., Holaday, S., & Pare, P. W. (2008). Soil bacteria augment *Arabidopsis* photosynthesis by decreasing glucose sensing and abscisic acid levels in planta. *Plant J*, 56(2), 264-273. doi:10.1111/j.1365-313X.2008.03593.x

Zhang, Q., Lambert, G., Liao, D., Kim, H., Robin, K., Tung, C. K., . . . Austin, R. H. (2011). Acceleration of emergence of bacterial antibiotic resistance in connected microenvironments. *Science*, 333(6050), 1764-1767. doi:10.1126/science.1208747

Zhao, Z., Zhao, Y., Zhuang, X.-Y., Lo, W.-C., Baker, M. A. B., Lo, C.-J., & Bai, F. (2018). Frequent pauses in *Escherichia coli* flagella elongation revealed by single cell real-time fluorescence imaging. *Nature Communications*, 9(1), 1885. doi:10.1038/s41467-018-04288-4

## VITA

Michelle Halsted was born in Fairfax, Virginia to Lisa and Stephen Halsted. She completed her undergraduate studies at Virginia Polytechnic Institute and State University in Blacksburg, VA with a degree in Biological Systems Engineering (2013). After graduation, she began work with Boeing Research & Technology in Seattle, WA. As a member of the Fluids and Lubrication Technology group she gained two years of experience with failure analysis, project management, and qualification & specification.

Michelle began a Ph.D. in Engineering Science and Engineering with The Bredesen Center for Interdisciplinary Research, a joint institution between The University of Tennessee and Oak Ridge National Lab. Michelle conducted her Ph.D. research at Oak Ridge National Laboratory in the Biological and Nanoscale Systems group. Her research was advised by Dr. Scott T. Retterer and designed novel platforms, using nanofabrication techniques, to augment the study of bacterial biofilms. Michelle initiated a collaboration with the Microbial Electrochemistry group at the Naval Research Lab in Washington, D. C., and interned as part of the Naval Research Enterprise Internship Program (2017).

Michelle became increasingly interested in engineering management and business. She began an engineering management graduate certificate with the University of Tennessee Space Institute, and this blossomed into a concurrent M.S. Industrial Engineering from the University of Tennessee (2019). She partnered with mobius pbs, a bioplastic startup, for her M.S. capstone project. This partnership continued after the degree requirements were met. Michelle becoming an intern, and then a part time employee with mobius, while finishing her Ph.D. Her work informs on strategic decision making with economic and environmental analysis. Michelle plans to continue work for mobius full-time after graduation.